Abstract

HATHAWAY III, ALFRED GASTON. High Intensity Pulsed Picosecond Positron Beam for Nanophase Examination. (Under the direction of Ayman I. Hawari.)

The physics of positron (e^+) annihilation within matter has proven to be a powerful non-destructive probe for the characterization of the surface conditions and subsurface defects of materials. The lifetime of a positron is inversely proportional to the concentration of electrons at the site of the annihilation. Because of the particles positive charge, positrons can be trapped at defect sites due to coulombic interactions. High energy (>1 MeV) photons generated by nuclear reactors, impinging on a suitable moderating material, can generate slow positron intensities on the order of 10^8 s^{-1}. When utilizing the pair production mechanism to generate positrons, no suitable start signal is available to indicate the birth of the positron. To compensate, the incident positron beam can be bunched into periodic pulses using rf electric fields applied to suitable electrodes. As the bunched pulse becomes narrower in time; the deviation of arrival time at the target from the electronic clock signal decreases, resulting in an increased time resolution. This increased time resolution allows the study of short lifetime defects which occur in metals and semiconductors.

A high intensity slow positron beam has been successfully implemented at Beam Tube 6 of the PULSTAR reactor at North Carolina State University. The moderator design and extraction optics are optimized for the maximum slow positron rate focused into the guiding field of the beam. Out-of-core testing was performed to optimize the beam performance prior to insertion into Beam Tube 6 of the reactor. In-core testing indicated the slow positron beam could generate an intensity of approximately 10^9 slow e^+/s before stabilizing at $6\text{x}10^8$ e^+/s due to issues with outgassing contaminants modifying the condition of the surface of the moderator.

A variable energy pulsed positron beam was developed, utilizing the high intensity positron beam as a source, for the study of defects in metals and semiconductors. This beam uses a 50 MHz double-gap harmonic buncher to generate pulses with a time resolution on the order of 200 ps. Utilizing the principles of conservation of charge and energy, a relationship between the focal length, kinetic energy and voltage amplitude was determined. A SIMION3D user program was created to test the effectiveness of the buncher design. The calculations indicated the design should successfully generate short pulses of positrons. Simulations, using the software AMaze and TriComp, were also performed to optimize the magnetic guidance of the beam. A 190 nm Tungsten-Molybdenum (WMo) transmission remoderator foil was used to improve the energy and angular spread of the source beam.

Once construction was completed, the magnetic coil positions were optimized to maximize the positron intensity reaching the sample. A Lanthanum-Bromide ($LaBr_3$) scintillation detector was used to detect the 511 keV annihilation gammas because the higher light yield per gamma offsets the larger rise time of the scintillator, yielding a better time resolution. Tests were first performed to demonstrate that slow positrons were successfully emitted from the remoderator foil by measuring the beam intensity against a retarding potential. The detector efficiency was determined using a Na-22 source. To optimize the timing of the beam, discrimination levels were set to accept pulses corresponding to the 511 keV annihilation peak. The timing performance of the buncher was optimized by varying the drift and buncher potentials but the time spectra indicated the presence of a long lifetime component. With the application of a 50 MHz, 10 V_{pp} square wave to the remoderator foil, the beam was successfully chopped, which eliminated the long lifetime component. The optimized spectrometer time resolution was found to be 277 ps.

High Intensity Pulsed Picosecond Positron Beam for Nanophase Examination

by
Alfred G. Hathaway III

A dissertation submitted to the Graduate Faculty of

North Carolina State University
in partial fulfillment of the
requirements for the Degree of
Doctor of Philosophy

Nuclear Engineering

Raleigh, North Carolina

2012

APPROVED BY:

Ayman I. Hawari Committee Chair	Korukonda L. Murty
Mohamed A. Bourham	Bernard W. Wehring

Biography

Alfred (Trey) Gaston Hathaway III obtained a BS in Chemical Engineering from North Carolina State University in May 2003. In August 2003, he began his graduate studies in the Department of Nuclear Engineering under the supervision of Dr. Ayman Hawari. He was offered the opportunity to visit the University of Michigan, Ann Arbor, for the summer of 2004 to work with Dr. David Gidley's positron group to aid in the design of a prototype reactor based slow positron beam for NC State University's PULSTAR Reactor. This work was utilized for the completion of his Master's of Science.

Following the success of the prototype positron beam, the work was further funded by the National Science Foundation to construct a high intensity slow positron beam and associated spectrometers. Trey worked two years aiding in the design of the primary positron beam performing electromagnetic and ion optics simulations to optimize the performance of the primary positron beam and MCNP5 calculations to predict the performance. Following this work, he began to design and construct the variable energy pulsed slow positron beam which is to be used to non-destructively characterize defects in metals and semi-conductors.

Acknowledgements

The author would like to think Dr. Ayman Hawari for the opportunity to work on this project. He would also like to think Dr. Mohamed Bourham, Dr. K. L. Murty and Dr. Bernard Wehring for agreeing to serve on his dissertation committee and advice offered by those members along the way. Thanks should also be extended to Dr. David Gidley for advice, suggestions and warnings during the testing of the pulsed positron beam.

The author would like to extend his thanks to the reactor staff and student operators for operating the reactor while testing the slow positron beam and spectrometers. He would also like to extend special thanks to Andrew Cook, Larry Broussard and Kerry Kincaid for aiding in the assembly of the infrastructure of the positron beam. He would also like to think Dr. Saurabh Mukherjee for his assistance and conversations during the testing process.

The author would also like to extend his thanks to Dr. Jeremy Moxom in his help and expertise on the design of positron instrumentation and analysis along with advice and assistance on setting up and testing the pulsed positron beam.

Table of Contents

List of Tables

List of Figures

Chapter 1 Introduction to Positron Physics

1.1 Introduction

In the late 1920's, Paul Dirac was able to successfully formulate a relativistic quantum theory for an electron moving in an electromagnetic field. While the theory was able to predict the spin properties of an electron, it yielded the troubling result that for every solution which produced electrons with positive kinetic energy there was a mathematically valid solution with negative kinetic energy, which had no physical meaning. The negative solutions could not simply be disregarded due to the fact that perturbations applied to the system could cause transitions of the electron from the positive energy solution to the negative. In an external field, the trajectory of this negative energy electron would be that of an ordinary electron with a positive charge. In an attempt to rectify this discrepancy, Dirac assumed the most stable electron states were the negative energy states and electrons would therefore fill these states with the emission of electromagnetic radiation. Furthermore, most of these states would be filled, forming an infinite uniform distribution which would be unobservable. Positive energy electrons would then be incapable of filling negative energy states and holes in the negative energy distribution would appear as a particle of positive charge. Also, when an ordinary electron fills one of these holes, the electron and hole disappear with the emission of electromagnetic radiation. Dirac assumed these negative energy electrons were protons, and protons were real particles while electrons were holes in the negative energy levels. [1]

In 1933, Carl Anderson observed a particle with a mass on the same order of magnitude of a free electron but with positive charge while analyzing photographs of cosmic ray tracks. Knowledge of the experimental conditions of the measurements allowed Anderson to place a limit on the charge of this particle, which he called the positron, to be no more than a factor of 2 greater than the charge of an electron and the mass could not be more than 20 times larger than the mass of the electron. [2] Therefore, the observed particle could not be a proton, but was a previously unobserved particle. Further support was presented by Blackett and Occhialini with the observation that Dirac's theory allowed the creation of pairs of particles of equal mass but opposite charge with the absorption of high energy photons within matter. The combined kinetic energy of the particles would be:

$$E = h\nu - 2mc^2 \tag{1.1}$$

where E is the total kinetic energy, hv is the energy of the incident photon, m is the rest mass of an electron and c is the speed of light. This relationship was backed by experimental evidence. [3]

1.2 Positrons within Condensed Matter

Theory, backed by experimental evidence, suggests the positron is stable within vacuum e.g. [4], having a lifetime on the order of $2\text{x}10^{21}$ years [5], but upon entering a material, the lifetime is inversely proportional to the local electron density e.g. [4]. Energetic positrons initially lose energy within solids in much the same way electrons do. For high energy positrons, with energy on the order of a few MeV, positrons slow via radiative emission but the energy loss is less efficient compared to electrons due to the difference in charge. Also, the expected range of positrons is less than that of an electron because of annihilation while slowing down. Additional energy loss comes from electron scattering and electronic excitation. [6] At energies on the order of eV and below, positrons slow to thermal energies by scattering off density fluctuations and phonons, namely longitudinal acoustic vibrations. [7]

At room temperature, positrons slow to thermal energies in a matter of picoseconds and continue propagation via quantum diffusion processes. The motion takes the form of a homogeneous random walk because the acoustic-phonon scattering is mostly isotropic. For positrons, the continuity equation includes a term to account for depletion due to trapping and annihilations:

$$\frac{\partial n(x,t)}{\partial t}+\nabla\bullet\mathbf{J}(x,t)=-\lambda(x)n(x,t) \qquad 1.2$$

where $n(x,t)$ is the time dependent positron density, $\boldsymbol{J}(x,t)$ is the current density and $\lambda(x)$ is the depletion rate. This depletion rate includes terms to account for annihilation and trapping,

$$\lambda(x)=\lambda_{ann}(x)+\kappa(x) \qquad 1.3$$

where $\lambda_{ann}(x)$ and $\kappa(x)$ are the annihilation rate and trapping rate of the positrons respectively. The diffusion of positrons is described by Fick's law, which, as in the case of electrons, can contain a term to compensate for an electric field if present.

$$\mathbf{J}(x,t)=-D_{+}\nabla n(x,t)+\eta_{+}\mathbf{E}(x) \qquad 1.4$$

where D_{+} and η_{+} are the positron diffusivity and mobility respectively. [7]

1.2.1 Positron Trapping

As positrons diffuse within a material, they may become trapped at defects present in the crystal lattice. Atoms missing from the crystal lattice result in the absence of a repulsive potential that the positive nucleus produces. This absence results in an attractive negative potential which can trap the diffusing positrons.

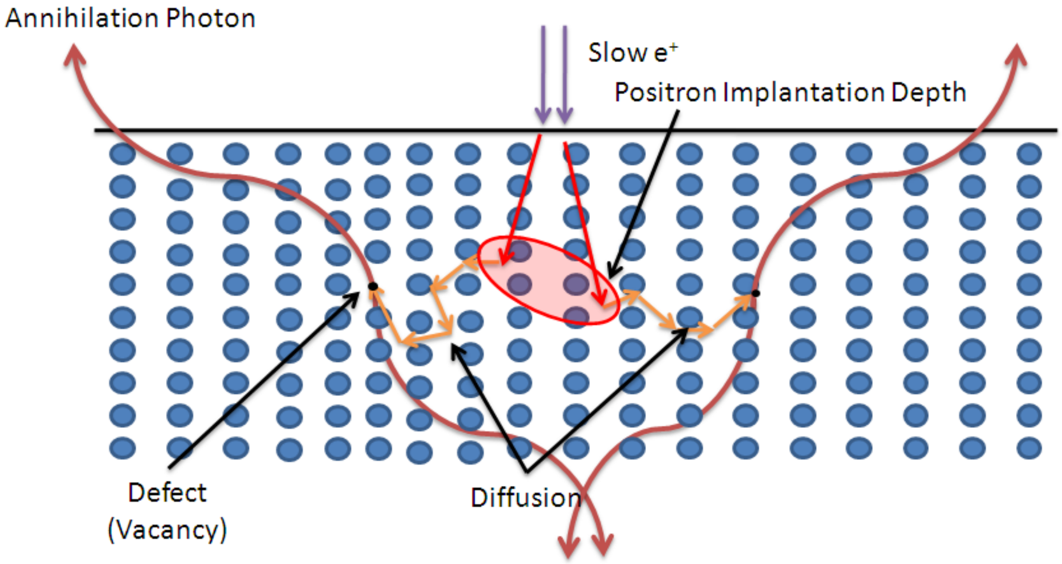

Fig. 1.1. Illustration of the lifetime, from implantation to annihilation, of positrons within a material.

The positron trapping rate, κ, is proportional to the concentration of defects present, *C*. For transition limited trapping (κ_{tl}):

$$\kappa_{tl} = \mu C \qquad 1.5$$

where μ is the trapping coefficient and is constant for a particular defect. For diffusion limited trapping (κ_{dl}), the trapping rate includes the diffusion coefficient of positrons within the material. The trapping rate for a spherical defect takes the form:

$$\kappa_{dl} = 4\pi r_d D_+ C \qquad 1.6$$

In this form, $4\pi r_d$ is related to the size of a spherical defect, where r_d is taken as the radius and D_+ is the positrons diffusion coefficient. This trapping rate can be dependent on the material of the sample and the temperature dependence of the diffusion coefficient. The total trapping rate will therefore be the superposition of the two individual trapping rates. [8]

$$\frac{1}{\kappa} = \frac{1}{\kappa_{tl}} + \frac{1}{\kappa_{dl}} \tag{1.7}$$

1.3 Positron moderation

As stated previously, positrons of sufficient kinetic energy are capable of implanting in a material where they quickly loose energy to thermal levels and begin to diffuse. If a positron reaches thermal energies within a diffusion length (the average distance a positron travels during its lifetime) of the surface, it can reach the surface with its next jump while diffusing. At the surface, there is a possibility of remission as a free positron. To maximize the efficiency of free positron emission, moderating materials can be annealed to remove non-equilibrium defects which act as trapping sites. Positrons emitted from the surface of a material with a negative positron work function obtain kinetic energies up to the magnitude of the positron work function of the material. [7]

1.3.1 The Negative Positron Work Function

The work function of an electron (φ_-) can be thought of as the minimum amount of energy required to remove an electron from just inside the surface to a location just outside the surface. It is composed of two terms; the surface dipole barrier and electron chemical potential, which are contributions by the surface and bulk of the crystal respectively.

$$\varphi_- = +D - \mu_- \tag{1.8}$$

In Eq.1.8, μ_- is the chemical potential of an electron, which is simply the absolute value of the Fermi energy for metals. The surface dipole (D) term arises mainly from the fact that the electron distribution near the surface protrudes into the vacuum outside the surface. [9]

The work function of a positron can be defined in a similar manner.

$$\varphi_+ = -D - \mu_+ \qquad 1.9$$

The chemical potential of the positron (μ_+) is influenced by the by the repulsive forces due to the ion cores and attractive forces by the electrons. [6] Because of the charge of the positron, the surface dipole term is negative, meaning positrons will be drawn out of the surface. Depending on the strength of the dipole term, the work function of a positron can be zero or negative. A negative work function would result in work needing to be performed to keep the positron within the surface. [10] It has been demonstrated that the slow positron emission rate from metal surfaces increases with as this work function becomes more negative. [6]

1.3.2 Slow Positron Reemission

Implanted positrons diffusing to the surface of a material can undergo a variety of processes upon reaching the surface. The four main routes are:

- Trapping and annihilation at the surface
- Emission as free positronium atom (a hydrogen-like bound state of a positron and electron)
- Emission as a free positron
- Reflection [11]

These processes can occur with roughly equal probability. [12] Upon reaching the surface of a material, thermalized positrons may be reemitted with a distribution of kinetic energies. These energies can vary up to the work function of the material, and for a clean surface, the energy spread of the peak is consistent with thermal broadening. An additional feature of interest is the high energy tail of the elastic peak. This can be attributed to positrons that reach the surface before complete thermalization. [13]

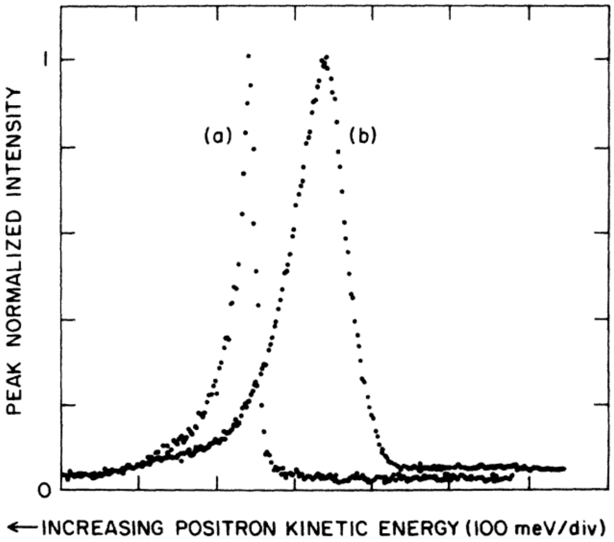

Fig. 1.2. Measured energy distribution of slow positrons emitted from the surface of a Ni(100) crystal. Curve *b* is collected at room temperature while curve *a* is collected at 23K. [13]

Slow positrons also leave the surface of a material with an angular spread strongly peaked about the surface normal, as seen in fig. 1.3. If the work function is thought of as a potential step at the surface, the positrons gain kinetic energy in the direction of the surface normal, which introduces the angular distribution. This angular distribution has a half angle ($\theta_{1/2}$) that can be estimated by:

$$\theta^{i}_{1/2} \cong \left(\frac{E_{prob}}{\varphi^{+}}\right)^{1/2} = \left(\frac{kT}{\varphi^{+}}\right)^{1/2} \quad 1.10$$

where E_{prob}, or kT, is the most probable energy of the positron and φ_{+} is the work function of the material. This angular spread is also consistent with the thermal broadening of the positron's component momentum parallel to the surface. [13]

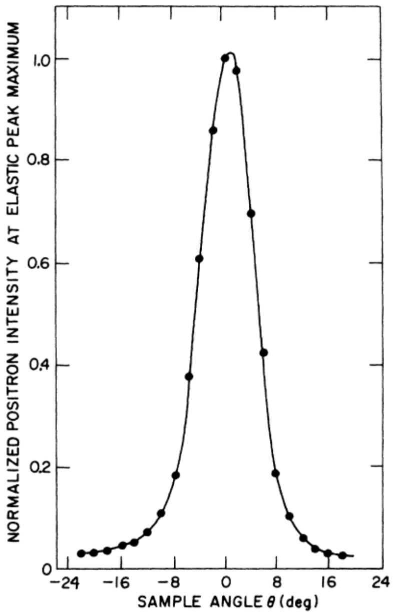

Fig. 1.3. Measured angular distribution of slow positrons emitted from the surface of a W(110) crystal. [13]

1.4 Positron Sources

1.4.1 Radioisotope Sources

Laboratory based slow positron beams tend to use radioactive isotopes as sources. For β^+-decay, a proton within an unstable nucleus is converted into a neutron with the emission of a positron and neutrino.

$$p \rightarrow n + e^{+} + \nu_e \qquad 1.11$$

The positron is not present in the nucleus prior to emission; rather it is created via the energy released by the decay. [14] A free proton is incapable of undergoing such a reaction due to the conservation of energy, the proton rest mass being smaller than that of the neutron. However, within a nucleus, excess binding energy allows the proton to undergo the decay. [15] An example of such a radioisotope is ^{22}Na:

$$^{22}Na \rightarrow {}^{22}Ne + e^{+} + \nu_{e} \qquad 1.12$$

The emission of the neutrino results in the emitted positron having a broad energy spectrum. Figure 1.4 presents a typical energy spectrum of positrons emitted from Na-22. The high kinetic energy of the emitted positrons results in a relatively large implantation depth, which limits the use of radioactive sources to the study of the bulk properties of a material. [16] By implanting the positrons generated by the source into a suitable moderating material, the large energy distribution can be reduced to a few eV due to positron thermalization and reemission. With the strongest commercially available isotopic sources, this technique can be utilized to produce monoenergetic slow positron beams with intensities which can reach 10^{6} s^{-1} under ideal conditions. [7] This result is influenced by the moderation efficiency of the slow e^{+} beam, the highest efficiency for an isotopic beam being a noble gas deposited (frozen) on a tungsten surface.

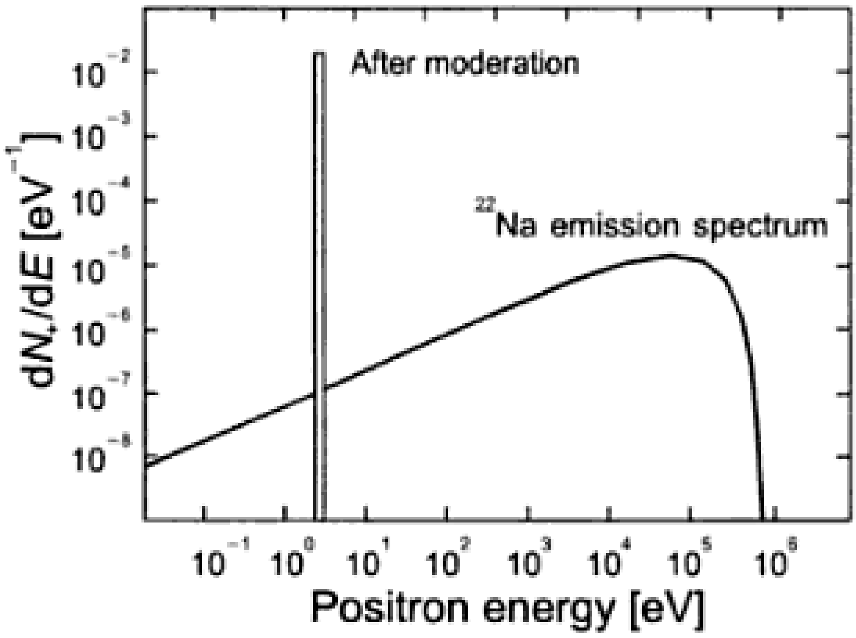

Fig. 1.4. Comparison of the energy spectrum of positrons emitted directly from nuclear decay and after the reemission of the positrons from a moderating material. [8]

1.4.2 Pair Production

A practical way to reach intensities greater than practically achievable by an isotopic beam (on the order of 10^8-10^9 s^{-1}) is the utilization of the pair production mechanism in a high-Z convertor material. Pair production is the creation of a positron-electron pair via the conversion of a photon in the vicinity of a third body to conserve momentum. [15] The threshold energy for such a process is equal $2m_ec^2$ (=1.022 MeV). As presented by Blackett and Occhialini, the energy of the pair is given by:

$$T_- + T_+ = E - 2m_ec^2 \qquad 1.13$$

where $T_{-/+}$ is the kinetic energy of the resulting particles, E is the excitation energy of the nucleus, m_e is the mass of the electron and c is the speed of light. The total atomic pair production cross section is proportional to the square of the atomic number of the nucleus and increases with photon energy, approaching a constant at high energy. [17] Therefore, the utilization of a high-Z moderating material will maximize the probability for pair production to occur.

Nuclear Reactors and LINACs are capable of generating photons with energy in excess of the pair production threshold. These photons, incident on a suitable moderating material, can then generate high intensity beams. In LINACs, bremsstrahlung radiation creates fast positron-electron pairs by implanting relativistic electron beams into high-Z materials. The fast positrons produced by pair production can then be moderated to low energies, creating pulsed slow positron beams. Alternatively, nuclear reactors can generate high energy photons directly from the nuclear chain reaction, resulting in continuous beams. The photon flux can be intensified and hardened with the use of thermal neutron capture reactions which emit high energy photons, such as using a cadmium shroud, $^{113}Cd(n,\gamma)^{114}Cd$. [7]

1.4.2.1 *Reactor Based Slow Positron Beams*

One of the first attempts to use a nuclear reactor to generate a slow positron beam did not involve the pair production mechanism. In 1983, Brookhaven National Laboratory began operation of an intense slow positron beam, where a nuclear reactor was used to generate a high activity (~100 Ci) Cu-64 source. This source was transferred to a source-moderator chamber where it was deposited onto a Tungsten moderator crystal. The positrons were then magnetically guided from the source region to the experimental stations. Because this beam operated via a source with a half-life of 12.8 hr, the beam intensity would vary with time. This beam was used to study the momentum distribution of a sample using angular correlation measurements of the annihilation gammas. [7]

The first reactor to begin to use the pair production mechanism to generate slow positrons was the Delft reactor located in the Netherlands. Initially, it was to use a hybrid of a Copper source and pair production from thermal neutron capture gammas. [7] The hybrid design consisted of Copper tubes with a Tungsten foil lining. It was determined that the beam was generating approximately the same number of slow positrons from the pair production mechanism as from the activated source, therefore the moderators were redesigned to be composed of only Tungsten foils and utilize the pair production mechanism exclusively. This moderator consisted of four Tungsten banks forming a 1x1 cm array 8 cm in diameter, which was able to generate an intensity of $2\text{x}10^8$ s^{-1}. [38]

1.4.3 The Quantification of Beam Quality

Fast positrons, from radioisotopes or pair production, can be used to generate slow positrons via the remoderation process. The slow positrons emitted from a moderating material have a lower energy and angular spread than those impinging on the surface because of the physics of remoderation. These slow positrons can be electrostatically focused or magnetically guided to form a slow positron beam. The phase space and brightness are two quantities which are used to describe the quality of the resulting beam and predict the future behavior of the beam.

1.4.3.1 *The Phase Space of Positron Beams*

The initial position and momentum of a charged particle (e.g. a positron) in Cartesian co-ordinates (x, y, z, px, py, pz) define its position in a six-dimensional phase space. A group of particle trajectories forming a beam occupy a volume in phase space which, under the influence of conservative forces, remains constant, according to Liouville's theorem. For cylindrically symmetric electrostatic beam systems, the phase space of the beam crossing a plane perpendicular to its centerline can be represented by an area in a plane with ordinates r and θ.

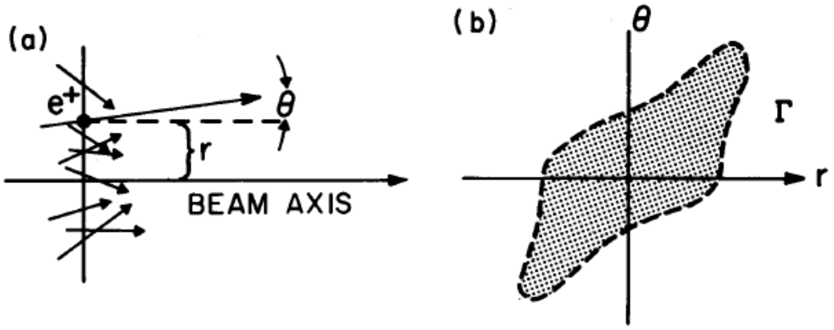

Fig. 1.5. (a) Particles in r-θ are described by their distance from the centerline and angle particle creates with horizontal. (b) Example of r-θ diagram for ensemble of particles. The area of the diagram is invariant. [20]

For these diagrams, r is the perpendicular distance of the particle from the beam axis and θ is the angle of the particle trajectory away from the axial direction. It is assumed that the particles under consideration have minimal transverse energies, meaning particle trajectories form small angles away from the axis, leading to the small-angle approximation, where the angle of the trajectory (*θ*) can be taken as $\partial r/\partial z$. The beam is assumed to be radially symmetric, therefore the position in *x* and *y* in Cartesian coordinates can be replaced with a single ordinate *r*. The *r*-*θ* diagram is an abstraction of an envelope of real particle trajectories as they traverse a plane perpendicular to the *z*-axis. It represents a "snapshot" of the particle trajectories at an instantaneous moment along the *z*-axis. [19] The motion of the particles in a beam is constrained by Liouville's theorem, which states that the phase space of a group of moving particles is invariant under the action of conservative forces. This means a group of particles form a volume in the six-dimensional phase space which can change shape while traversing a lens system, but the volume cannot. [18] Therefore the shape of the *r*-*θ* diagram may change as the particles travel down the *z*-axis, but the area enclose by the *r*-*θ* diagram remains the same. By applying Liouville's theorem to the *r*-*θ* diagram, the transverse momentum (*p*) can be taken as:

$$p = \theta\sqrt{2mE} \qquad 1.14$$

where *θ* is the angle of the trajectory, and *m* and *E* are the mass and energy of the particle respectively. When considering the phase space of particles in the x-z plane, the area $x \cdot p_x$ is a conserved, so $x\theta(E)^{1/2}$ is a conserved area. By integrating over the boundary of particles composing the beam, the area of the *r*-*θ* diagram can be generalized to $\Gamma=4x\theta$. Therefore Liouville's theorem for a group of moving particles can be taken as: [19]

$$\Gamma\sqrt{E} = constant \qquad 1.15$$

The implication of this relationship is that the beam diameter can be decreased only with a corresponding increase in the angular divergence of the beam. [20]

1.4.3.2 *Beam Brightness*

The concept of beam brightness provides a figure of merit which can characterize the properties of a charged particle beam. An analogy to light optics is that the ratio of the radiance of a light beam to the square of the local index of refraction is invariant. For light, this implies that the brightness of a beam is a measure of the energy flux density per unit solid angle. In terms of charged particle beams, with consideration of conservation of charge, the brightness defines the beam's charge flux density per unit solid angle. The current density J_K is equal to:

$$J_K = \int_0^{\frac{1}{2}\pi} R_o^* \cos\theta d\Omega \tag{1.16}$$

where R_o^* is the brightness and is independent of angle θ. The solid angle is taken as:

$$\Omega = 2\pi(1-\cos\theta) \tag{1.17}$$

and the solution is simply:

$$R_o^* = \frac{1}{\pi} J_K \tag{1.18}$$

The particle is emitted with a characteristic energy (E_k), so the voltage can be determined as:

$$eV_k = E_k \tag{1.19}$$

Therefore the brightness per volt can be defined as: [21]

$$R_v^* = \frac{eJ_k}{\pi E_k} \tag{1.20}$$

A more common definition in characterizing positron beam brightness is: [6]

$$R_v = \frac{I}{\theta^2 d^2 E} \tag{1.21}$$

This derivation demonstrates that the brightness per volt is related to the ratio of the source intensity and square of the product of the phase space area and energy of the particle.

The beam brightness can be increased by remoderating the positron beam. As mentioned previously, the phase space describing a beam must remain constant under the influence of conservative forces. The brightness is a function of the phase space area, so conservative forces cannot increase the brightness of the beam. Remoderation is non-conservative so Liouville's theorem does not apply. Positrons reemitted from the remoderator surface possess energy and angular distributions which are dependent on the composition and surface condition of the remoderating material. Because the reemitted positrons have a smaller angular spread after reemission, the phase space area decreases. This, coupled with the decrease in the energy distribution, leads to an increase in the brightness.

1.5 Defect Characterization Techniques

The study of defects and the evolution of the microstructure has become an important aspect in the development of modern materials. For example, ion implantation is important in the fabrication of semiconductor devices, but creates many defects requiring additional processing steps such as annealing. It is therefore advantageous to study the formation of defects and how further processing influences the presence of defects. Defect characterization is not limited to the study of microelectronics though. Self-irradiation of Plutonium can generate vacancies which can precipitate into voids leading to macroscopic swelling of the material, resulting in uncertainty of the materials lifetime in a stockpile. [18]

Positrons can be used to probe the composition and structure of a material, which provides complementary information to that of other techniques. Several techniques offer the ability to depth profile a sample for impurity atoms. One such technique is Secondary Ion Mass Spectrometry (SIMS), where the sample in question is sputtered and the atoms ejected are analyzed. With the impact of a heavy ion, with energies of a few keV, sample atoms are ejected from the surface, with a sputtering yield typically several ejected atoms per incident ion. A fraction of the ejected atoms are then ionized, where they can be analyzed by a mass spectrometer to allow the determination of the composition of the ejected flux. Because this technique erodes the surface of the sample, the technique provides depth profiling of the sample because surface being analyzed moves deeper within the sample. [23] While this technique can characterize impurity atoms it is not sensitive to open-volume defects.

Additional techniques are required to characterize the microstructure of a sample. Small angle neutron or x-ray scattering (SANS/SAXS) allow for indirect probing of open-volume defects. Small angle X-ray scattering is capable of determining variations in the density in the size scale of subnanometer to 100nm defects. For this technique, observed x-ray scattering spectra are analyzed by fitting the data to calculated spectra generated by scattering theory for samples with varying density fluctuations. The data is fit using a least squares method with optimizations on the shaping parameter and average radius of the pore. For thin samples, a reflection type geometry must be utilized to maximize the scattering intensity and models must consider reflection and refraction at the samples surface. [24] This is also the case for small angle neutron scattering. The collected scattering data is corrected for background and the resulting data is converted into a scattering cross-section.

A size distribution is fit to the scattering cross-section data, where the slope of the curvature provides the mean size and distribution of the defect and absolute intensity provides the number density and volume fraction. The data for a sample without defects can be subtracted from one with defects to isolate the feature of interest. [25]

One of the best methods to examine open-volume defects is using particles, such as a helium atoms, hydrogen atoms or positrons, which enter the sample and become trapped in cavities. One of these techniques is Mercury porosimetry. For this technique, the sample must first be cleaned and degassed in a vacuum (~1x10^{-4} atm) to removed adsorbed species from the sample. While under vacuum, mercury is introduced to the chamber and the pressure is built-up gradually to high pressure (~2000 atm). As the pressure increases, mercury penetrates the pores, lowering the level of the mercury introduced to the chamber. The chamber pressure versus the mercury level is recorded. [27] Typically, to quantify the pore size it is assume that the sample contains nonintersecting cylindrical pores. This model converts the applied pressure into pore size. The volume distribution of mercury introduced into the sample is determined by taking the derivative of the mercury level versus pore size data. [28] Another common technique to determine the pore size distribution of a sample is the use of nitrogen as a gas probe. For this technique, models must again be calculated to generate isotherms, which can then be fit to the collected data to determine the pore distribution. [29] For these techniques to be successful, the pore must be connected to the surface to allow the impinging probe atoms to breech the pore.

There are many advantages of performing these analyses by positrons alone. The material is not damaged by positron irradiation and because of positron diffusion; analysis of open and closed-volume defects can be performed. With a variable energy positron beam, layered structures can be studied, resulting in the depth-distribution of defects within a sample. [7] Figure 1.6 [25] compares the use of positrons for defect characterization to other techniques. As can be seen, positrons are able to discern the smallest defects over a wide range of implantation depth below the surface. It is also capable of determining the defect concentration over a wide range of concentrations and depths.

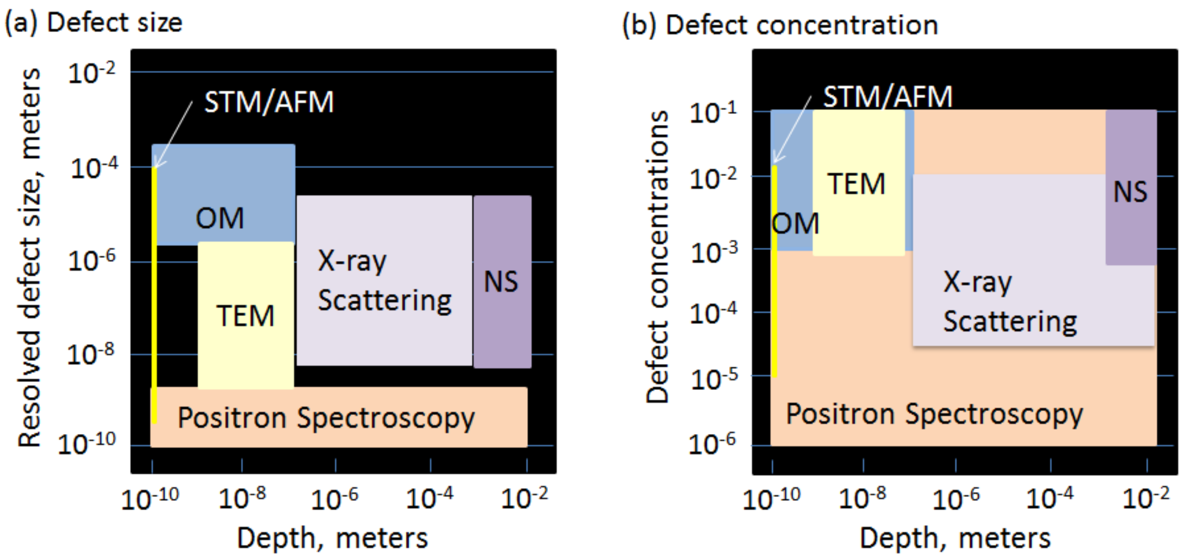

Fig. 1.6. Comparison of various defect characterization techniques for defect size vs. defect depth (a) and defect concentration vs. defect depth (b). [25]

1.5.1 Doppler Broadening

Upon annihilating, a positron-electron pair must conserve momentum, transferring the momentum of the system to the photons produced. If the pair were at rest, the resulting 511 keV gamma rays would be collinear, i.e., emitted at 180° apart. Motion of the particles introduces variations in the momentum of the gamma rays. This can best be seen by viewing the annihilation process in a lab frame of reference, as demonstrated by Fig. 1.7. Since the positron is usually thermalized when annihilation occurs, the momentum of the system can be attributed to the electron, therefore the measurement of 511 keV peak offers a probe of the momentum distribution of electrons in a sample. By analysis the annihilation of the positron and electron in the center of mass reference frame, the energy spread of the annihilation peak can be determined by:

$$\Delta E_{\gamma} = mcv_{cm}\cos\theta \tag{1.22}$$

where v_{cm} is the center of mass velocity of the system and θ is the angle separating the direction of motion and one of the emitted gamma rays. [4]

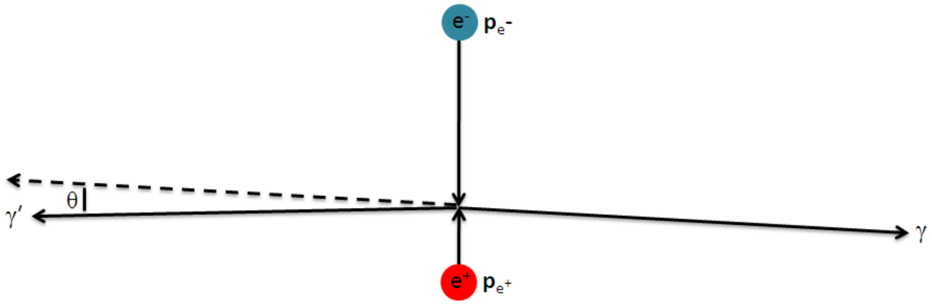

Fig. 1.7. Diagram of the conservation of momentum of an annihilating positron-electron pair in the lab reference frame.

For Doppler Broadening Spectroscopy (DBS), the energy spectrum of the 511 keV annihilation peak is measured using a detector with suitable energy resolution, usually a high purity germanium detector. [23] When trapped in open volume defects, positrons are more likely to annihilate with valence shell electrons, which have lower momentum, rather than core electrons, leading to a sharper annihilation peak. [8]

Two parameters of interest to Doppler broadening measurements is the *S*-parameter and the *W*-parameter. The *S*-parameter is defined as the ratio of the area of the low-momentum central region of the annihilation peak to the total peak area.

$$S = \frac{A_s}{A_o}, \quad A_s = \int_{E_o - E_s}^{E_o + E_s} N_D \, dE \tag{1.23}$$

In Eq.1.23**,** S is the calculated S-parameter, A_o is the total area of the 511 keV peak and A_s is the area about the center of the peak. This area is defined as the area under the peak $\pm E_s$ from the central energy E_o (511 keV). A high S-parameter indicates a greater concentration of annihilations with lower momentum valence electrons, therefore more vacancies. The W-parameter is also of interest. This is taken as the ratio of the area of the higher momentum tails of the annihilation peak to that of the total peak area. [8]

$$W = \frac{A_w}{A_o}, \quad A_w = \int_{E_1}^{E_2} N_D dE \qquad 1.24$$

In this case, W is the calculated W-parameter, A_o is the area of the 511 keV peak and A_w is the area under the wings of the peak. In this case, E_1 and E_2 define an energy range from a suitable starting point (E_1) to the edge of the peak (E_2). The value of E_1 must be chosen so it does not interfere with the calculation of the S-parameter. [23]

1.5.2 Positron Annihilation Lifetime Spectroscopy (PALS)

The lifetime of positrons within a material is a function of the electron density at the site of the annihilation. [8] When trapped within a defect, the positron encounters a lower electron density due to the absence of lattice atoms, resulting in a longer positron lifetime, relative to the lifetime within the bulk of the material. The measurement of the lifetime within a material can therefore be related to the concentration, size and type of defect.

The key to a successful positron annihilation lifetime experiment is the precise determination of the instant that the positron enters a sample. In a conventional bulk positron experiment, a Sodium-22 radioisotope is utilized as a positron source, which emits a positron nearly 90% of the time and decays to the 1.27 MeV level of Neon-22. The emission of the 1.27 MeV gamma ray is nearly instantaneous with the emission of the positron. The detection of this gamma ray can therefore be utilized as a time marker for the beginning of the life of the positron. The detection of a 511keV annihilation gamma ray in delayed coincidence with the 1.27 MeV gamma ray can therefore be used to determine the lifetime of the positron in the sample. The start single and stop signal, with a sufficient delay, is processed by a time-to-amplitude converter (TAC) and sent to a multichannel analyzer (MCA) resulting in a lifetime spectra, which is a histogram of detected lifetimes. While this technique offers a simple experiment to characterize the nanophase structure of a sample, because of the high kinetic energy of the positron, the method is limited to characterizing the bulk properties of a material. [8]

A histogram of the measured lifetimes takes the form of a summation of decaying exponentials. As a simple example, consider a sample which contains only one type of defect. Positrons can then annihilate in either the bulk of the sample or become trapped in a defect. The individual annihilation rates are therefore:

$$\frac{dn_b(t)}{dt} = -(\lambda_b + \kappa_d)n_b(t) \tag{1.25}$$

$$\frac{dn_d(t)}{dt} = -\lambda_d n_d(t) + \kappa_d n_b(t) \tag{1.26}$$

where λ_b and λ_d are the positron annihilation rates in the bulk and defect respectively and κ_d is the trapping rate of the particular defect. The solutions to these equations results in a decay spectrum:

$$D(t) = I_1 \exp\left(-\frac{t}{\tau_1}\right) + I_2 \exp\left(-\frac{t}{\tau_2}\right) \tag{1.27}$$

where:

$$\tau_1 = \frac{1}{\lambda_b + \kappa_d} \tag{1.28}$$

$$\tau_2 = \frac{1}{\lambda_d} \tag{1.29}$$

$$I_1 = 1 - I_2 \tag{1.30}$$

$$I_2 = \frac{\kappa_d}{\lambda_b - \lambda_d + \kappa_d} \tag{1.31}$$

The lifetime spectrum would therefore be the time derivative of Eq.1.27.

$$N(t) = \left| \frac{dD(t)}{dt} \right| = \frac{I_1}{\tau_1} \exp\left(-\frac{t}{\tau_1} \right) + \frac{I_2}{\tau_2} \exp\left(-\frac{t}{\tau_2} \right) \tag{1.32}$$

where I_1 and I_2 are the intensities of the signal and τ_1 and τ_2 are the lifetime components. To match the results of the actual measurement, a time resolution function must be convolved with the lifetime spectrum. This resolution function, which is attributed mostly to the time resolution of the detectors, can be approximated by a sum of Gaussian functions. With the utilization of least squares fitting techniques, a suitable model with appropriate lifetime components and resolution function can be fit to measured data. The intensities and lifetime components can then be related to the type and concentration of defects present. [8] For samples with high defect concentrations, almost all implanted positrons annihilate while trapped. This yields the positron lifetime of the particular defect present in the material. [31]

As seen in fig. 1.4, moderating a spectrum of fast positrons allows the production of slow positron beams, which allows the control of the kinetic energy of the particle upon entering the sample, allowing depth profiling of the sample. Unfortunately, in the case of using a radioisotope source, the moderation process destroys the time correlation between the between the emission of the gamma ray and positron, i.e. the start of the positron lifetime is unknown. [16] Additional measures must therefore be undertaken to perform the measurement. One method to provide a suitable start signal is the detection of secondary electrons emitted from a sample when a positron enters. The detection of these secondary electrons in a CEMA detector and coincident annihilation gamma ray marks the lifetime of the positron in the sample. Due to the energy and angular spread of the emitted secondary electrons, the time resolution is usually limited to around 500 ps. [16]

1.6 Pulsed Positron Beams

The lifetime of positrons in a metal or semiconductor is typically in the range of 100-300 picoseconds [32], therefore the detection of secondary electrons does not provide a suitable time resolution to characterize defects in these materials. An additional method to determine a start signal is to generate a time resolved beam via bunching of the incident beam. [6] Beam bunching is the process of compressing a continuous beam of particles into narrow periodic pulses [33], which can offer greatly enhanced time resolution. One technique for producing such longitudinal bunching is the use of rf electric fields applied to suitable electrodes, producing acceleration gaps which impart a velocity modulation to the positrons traversing the gap. Figure 1.8 displays example phase space plots of positrons undergoing the bunching process. The velocity modulation imparted to the positrons decelerates positrons which lead the final pulse and accelerate those which lag the positron pulse. After drifting some distance, the instantaneous positron current is maximized at the focal point of the buncher. The particle bunching is optimized when the initial energy distribution of the beam is small compared to the voltage applied to the bunching electrodes

[33] and the increased time resolution comes at the expense of increased energy spread at the focal point.

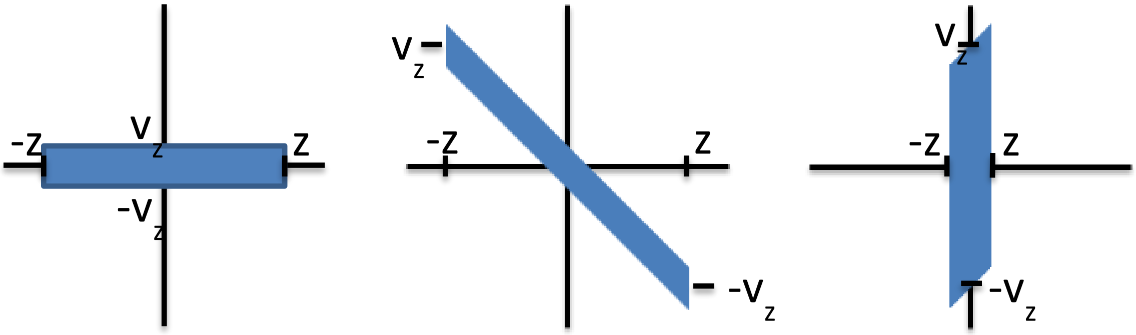

Fig. 1.8. Phase space plots of positrons undergoing the bunching process. The figure on the left depicts the phase space of the positrons prior to entering the buncher. The figure in the middle presents the phase space of the positrons after traversing the accelerating gap and receiving an energy modulation. The figure on the right depicts the phase space of the positrons at the target. At the target, the velocity spread is larger but bunch width is smaller, as opposed to the original phase space which has smaller velocity spread but a wide pulse. The area of the phase space is constant.

The applied rf voltage results in a time-varying electric field which takes the form of a sine wave. Only a portion of this waveform results in optimum bunching, with the rest producing background counts between the pulses. The signal-to-background ratio can be improved by chopping the incident continuous positron beam into pulses which are narrow enough to minimize the number of positrons falling on the non-ideal portion of the rf field. The chopper prevents positrons from reaching the non-ideal portion of the applied rf voltage, preventing energy modulation which adds to the background.

The increase in time resolution is due to the fact that the start signal can be taken directly from the electronics of the system, which has less variability than the detection of a secondary particle. The time resolution of the spectrometer ranges from the moment the positrons reaches the surface to the detection of the corresponding annihilation photon, and includes the width of the positron pulses and the electronic time resolution of the detector system. As the width of the positrons pulses narrow, in time, the deviation of the arrival time of the positron at the sample to the electronic start signal used for the lifetime measurement decreases, resulting in a smaller time resolution for the spectrometer.

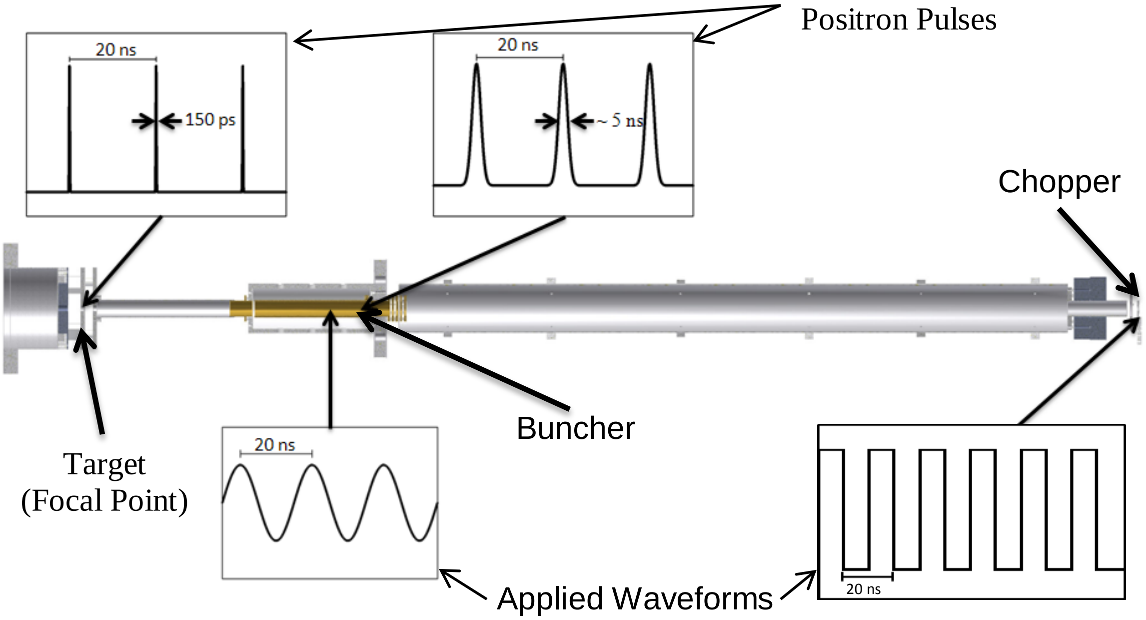

Fig. 1.9. Illustration of the use of the techniques of chopping the incident beam and rf bunching to produce positron bunches. The incident positron beam is chopped using a square wave potential applied to a remoderator. Five nanosecond wide pulses arrive at the first acceleration gap of the double gap buncher every 20 ns. The rf buncher produces high resolution pulses with a repetition rate of 20 ns.

Chapter 2 The Intense Slow Positron Beam

2.1 The PULSTAR Reactor at North Carolina State University

In 1953, North Carolina State University was the first nonfederal institution to own and operate a nuclear reactor. The PULSTAR Reactor began operation in 1972 and is the fourth reactor to be operated at the site. This generation of the reactor is a swimming pool style research reactor, with the core placed within a 15000 gallon open tank of pure water.

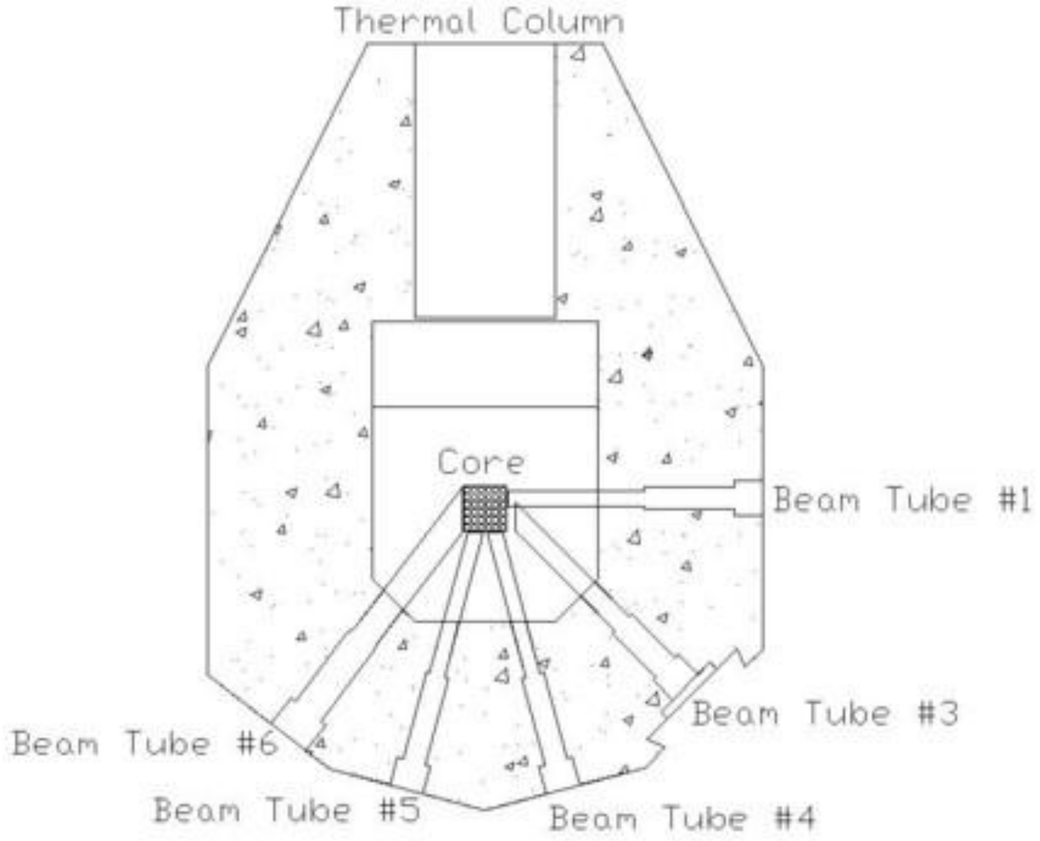

Fig. 2.1. A diagram of the PULSTAR reactor. Five of the six beam ports radiate out from the reactor core. Beam Tube #2, which is not shown, passes through the reactor in front of the core.

The core is composed of 359 kg of uranium dioxide fuel enriched to 4% uranium-235, producing a peak power of 1-MWth. Six beam tubes (BT) positioned within the pool allow experiments to be placed as close to the surface of the core as possible, as seen in fig. 2.1.

Five of the six beam tubes extend radially from the surface of the core. The remaining beam tube acts as a through port and crosses the face of the reactor core. [34]

The pool is filled with pure light water which is utilized as coolant and neutron moderator. Reflectors are placed on two sides of the core to enhance the neutron economy and therefore maximize fuel usage. Because of the high fuel to moderator ratio, the core is highly undermoderated. This design characteristic, combined with the small reactor core dimensions results in a high fast neutron leakage from the core boundary, which causes the thermal neutron flux to peak at the edges of the core. [35] This allows the relatively small research reactor the capability of generating radiation intensities comparable to reactors many times its size.

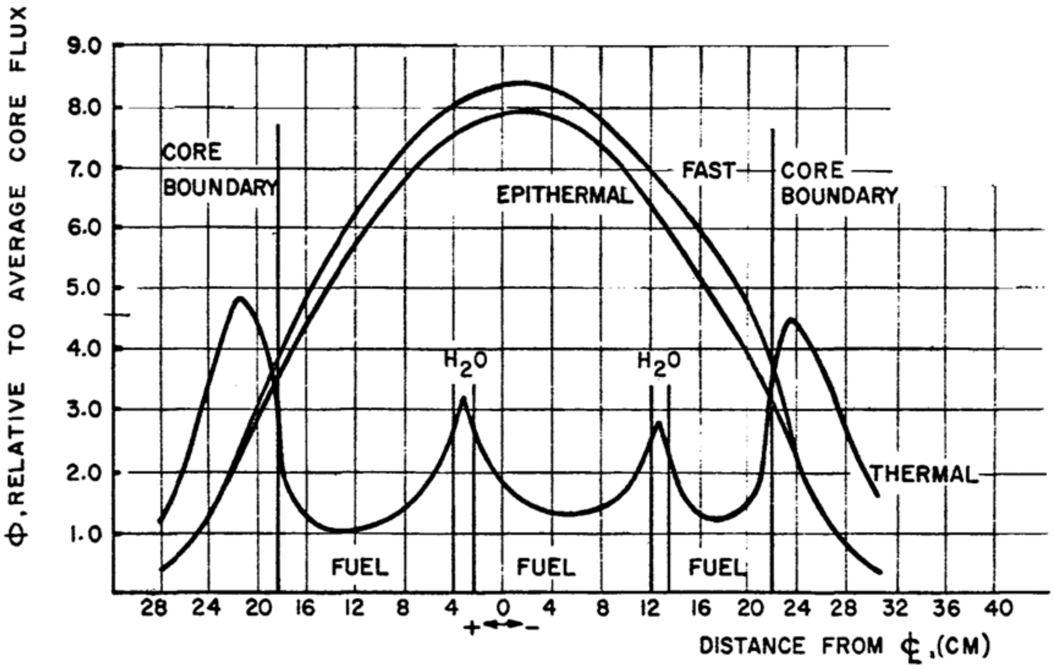

Fig. 2.2. A measured neutron flux profile of the PULSTAR reactor. The fast, epithermal and thermal neutron fluxes can be seen.

Beam tube 6 was designated to house the slow positron beam. Beam tube 6 is square with a cross section of nearly 12”x12”, forming a 37° angle to the northwest face of the reactor core. The large cross section allows the use of large e^+ moderators, maximizing the amount of positron moderating material in the vicinity of the core. Another highlight of this location is that the beam is directed towards the wall of the confinement building, allowing the positrons to be steered into the adjoining labs which house the spectrometers.

2.2 Simulation and Design Calculations

Before construction of the second generation intense slow positron beam, thorough design calculations were performed to predict and optimize the performance of the final beam. The Monte Carlo code MCNP was utilized to directly calculate the energy dependent reaction rates of positrons within the moderator. Also, a SIMION user program was written to predict the survival of positrons from the moderator, coupled with the utilization of the ion optics modeling software AMaze which offered better simulations of the extraction and focusing of positrons into a magnetic gradient produced by a solenoid.

2.2.1 Slow Positron Production Rate

For the second generation beam, the core of the PULSTAR reactor was rearranged to place fuel directly beside the entrance of beam tube 6 to achieve the increase in photon flux predicted by calculations performed during work on a prototype beam. [36]

To produce a more intense beam, a larger moderator was designed to be placed as close to the end of beam tube 6 as possible. The concept design of the moderator for the second generation beam consisted of an array of interlocking one inch wide tungsten strips with an overall diameter of 8.8”, forming a matrix of 1 cm cells, to utilize as much of the 12”x12” cross section of beam tube 6 as possible. MCNP calculations were performed to optimize the thickness of the tungsten vanes to maximize slow positron production. To predict the positron production rate, the core of the PULSTAR Reactor was modeled with two tungsten cells placed as close to the surface of BT6 as possible.

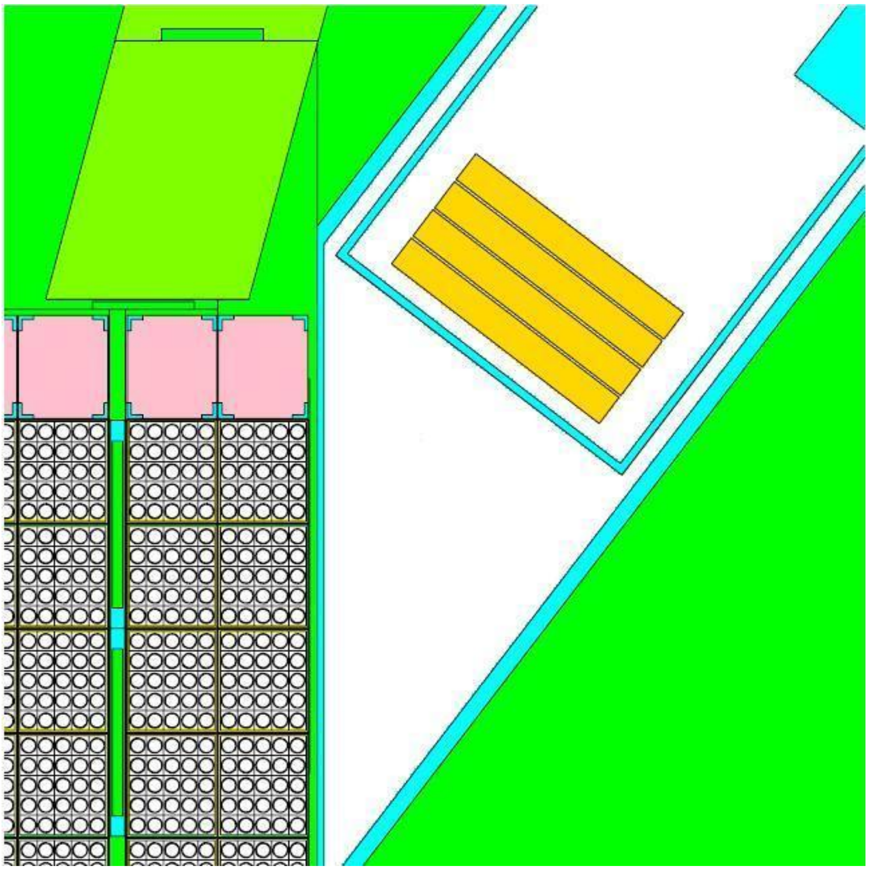

Fig. 2.3. A MCNP model of the PULSTAR reactor core with fuel next to beam tube 6 utilized for calculations for the second generation beam. Four 8.8” tungsten moderator banks were modeled to be as close to the core as possible to see how the production varied with distance from the core.

Rather than modeling each individual vane comprising the moderator, each bank was modeled as a single cylinder with a diameter of 8.8” and a height of 1”, as seen in fig. 2.4. For this simplification to be accurate, the density supplied for the cell defining the moderator must be reduced to maintain the same linear attenuation coefficient as normal tungsten. Varying the thickness of the tungsten strips will result in a change in the density supplied to MCNP for this region, allowing the optimization of the thickness. To determine this simulation density, the mass of the moderator must first be determined. The surface area of the moderator will be essentially constant, assuming overlap of the tungsten vanes is minimal due to the thinness of the material utilized, so the product of the surface area of the moderator, approximately 1819 cm^2, and the thickness under consideration will yield the volume of the tungsten used to construct the moderator in question.

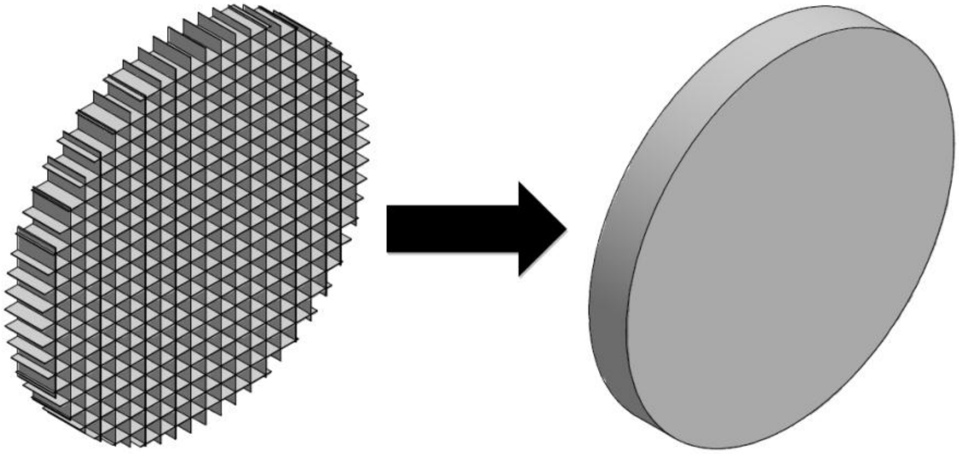

Fig. 2.4. Image demonstrating the conversion of 1x1 cm Tungsten array to single solid cylinder.

The mass of the moderator can then be found with the multiplication of the density of tungsten, 19.25 g/cm^3, and the calculated volume. The volume of the simulated moderator is simply the volume of the cell representing the moderator, approximately 996 cm^3, which is constant for each calculation. Therefore, the density supplied to MCNP will be the calculated mass of the moderator in question divided by the simulated volume for the moderator. For example, assuming tungsten vanes with a thickness of 0.254 mm, the calculated mass would be approximately 890 g, resulting in a simulated density of approximately 0.89 g/cm^3.

With the utilization of tally multiplier cards, MCNP is capable of calculating the product of the energy-dependent flux and any of the approximately 100 ENDF reactions. [34]

$$P = C\int \varphi\left(E\right)\sigma\left(E\right)dE \tag{2.1}$$

If $\sigma(E)$ is taken as the pair production cross section of tungsten, P represents the number of pair production reactions occurring in the moderator, $\varphi(E)$ is the energy dependent flux. In Eq.2.1, C is an arbitrary scalar constant which can be used to normalize the calculation. MCNP utilizes microscopic cross sections in units of barns (b). Therefore, if the constant C is taken as the atomic density, and has the form atoms/b/cm, the calculation results in the energy dependent reaction rate in units of reactions/cm^3. [34] The simulated density for each thickness is therefore converted to atomic density and supplied as the constant for the tally multiplier card.

Table 2-1. Constant values supplied to MCNP for the tungsten thickness optimization calculation.

Thickness (mm)	Simulation Density (g/cm^3)	Constant (b^{-1}cm^{-1})
1.00x10^{-6}	3.51x10^{-6}	1.15x10^{-8}
1.00x10^{-5}	3.51x10^{-5}	1.15x10^{-7}
3.50x10^{-5}	1.23x10^{-4}	4.03x10^{-7}
7.00x10^{-5}	2.46x10^{-4}	8.05x10^{-7}
1.40x10^{-4}	4.92x10^{-4}	1.61x10^{-6}
5.00x10^{-4}	1.76x10^{-3}	5.75x10^{-6}
1.00x10^{-3}	3.51x10^{-3}	1.15x10^{-5}
1.00x10^{-2}	3.51x10^{-2}	1.15x10^{-4}
1.27x10^{-2}	4.46x10^{-2}	1.46x10^{-4}
2.54x10^{-2}	8.92x10^{-2}	2.92x10^{-4}
6.35x10^{-2}	2.27x10^{-1}	7.44x10^{-4}
1.27x10^{-1}	4.46x10^{-1}	1.46x10^{-3}
1.91x10^{-1}	6.69x10^{-1}	2.19x10^{-3}
2.54x10^{-1}	8.92x10^{-1}	2.92x10^{-3}

The MCNP calculation is capable of determining the number of pair production events, which is taken as the number of positrons generated by the moderator, occurring in the moderator bulk, but only a small fraction of those positrons are capable of diffusing to the surface for emission. The production rate determined by MCNP must be multiplied by correction factors to determine the number of slow positrons emitted from the moderator.

$$R\left(\frac{slow\,e^{+}}{s}\right)=\varepsilon_{e^{+}}V_{eff}P \qquad 2.2$$

The production rate, R, is therefore the product of the surface branching ratio, ε_{e+}, the effective volume, V_{eff}, and the resulting production rate predicted by MCNP, P. The slow positrons surface branching ratio is the fraction of positrons reaching the surface of the moderator which are emitted as slow positrons. The factor V_{eff} denotes the volume of the moderator one diffusion length from the surface, and is called the effective volume. It is assumed that positrons created in this volume successfully reach the surface. This volume is taken as the product of the surface area of the moderator and the diffusion length of a positron in tungsten.

$$V_{eff}=SL^{+} \qquad 2.3$$

In Eq.2.3**,** S is the surface area of the moderator and L^{+} is the diffusion length.

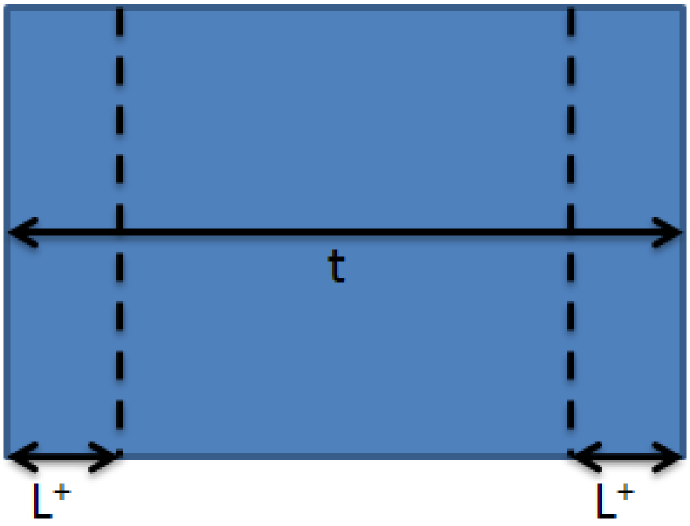

Fig. 2.5. Diagram showing the diffusion length, L^{+}, in relation to the thickness of the moderator.

The diffusion length, L_+, is the average distance traveled by a thermalized positron prior to annihilation. [7] It was assumed that any positron which thermalizes at a deeper depth cannot successfully reach the surface for slow positron emission. From literature, the diffusion length for tungsten can range from 50 nm for tungsten annealed at 1400 K [38] to 100 nm for a single crystal annealed to 2300 K [40]. It is therefore assumed that the effective volume for the tungsten used for the moderator will range from 0.0091 cm^3 to 0.0182 cm^3.

Gamma rays from fission products produce an additional photon spectrum which tends to soften over time because high energy gammas tend to be emitted more rapidly than lower energy gammas. While operating, fission fragments which emit high energy gammas are constantly being replenished, so the photon spectrum comes to equilibrium. [41] MCNP ignores the production of delayed photons while performing critically calculations. [34] Because these photons can have energies in excess of the pair production energy threshold, they must be considered for the positron production calculation. To compensate, a simple correction factor was introduced which determined the ratio of prompt photons to delayed photons. The prompt fission photon distribution, with energies in excess of 1 MeV, takes the form [41]:

$$\chi_p(E) = 8.0e^{-1.1E} \tag{2.4}$$

The delayed photon spectra can also be approximated by an exponential [41]:

$$\chi_d(E) = 6.65e^{-1.1E} \tag{2.5}$$

Both expressions result in the number of gamma rays produced per fission event per MeV. By integrating over the energy range, which is assumed to cover the fission photon energies, the ratio of delayed to prompt fission photons can be determined.

$$\frac{\chi_d}{\chi_p} = \frac{6.65\int e^{-1.1E}dE}{8.0\int e^{-1.1E}dE} \sim 0.8 \qquad 2.6$$

This implies that for every 10 prompt fission gammas, there should be approximately 8 delayed gammas. Therefore, multiplying the production results calculated by MCNP by a correction factor of 1.8 is a reasonable correction for MCNP to compensate for delayed photons,

$$P = P' + 0.8P' = 1.8P' \qquad 2.7$$

where *P'* is the raw data calculated by MCNP.

Figure 2.6 displays the results for the thickness calculation. The results are normalized to the maximum production rate, with the black points displaying the total production rate, the red points displaying the production rate in the first bank (the bank closest to the core) and the blue displaying the production rate from the second bank. At thicknesses less than the diffusion length, it is assumed all created positrons produced are capable of reaching the surface as thermal positrons. Therefore the production is simply dependent on the reaction rate. The probability of interaction of a photon within a thickness x is simply:

$$1 - \frac{\varphi(x)}{\varphi_o} = 1 - e^{-\Sigma_{pp}x} \qquad 2.8$$

where $\varphi(x)$ is the flux at a distance x, φ_o is the initial flux and Σ_{pp} is the macroscopic pair production cross section. This presence of this exponential term dictates the shape of the production curve at low tungsten thicknesses. Once the thickness of the tungsten is twice the diffusion length of positrons, the production rate begins to plateau. This can be attributed to the fact that positrons produced deeper within the moderator than the diffusion length cannot reach the surface for reemission and are lost. As the thickness continues to increase, the production rate begins to decrease because the volume of the first bank (the bank closest to the core) begins to attenuate more and more of the photons produced by the reactor, limiting the production in the second bank, where the extraction efficiency is higher.

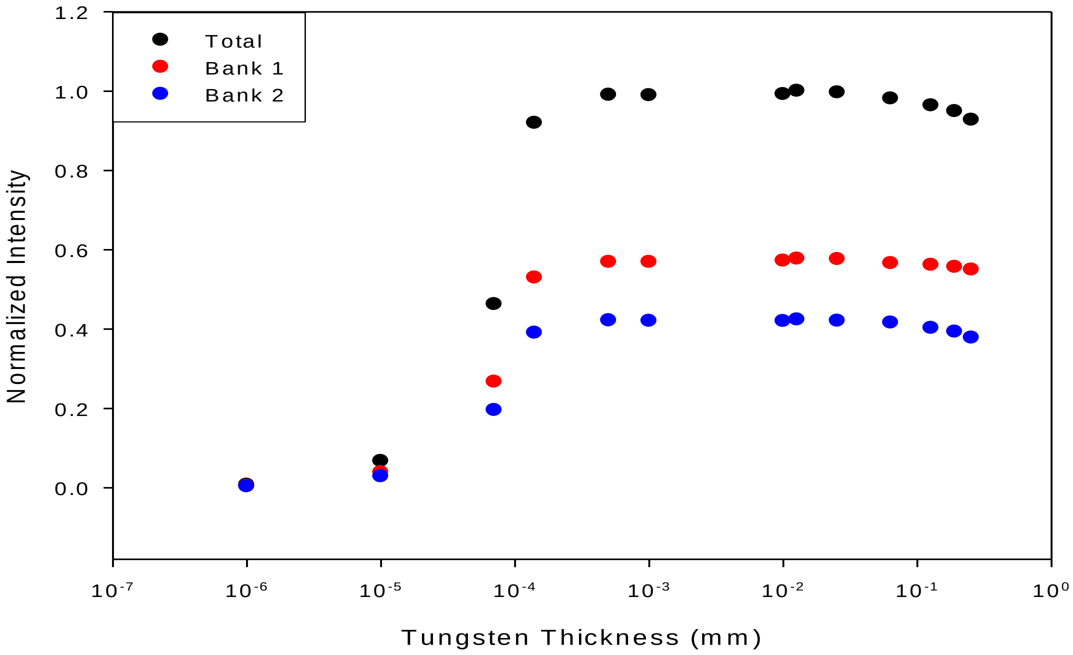

Fig. 2.6. Results of the MCNP tungsten thickness optimization calculations. The bank located closest to the face of the reactor core is labeled Bank 1 with the remaining bank labeled Bank 2.

The moderator was constructed from vanes with a thickness of 0.25 mm. While this is approximately 7% less than the maximum production rate, which occurs at a thickness of about 0.0127 mm, the increased thickness offers greater structural integrity to the assembled and annealed moderator. The product of the effective volume, surface branching ratio (taken as 0.25) and MCNP pair production rate yields a predicted slow positron production rate which ranges from (1.2-2.4)x10^9 s^{-1} for a moderator composed of 0.25 mm vanes, depending on the thickness of the diffusion length utilized for the calculation. [42] This positron production calculation included the thermal neutron capture gammas emitted by a cadmium shroud, which is discussed in the following section.

2.2.2 Cadmium Thickness Optimization

Thermal neutron capture reactions, in a suitable shroud surrounding the moderators, can be used to intensify and harden the gamma spectra through the moderators. A search was performed to determine the ideal material which would maximize the thermal neutron utilization and yield the highest energy gamma rays. The product of the number density of target atoms, the cross section and incident flux yields the reaction rate of a particular reaction,

$$R = N\sigma\phi \qquad 2.9$$

where R is the reaction rate, N is the number density, σ is the microscopic cross section and φ is the neutron flux. Therefore, the probability of a particular gamma emission to occur is simply the product of the flux and the microscopic cross section and the intensity of emission (Γ).

$$\Gamma\frac{R}{N} = \Gamma\sigma\phi \qquad 2.10$$

Assuming the flux to be invariant for the search, elements should be sorted based on the product of the intensity of emission and microscopic cross section. The results of this search indicated Cadmium and Gadolinium offered the best performance.[a] Large sheets of Cadmium (12”x12” in cross section) could be easily obtained, therefore this element was chosen to construct the shroud surround the moderator banks.

---

[a] Initial work sorting isotopes to optimize thermal neutron capture reactions performed by Dr. Jianwei Chen.

MCNP calculations were performed to optimize the thickness of the cadmium cap surrounding the vacuum can housing the moderator banks. The goal of this optimization was to maximize the rate of thermal neutron capture reactions while minimizing the effect of photon attenuation through the cadmium shroud. To accomplish this, repeated runs were performed with varying thickness of cadmium surrounding the vacuum can containing the moderator. The cadmium thickness was varied from 0 to 3 mm.

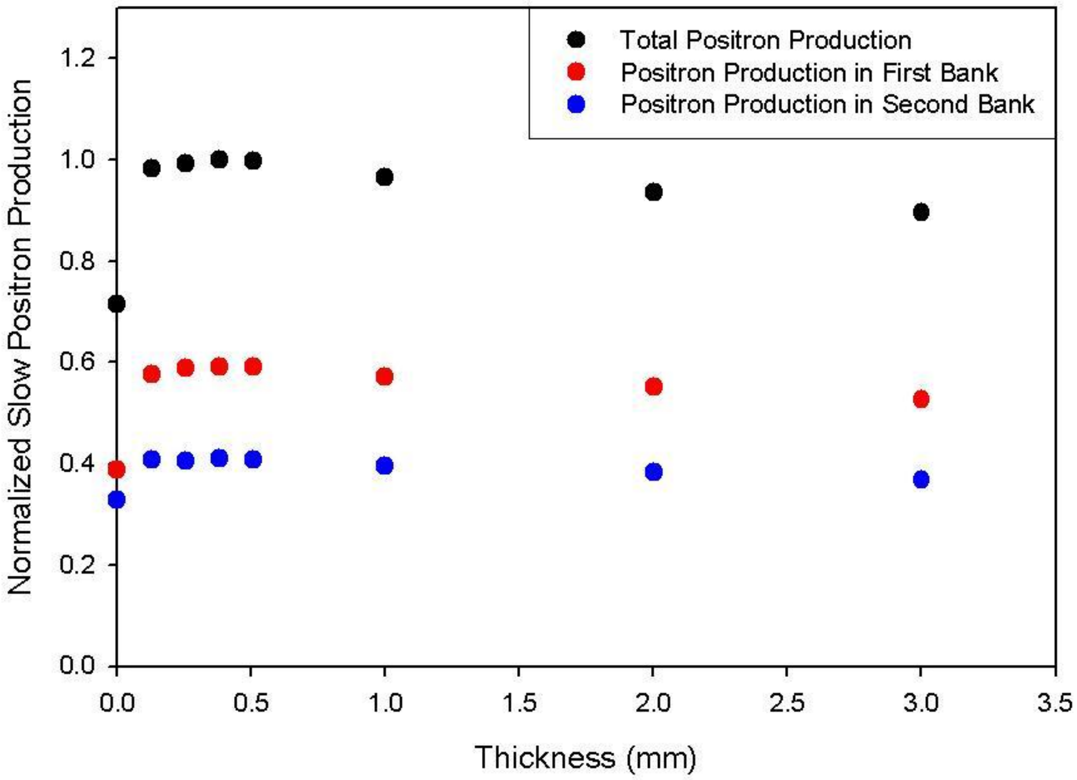

Fig. 2.7. Results of the MCNP cadmium thickness optimization. The bank located closest to the face of the reactor core is labeled Bank 1 and the remaining bank is labeled Bank 2.

These calculations demonstrated that the addition of 0.25 mm of cadmium can increase the positron production by nearly 39%, compared to using no cadmium. Thinner sheets do not capture all the available neutrons while a thicker cap begins to attenuate the photons produced by the core. This particular thickness can also be purchased in large sheets which can easily cover the entire vacuum chamber housing the extraction optics; therefore 0.25 mm cadmium sheets with a cross section of 12”x12” were utilized.

2.2.3 Slow Positron Survival within Moderator Banks

Calculations were performed to test the efficiency of various moderator configurations in an attempt to maximize the production and extraction of slow positrons from the moderator. As the length of the moderator is increased, the production of slow positrons increases because of the increase in volume, but the extraction efficiency decreases due to collisions of positrons with the walls of the moderator.

To test the extraction efficiency of various moderator configurations, a user program for SIMION [39] was created which simulated the physics of positron interactions with the surface of a material. If an emitted positron collided with the walls of the cylinder, a Monte-Carlo program was called which determined if the positron survived the interaction, with refection probabilities shown to be approximately 60% [43]. An emitted positron with kinetic energy greater than the work function of the moderating material can penetrate the surface where it can annihilate or be re-emitted as a slow positron. If this event occurs, the user program emits a positron with kinetic energy equal to the work function of the material, 2.8 eV for Tungsten [7], and it is given a random direction vector to mimic positron emission from polycrystalline tungsten. The positrons can also undergo elastic and inelastic collisions with the walls of the moderator. For an elastic collision, the incident kinetic energy of the positron is kept the same while the direction vector is randomized. For inelastic collisions, the direction vector and kinetic energy (up to the energy of the incident particle) is randomized. When necessary, the angle is randomized in a hemispherical direction away from the surface.

Positrons were flown from different positions with an increasing distance away from the exit of the moderator. The location of the positrons were recorded when the positrons impacted an extraction grid directly in front of the simulated moderator bank. Reaching the extraction grid indicated the positron was successfully extracted from the moderator. In addition to the position, the kinetic energy and component velocities of the positrons were recorded for use in focusing calculations.

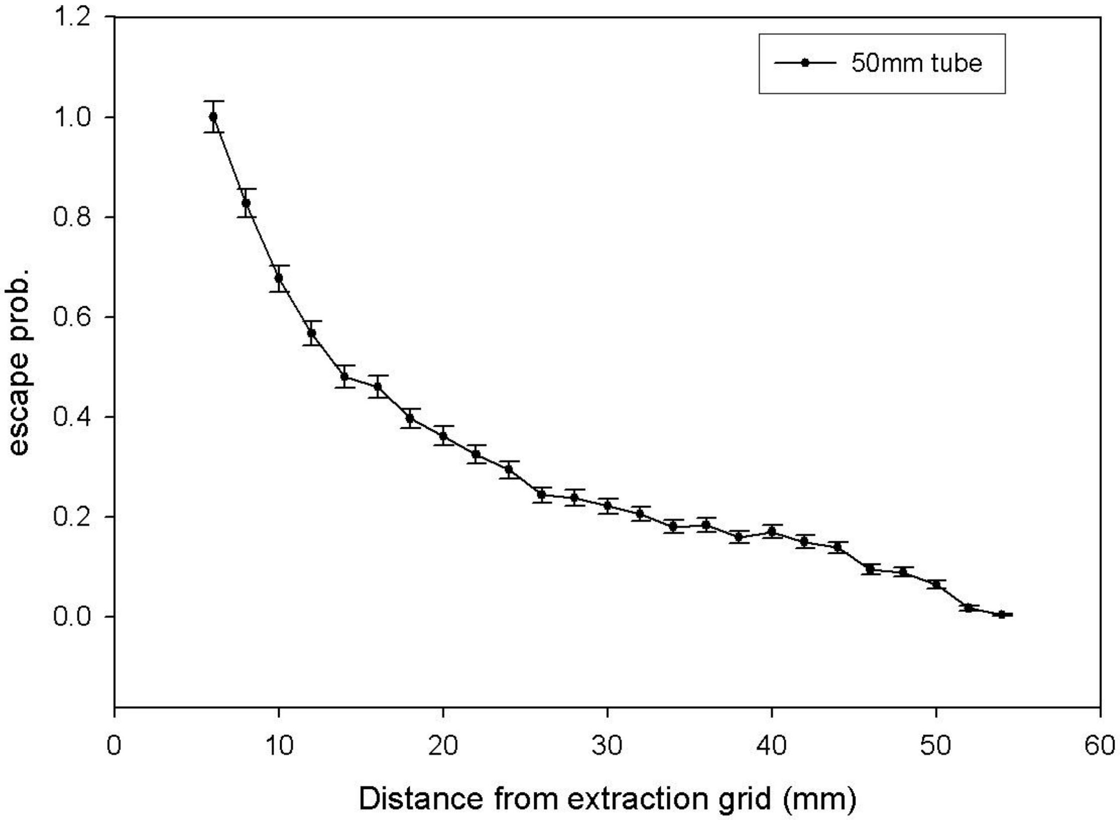

Fig. 2.8. Figure displaying the slow e^+ extraction efficiency for a 1 cm in diameter, 50 mm long tube versus the distance from the extraction grid of the bank.

The ratio of the number of positrons successfully reaching the extraction grid to the number of positrons emitted from a particular point resulted in the extraction efficiency for that particular location. [44] Figure 2.8 displays the extraction efficiency results for a 1 cm in diameter tube which is 50 mm long. The extraction efficiency is calculated to be 30.2%.

To increase the extraction efficiency, multiple shorter moderator banks can be used. By placing a potential difference between banks, positrons produced in the bank further away from the focusing optics can be extracted into the next, where the probability of escape increases. The potential difference between the banks produces a fringing field which penetrates the moderator tube, producing an electric field that pulls positrons from the first bank into the second, which is closer to the extraction lenses. Unfortunately, this field forces positrons emitted near the gradient in the second bank back into the surface, as seen in fig. 2.8, reducing the extraction efficiency. This can be remedied by placing a grid between the two banks at the same potential as the second bank. This eliminates the potential gradient, allowing positrons to travel further before being deflected towards the exit.

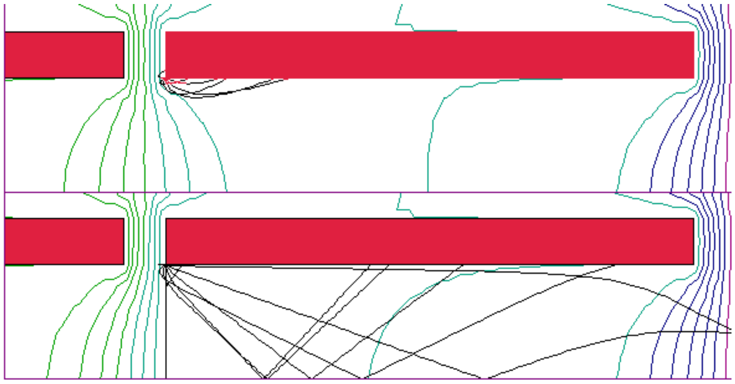

Fig. 2.9. Simulation displaying the effectiveness of grids behind the moderator bank. The top simulation contains no grid. The bottom simulation has a grid at the same potential as the moderator on the right. The first bank is on the left and second (closest to the extraction optics) is on the right.

Removing the fringing field at the end of the second bank minimizes the possibility that the positrons will be pushed back into the surface upon emission. The results for a case with and without grids can be seen in fig. 2.10

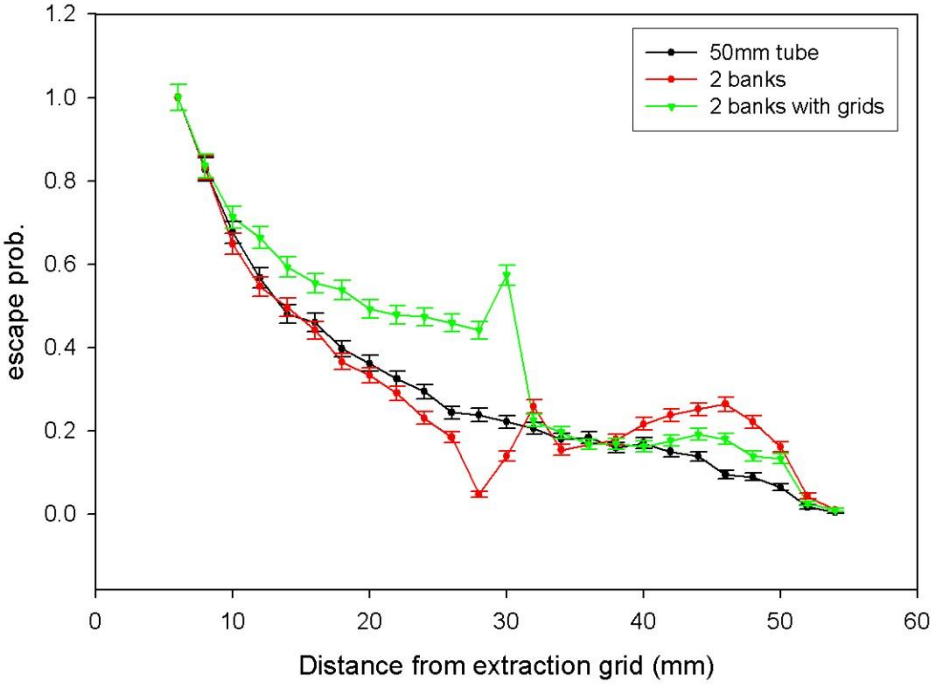

Fig. 2.10. Extraction efficiency results for a 50 mm tube, two 25 mm tube biased with potential difference and two 25 mm tubes with potential difference and grid between two banks.

The overall extraction efficiency for the cases with and without grids is calculated to be 38.4% and 30.9% respectively. The results of the simulation with grids indicate extraction efficiencies of 60% for the bank closest to the focusing optics with only 26% efficiency for the next bank. [42]

Further simulations were performed utilizing 4 banks separated by grids. These results indicated an additional two banks could increase to overall production by 29%. [44] Two moderator banks were utilized in the final design as a simplification for the initial testing of the positron beam, although the capability to add two additional banks was included.

2.3 Charged Particle Optics

With a complete knowledge of applied electrostatic and magnetic fields, the trajectories of charged particles traversing those fields may be analytically determined. A nonrelativistic charged particle with an initial velocity vector ***v***, traversing a region containing an electric and magnetic field will experience two forces. An electrostatic field will generate a coulombic force, **F_E**, given by:

$$\boldsymbol{F}_E = \frac{d(m\mathbf{v})}{dt} = q\boldsymbol{E} \tag{2.11}$$

where m is the mass of the charged particle, q is the charge and $\boldsymbol{E}$ is the electric field. Within a magnetic field, the charged particle will experience a Lorentz force defined as:

$$\boldsymbol{F}_B = \frac{d(m\mathbf{v})}{dt} = (q)\boldsymbol{v}x\boldsymbol{B} \tag{2.12}$$

where $\boldsymbol{B}$ is the spatial distribution of the magnetic flux density. The Lorentz force on the charged particle acts in a direction perpendicular to the velocity of the particle, $\boldsymbol{v}$, and magnetic field. The total force acting on the particle is the superposition of the two individual forces, [18]

$$\boldsymbol{F} = \frac{d(m\mathbf{v})}{dt} = q(\boldsymbol{E} + \boldsymbol{v}x\boldsymbol{B}) \tag{2.13}$$

With knowledge of the initial position and direction of the charged particle, the complete trajectory of the particle can be defined. For example, for a positron emitted from the origin with a velocity of $\boldsymbol{v}=(v_x,v_y,v_z)$, travelling through a uniform magnetic field defined as $\boldsymbol{B}=(B_x,0,0)$ and an electric field $\boldsymbol{E}=(E_x,0,0)$, from Eq.2.13, it follows that the equations of motion of the particle are solutions to:

$$m\frac{d^2x}{dt^2} = qE_x \tag{2.14}$$

$$m\frac{d^2y}{dt^2} = v_zB_x \tag{2.15}$$

$$m\frac{d^2z}{dt^2}=-v_yB_x \tag{2.16}$$

By defining the initial position (x,y,z) and initial velocity (v_x,v_y,v_z) of the particle, the complete path of the particle through the field region can be determined.

2.3.1 Electrostatic Extraction and Focusing Optics Optimization

SIMION 3D is an electrostatic and magnet simulation software which utilizes the finite difference technique of over-relaxation to estimate the potential of the non-electrode regions of a defined potential array. It seeks to iteratively solve Poisson's equation, Eq. 2.17, with boundary values supplied from arbitrary user defined geometry.

$$\nabla^2V=0 \tag{2.17}$$

Each non-electrode point is estimated as the average of the nearest neighboring points, which is demonstrated by fig. 2.11 and Eq.2.18 for a Cartesian coordinate system. [39]

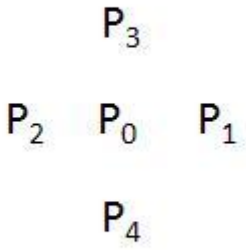

Fig. 2.11. Diagram of relationship between nodes for difference method of over-relaxation utilized by SIMION 3D.

$$P_{o,new}=\frac{P_1+P_2+P_3+P_4}{4} \tag{2.18}$$

For each iteration, the residual between the new calculated potential estimate and the previous estimate is decreased and the potential array is refined until residual is less that some specified criterion. While this technique works well for electrostatic modeling, SIMION is not intended to model true magnetic fields. It requires the use of potentials for refinement, but magnetic fields present themselves as flux. To model a magnetic field, magnetic poles must be defined. [39] Gradients in magnetic fields must be estimated with the use of shaped poles.

Because it was necessary to model magnetic field gradients located at the entrance of the solenoid, different modeling software was utilized. Field Precision offers a suite of software that can be used to model 3D (the AMaze software package) and 2D (the TriComp software package) electric and magnetic fields. [45]

As mentioned previously, the Monte Carlo routine written to determine the extraction efficiency of different moderator designs was able to record the location, kinetic energy and component velocities of particles emitted from the surface of a simulated moderator. This data could then be utilized as the initial particle parameters used in the optimization calculations for the extraction optics. This method offered a reasonable estimation of the of the phase space of actual particles emitted from the moderator, including internal positron bouncing within the moderator banks, rather than roughly estimating the perpendicular energy of surviving positrons and emitting them with the same energy in a fan of angles, as was performed for design calculations for the prototype beam. [36] The initial conditions required by AMaze and TriComp include: the mass, charge, kinetic energy, initial position coordinates (X,Y,Z) and the direction vector of the particles (or vector composed of the percentage of the particles momentum in a particular Cartesian direction [45]). The direction vector was taken as the vector described by the component velocities determined by SIMION.

The conceptual design of the extraction optics consisted of an extraction grid directly in front of the moderator, 6 lenses of decreasing diameter and a final drift lens running the length of the solenoid. After the first lens, which was simply a large diameter cylinder, the following three lenses were tapered. The reason for this taper was to allow the lenses to be located in a similar location as cylindrical lenses (which are easier to construct), but the edges of the lenses were removed from the trajectory of the positrons, freeing the internal volume of the extraction optics of obstructions.

Positrons were emitted from a plane at the inlet of the extraction optics. Placing a particular potential on the emission plane essentially mimicked the effect of biasing real moderators, increasing the kinetic energy of the emitted positron accordingly. A representative group of simulated positrons were emitted from the plane in increasing 1 cm increments from the center of the beam. Data was tabulated for each positron that reached a plane approximately 90 cm away from the emission point. This ensured that positrons had successfully been focused into the solenoid and through the magnetic gradient at the entrance of the solenoid. Once in the solenoid, it was assumed positrons safely reach the outlet of the reactor biological shield. The results of this optimization can be seen in fig. 2.12. The extraction efficiency is in excess of 95% up to 7 cm away from the center of the moderator, and still nearly 65% at 9.5 cm away from the center. The drift lens was held at ground and remaining lenses were biased accordingly. The voltages used in the final optimization simulation were, from the extraction grid to the lens 6: 910 V, 800 V, 735 V, 50V, -3100 V, 640 V and 0 V. [42] While the extraction efficiency for a particular location is shown to be in excess of 90% across a majority of the face of the moderator, this is not entirely accurate for the true overall extraction efficiency. The extraction efficiency at points further from the center of the beam must be weighted more due to the fact that the slow positron production is higher at larger radii, i.e. an annular ring of the moderator at a radius of 9 cm encloses more moderator mass and surface area than an annular ring of the same width at 1 cm. Weighting the extraction efficiency to compensate from this radial component reduces the overall extraction efficiency to approximately 80%. [42]

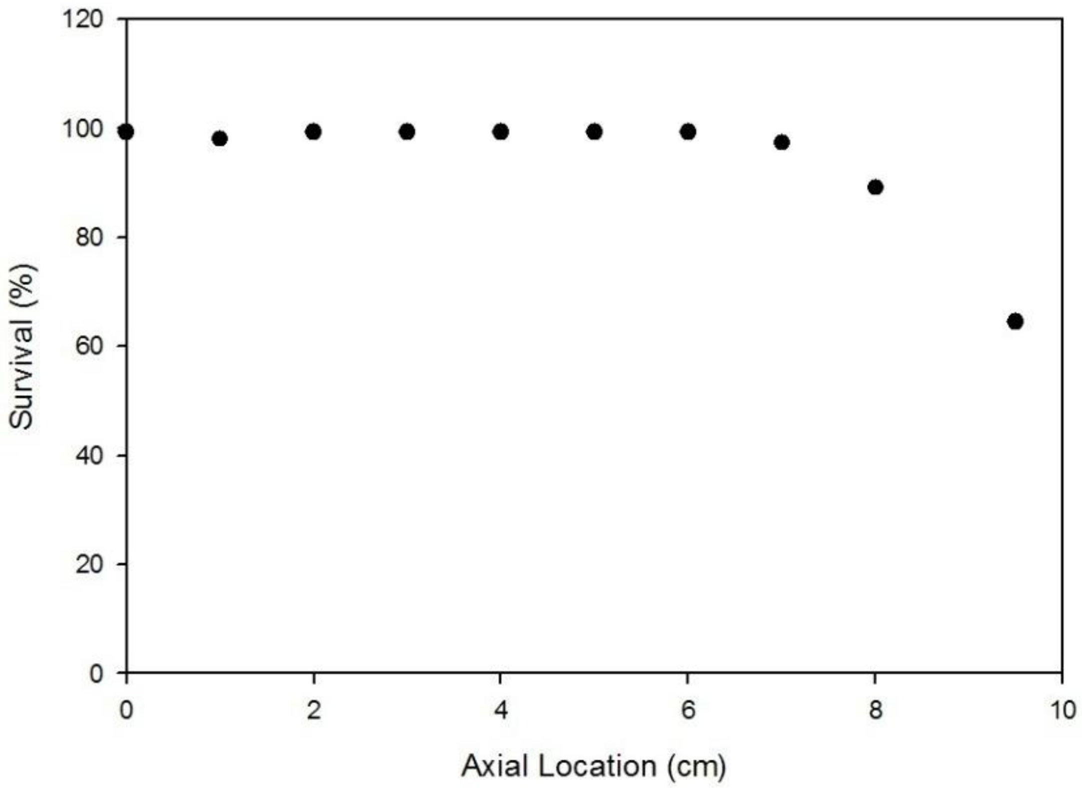

Fig. 2.12. Results of simulations predicting the extraction efficiency of positrons emitted from the moderator.

Figure 2.13 displays the results of the extraction optics calculation with some representative positron tracks. It becomes difficult to focus positrons further off axis due to the fact that high potentials are needed to push positrons emitted near the edge back to the center of the beam, which drastically reduces the efficiency of positrons emitted across the entire face of the moderator. After considering the calculated slow positron production from MCNP, the positron survival within the moderator banks and the efficiency of the extraction optics, the slow positron beam intensity was estimated to range from (4.1—8.2)x10^8 s^{-1}. [42]

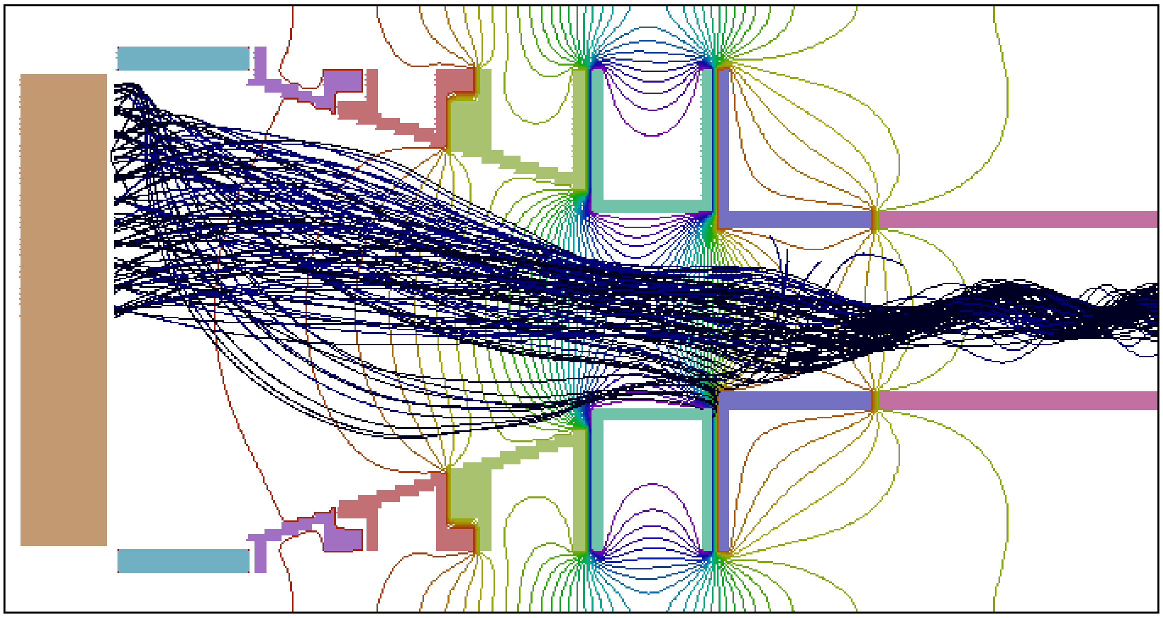

Fig. 2.13. Results of the slow positron extraction optimization produced by the TriComp ion optics software.

2.3.2 Magnetic Guidance Optimization

Measurements performed at the conclusion of testing of the prototype positron beam indicated the presence of residual transverse magnetic fields within the biological shield of the reactor. These fields are capable pushing positrons off the axis of the beam, causing annihilation with the walls of the vacuum chamber. To correct for these fields, sets of racetrack coils were placed along the body of the solenoid passing through the biological shield which can produce a resultant transverse field capable of steering the positrons through the residual transverse field back to the center of the beamline.

Simulations were performed to test the effectiveness of these racetrack coils on steering the beam. Two sets of these coils, set 90° apart, were modeled around the solenoid. Additional sets of square coils, again set 90° apart, were then modeled to surround the solenoid in a location that would correspond to the biological shield. Current supplied to these external square coils would then produce a transverse field which was capable of overcoming the applied axial field and could direct the positrons into the walls of the lenses. The orientation of these simulated coils can be seen in fig. 2.14.

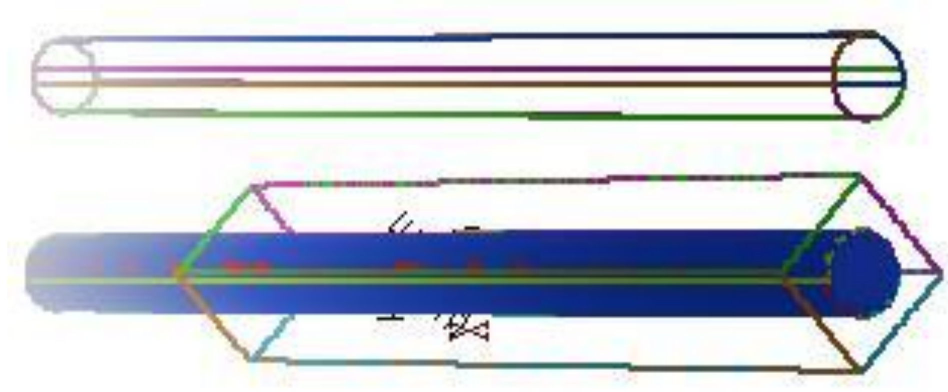

Fig. 2.14. Diagram of coils used to test effectiveness of steering coils. The blue cylinder represents the solenoid, the large rectangular coils produce a simulated residual field and racetrack coils run the length of the solenoid.

Figure 2.15 demonstrates that the simulation can produce a transverse field that can steer the beam into the walls of the drift lens. The goal of this optimization exercise was to see if the race track coils could negate this transverse field and steer the positrons back to the center of the beam, the results of which can also be seen in fig. 2.15.

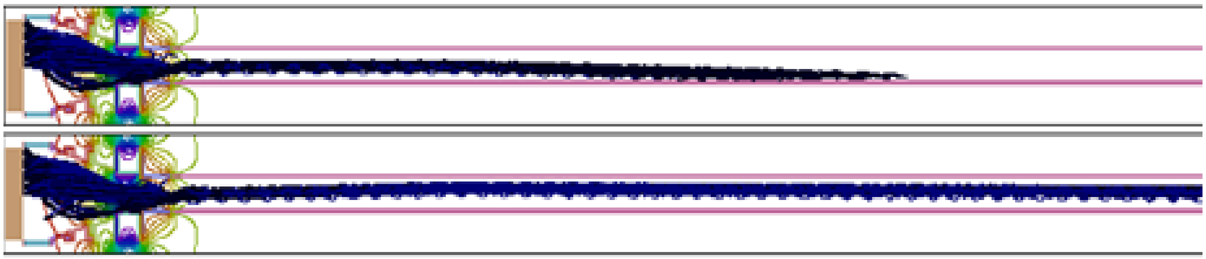

Fig. 2.15. Results of simulations demonstrating the effectiveness of the steering coils. Residual fields and capable of steering positrons off axis and into the walls of the lens, which can be countered with the use of steering coils guiding the positrons to the center of the beam.

Initially, positrons are directed off axis by the racetrack coils due to there being no residual field to negate. The simulation demonstrated that the resultant field generated by the superposition of residual transverse field and steering coils was able to steer the positrons back onto the axis of the beamline at the outlet of the reactor biological shield.

At the outlet of the biological shield, the positrons must be magnetically guided out of the neutron headlight of the beam tube to allow the placement of a beam stop. Positrons travelling in a curved magnetic field undergo two guiding center drifts, from gradients and curvature of the applied magnetic field. Gradients in magnetic fields cause the Larmor radius of a charged particle to be smaller in the high field region but larger in the lower end of the gradient. Generalized to three dimensions, the ∇**B** drift can be characterized as [46]:

$$v_{\nabla B} = \pm \frac{1}{2} v_{\perp} r_L \frac{\mathbf{B} x \nabla \mathbf{B}}{B^2} \qquad 2.19$$

where $v_{\nabla B}$ is the drift velocity, $v_{\perp}$ is the perpendicular components of the particles velocity, r_L is the Larmor radius [46]:

$$r_L \equiv \frac{v_L}{\omega_c} = \frac{m v_{\perp}}{|q| B} \qquad 2.20$$

and $\boldsymbol{B}$ is the magnetic field. In addition to ∇**B** drift, charged particles travelling in a curved magnetic field undergo a curvature drift due to centrifugal force acting on the particle. Where ∇**B** drift is characterized by the perpendicular component of the velocity, curvature drift is related to the parallel component [46].

$$v_R = \frac{m v_{\parallel}}{q B^2} \frac{\mathbf{R}_c x \mathbf{B}}{R_c^2} \qquad 2.21$$

In this expression, v_R is the curvature drift velocity, m is the mass of the particle, q is the charge, B is the magnetic field, $v_{\parallel}$ is the parallel component of the particles velocity and R_c is the radius of curvature of the magnetic field. In a curved magnetic field, these two drift components are added together resulting in [46]:

$$v_{\nabla B} + v_R = \frac{m}{q}\frac{\mathbf{R}_c x \mathbf{B}}{R_c^2 B^2}\left(v_{\|}^2 + \frac{1}{2}v_{\perp}^2\right) \qquad 2.22$$

This relationship can further be reduced by taking the unit vector of ***R*** $\boldsymbol{R_c}$ and ***B*** resulting in:

$$v_d = \frac{m}{qR_c B}\left(v_{\|}^2 + \frac{1}{2}v_{\perp}^2\right)\mathbf{R}_c x \mathbf{B} \qquad 2.23$$

Assuming the total energy of the positrons is 1003 eV, the resulting velocity is 1.88x10^7 m/s. With the additional assumption that the component velocities are separated by 45°, as a conservative assumption, the perpendicular and parallel velocities will be 1.33x10^7 m/s. With the a guiding field strength of 80 G and a radius of curvature of 0.2 m, the drift velocity, perpendicular to the curvature of the bend, can be found to be approximately 9.4x10^5 m/s. To determine the magnitude of the drift of the particle, the time the particle is in the curved magnetic field must be calculated as well. With particles travelling through a 45° angle (or 0.79 radians) with the 0.2 m radius of curvature, the arc length of the drift can be found by [47]:

$$S = \theta R_c \qquad 2.24$$

where S is the arc length and θ is the angle swept by the arc in radians, resulting in a length of 0.158 m. Because the arc length and velocity through the bend, the parallel velocity, is known, the time the particle spends in the curved field is determined to be approximately 11.9 ns. Therefore a conservative estimate for the amount of drift positrons will experience traversing a curved magnetic field is approximately 11 mm. Nearly 85% of simulated positrons fall within a diameter of 30 mm, while the diameter of the vacuum chamber which the positrons are traversing is nearly 100 mm, so the effect of the particle drift on the intensity of the beam should be negligible. This drift would not need to be corrected due to the fact that positrons are guided through an *S*-bend; therefore the drift off axis due to traversing the first bend is reversed by traversing a bend in the opposite direction.

A simulation was performed to ensure positrons could be successfully guided through a bent magnetic field. The 3D ion optics simulation package AMaze was utilized to simulate the bent magnetic field. The model consisted of two solenoids, at 45° apart, with the bend simulated with a 45° segment of a torus. The results of the previous calculation, focusing of positrons from a moderator face into the guiding solenoid, were used to provide the starting trajectories for this simulation. This mimics the behavior of actual positrons emitted from a moderator and focused into a solenoid, rather than estimating the phase space of positrons and emitting a few positron trajectories. The simulation, as seen in fig. 2.16, clearly demonstrates the magnetic field gradient produced by the bent solenoid and the resulting drift caused by the curvature and gradient drift, which is shown to be approximately 1 cm. Further simulations of the *S*-bend demonstrate positrons guided off axis due to the first bend successfully return to the center of the beamline while traversing the second opposite bend.

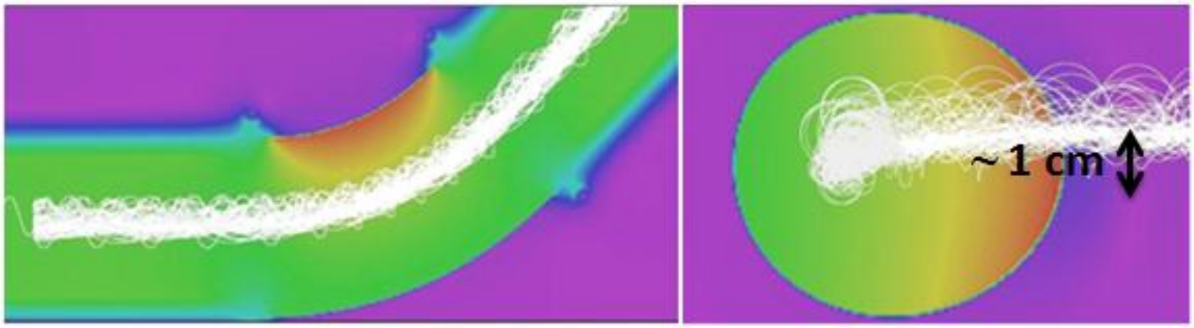

Fig. 2.16. Simulated particle trajectories through a bent solenoid.

Once out of the radiation headlight, positrons must be steered to the spectrometer in use. As mentioned for the *S*-Bend, positrons traveling through curved magnetic fields undergo guiding center drifts. Unlike the *S*-bend, positrons travelling through a potential switchyard will not undergo a bend in the opposite direction to correct any resulting drifts. To account for this, the concept of the positron beam switch yard consists of large diameter coils placed on gimbals, sharing a common center point. The large diameter coils are capable of producing a field which can bridge the gap in the magnetic field between the two solenoids used to guide the beam.

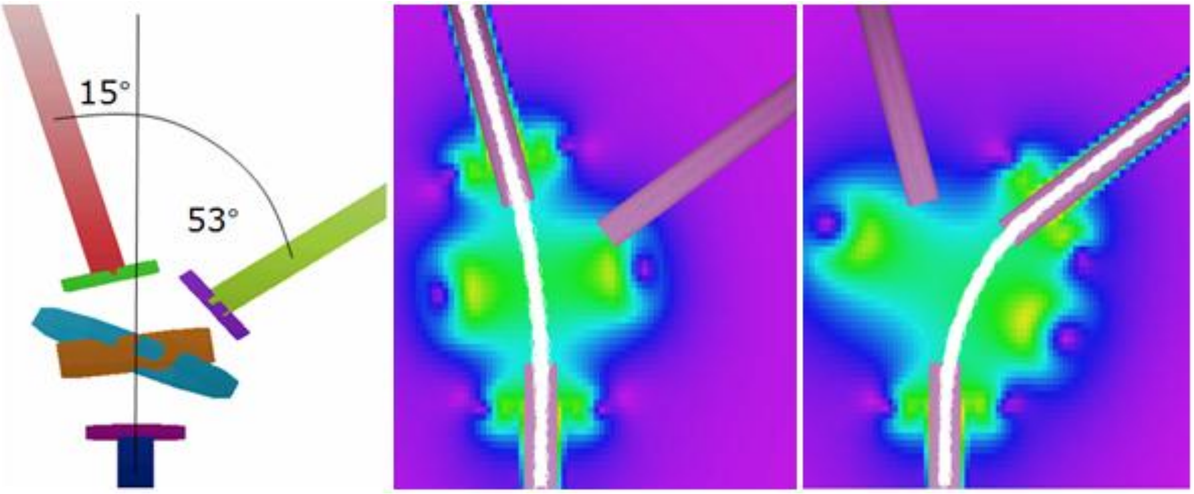

Fig. 2.17. A schematic of the coil placement for a concept first beam switchyard. This is capable of compensating for particle drifts.

These coils can rotate in the direction counter to any drifts resulting from the curvature of the field, i.e. the beam can be steered into the inlet of the desired solenoid. Additional coils are placed at the end of the solenoids to provide additional fine tuning of the particle guidance. Providing current to the desired array of coils produces the magnetic field which guides positrons to the respective spectrometers, either directly to the Ps-PALS spectrometer or to the second switchyard which then guides positrons to the e^+-PALS spectrometer, as seen in fig. 2.18.

The advantage of the concept is the positron beams enter the labs at perpendicular angles to the walls, removing the need for additional steering. The switchyard design was tested using the AMaze simulation suite. Positrons emitted from the simulated moderator are first guided through the main solenoid and *S*-Bend portions of the beam. At the outlet of the *S*-Bend, the positron's position, direction vector and energy are recorded, with the data taken as the starting position for the switchyard simulation. Simulations indicate the efficiency of this switchyard design is in excess of 96%.

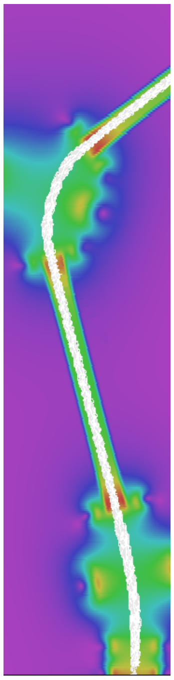

Fig. 2.18. Results of beam guidance simulation through two switchyards to e^+-PALS spectrometer.

The principle of using coils to correct for charged particle drifts can also be applied to the *S*-bend. Coils must be used to bridge gaps in the magnetic field where vacuum chamber crosses are located, which provide locations to attach feedthroughs and vacuum pumps. For the *S*-bend, additional coils can be used to provide a bridging field into the 45° solenoid. The advantages of this are a magnetic coil is easier to wind than a bent solenoid and the coil can be manipulated to guide positrons through the bend and correct for drifts. Figure 2.19 displays the results of the optimization simulation of the *S*-bend. Helmholtz coils are used to bridge the gap in the axial field due to the placement of a vacuum chamber cross. This is followed by a coil rotated to 22.5° at the center of the bend to bridge the gap. Termination coils are located at the outlets of the 45° solenoid to provide an additional magnetic field to bridge gaps.

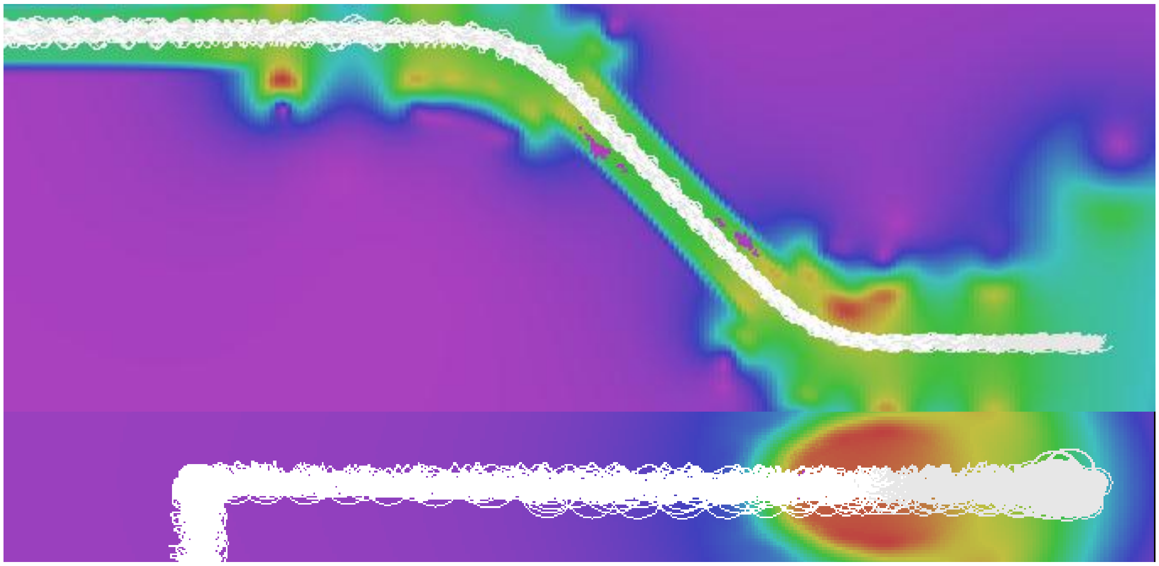

Fig. 2.19. Results of simulations demonstrating the effectiveness of steering slow positrons through the S-bend at outlet of biological shield.

Figure 2.19 also demonstrates how tuning the coils in the bend can compensate for gradient and curvature drift. The reason for the sharp bend seen in the figure is because the positrons are sent through the first beam switch and out of the solution volume.

2.4 Design and Construction of the Intense Slow Positron Beam

2.4.1 Moderator Design and Construction

The final design of the moderator consisted of two banks composed of 0.25 mm Tungsten strips, forming an interlocking matrix of 1x1 cm cells. To assemble the moderator, small slits had to be cut into these strips. This was achieved using Electrical Discharge Machining (EDM). Electrical Discharge Machining is the process of removing material from an electrically conductive material using an electric discharge. For EDM machining, a small electrode is placed very close to the surface of the material to be machined. The electrode never actually touches to surface to be machined, but the application of a high voltage causes an electric discharge between the electrode and material, resulting in the vaporization and melting of the piece. [48] Care must be taken to use Tungsten wire to cut the moderators. Other materials could introduce impurities into the tungsten moderator which can reduce the moderation efficiency, therefore reducing the number of positrons emitted from the moderator.

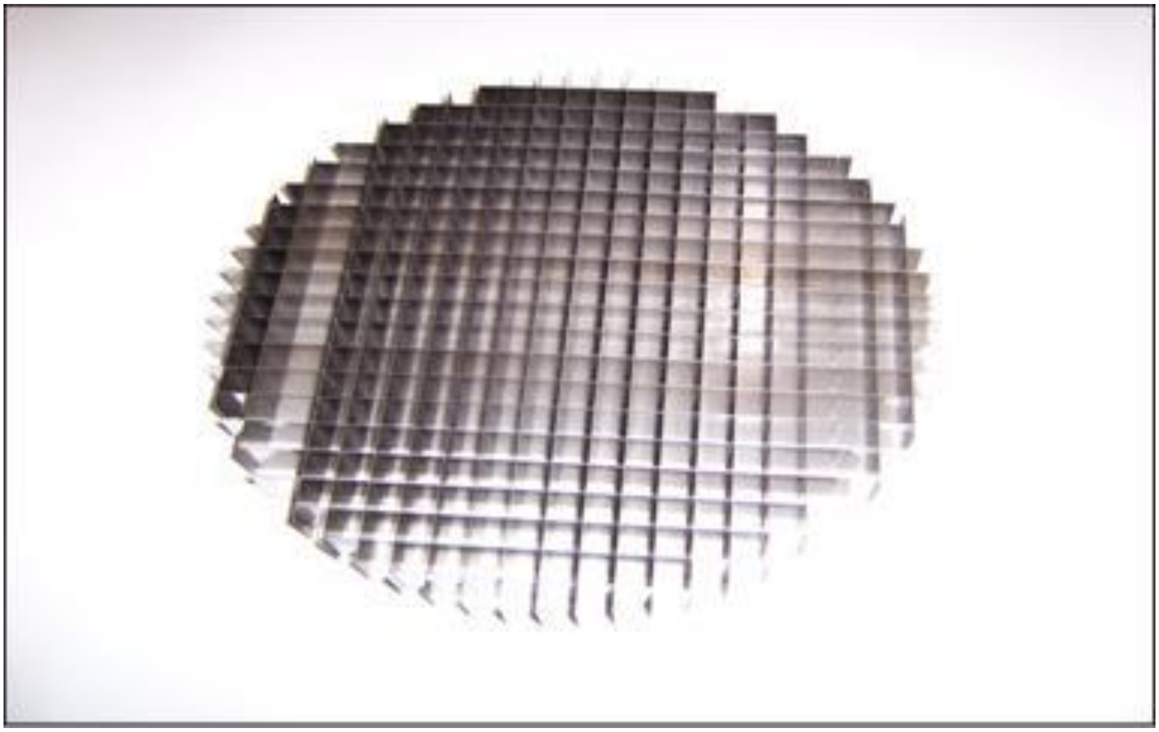

Fig. 2.20. Image of an assembled tungsten vain moderator.

Once constructed, the moderators were cleaned, followed by an etching process to remove the outer layers of tungsten. The moderator was first cleaned of organic surface contamination by submersion in a mixture of 30% hydrogen peroxide and concentrated ammonium hydroxide. This was followed by submersion in a solution consisting of 0.1 M nitric acid and 0.1 M potassium nitrate contained in a stainless steel dish, with the moderator insulated from the pan by placing it on a small insulating dish. A thin tungsten wire was attached to the moderator to serve as a contact for a MPJA DC power supply, model 9312-PS. The supply leads were connected to this contact and also attached to the wall of the stainless steel dish. This allowed the application of a constant 1 A current, resulting in a potential difference between the moderator and dish. As the tungsten oxide (WO_3) layer formed, the voltage rose on the power supply and the color changed to a dark blue. The current was removed when the voltage reached approximately 40 V, or when electrical arcs could be seen between the moderator vanes. After the surface was anodized, the moderator was placed in a solution of 0.1 M potassium hydroxide, which stripped the tungsten oxide layer, leaving a fresh tungsten surface. This process was repeated 10 times resulting in the removal of approximately 330 nm of tungsten.

Once cleaned, the moderators were annealed in a high temperature vacuum furnace at the High Temperature Materials Laboratory at Oak Ridge National Lab (ORNL). This furnace had an all tungsten hot zone approximately 30x30x30 cm. This was large enough to anneal an entire assembled moderator. The initial moderators were annealed individually in the event of damage occurring during the annealing process, e.g. sintering to a tungsten hearth plate which supported the moderator in the furnace, thermal stresses, etc. The moderator was annealed in vacuum at a temperature of approximately 2200 K for 4 hours, during which time the pressure increased from $6x10^{-6}$ to $5x10^{-5}$ mbarr, then allowed to cool overnight. The same process was performed for the second moderator bank. The annealing process did not damage the moderators, so future moderators can be annealed simultaneously. After annealing, the moderators were transferred to North Carolina State University under vacuum using a simple desiccator, where they were promptly installed in the beam and returned to high vacuum. [42]

2.4.2 Extraction Optics Design and Construction

The extraction optics lenses were fabricated from 6061 aluminum. Six lenses, and an extraction grid, were utilized to extract slow positrons from the moderators and focus them into the solenoid for magnetic guidance through the biological shield. Each of the lenses was machined from single blocks of aluminum.

A drift lens ran the length of the solenoid, which served multiple purposes; to guide the wires supplying high voltage, shield the drifting positrons from the applied voltages and allow the possibility to float the beam if it were necessary. The drift tube was split in half lengthways using a waterjet cutting procedure. The surfaces were then smoothed and a layer of Aerodag G was applied to provide a conductive coating on the inside surface. Aerodag G is an aerosol graphite spray and was applied to all aluminum components which held a potential. Aluminum components develop a thin oxide layer when exposed to air. It is possible that this oxide layer can influence the resulting electric field due to non-uniform charge from the thin insulating layer which could vary in thickness, therefore the application of the graphite layer results in a surface with constant conductivity. Once the surfaces were prepared, the lens was reassembled using support rings, alternating in composition between aluminum and Macor**,** to hold the individual halves together. The Macor rings were wide enough to insulate the drift lens from the walls of the vacuum chamber, while the aluminum rings simply offered electrical contact between the two halves and maintained the shape of the lens. The Macor rings were machined with holes in the wall to aid in pumping. Aluminum oxide tubes, with an outer diameter of 0.125", were installed which spanned the Macor rings, down the length of the lens, and provided guides for the wires used to supply high voltage to the extraction optics. Once the wires were installed, the drift lens was inserted in the solenoid.

The extraction optics of the positron beam consisted of 6 aluminum lenses and one extraction grid, as seen below.

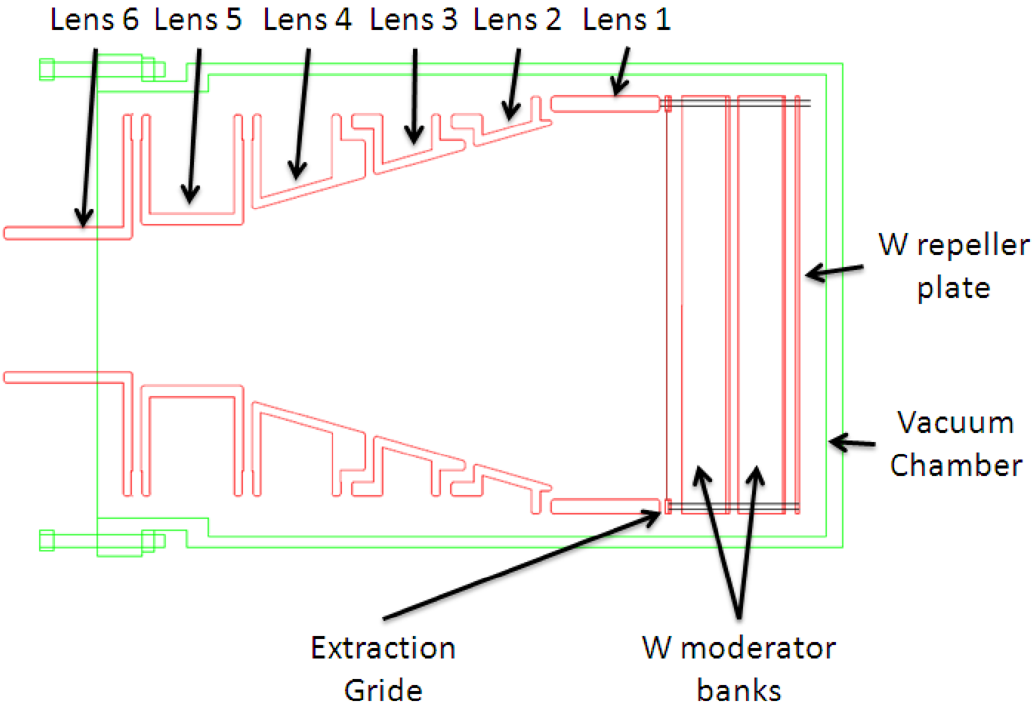

Fig. 2.21. Diagram of the extraction optics of the second generation slow positron beam.[b]

The extraction grid consisted of a tungsten grid sandwiched between two aluminum support rings placed directly in front of the tungsten moderator banks. The first lens was a cylinder

---

[b] Image courtesy of Dr. Jeremy Moxom, North Carolina State University.

with a diameter of 9.4”, with an inner diameter of 8.75”, and a height of 2.45”. The following three lenses were tapered at 15.8°. This taper brought the inner diameter of the lenses from 8.35” to approximately 4.3” over the length of the three lenses. The remaining two lenses were cylindrical with inner diameters of 3.625” and 3” on the fifth and sixth lenses, respectively.

The electrostatic lenses were designed to be supported by the sixth lens, which was mounted to the vacuum chamber flange housing the extraction optics using a circular array of 0-80 threaded rods.

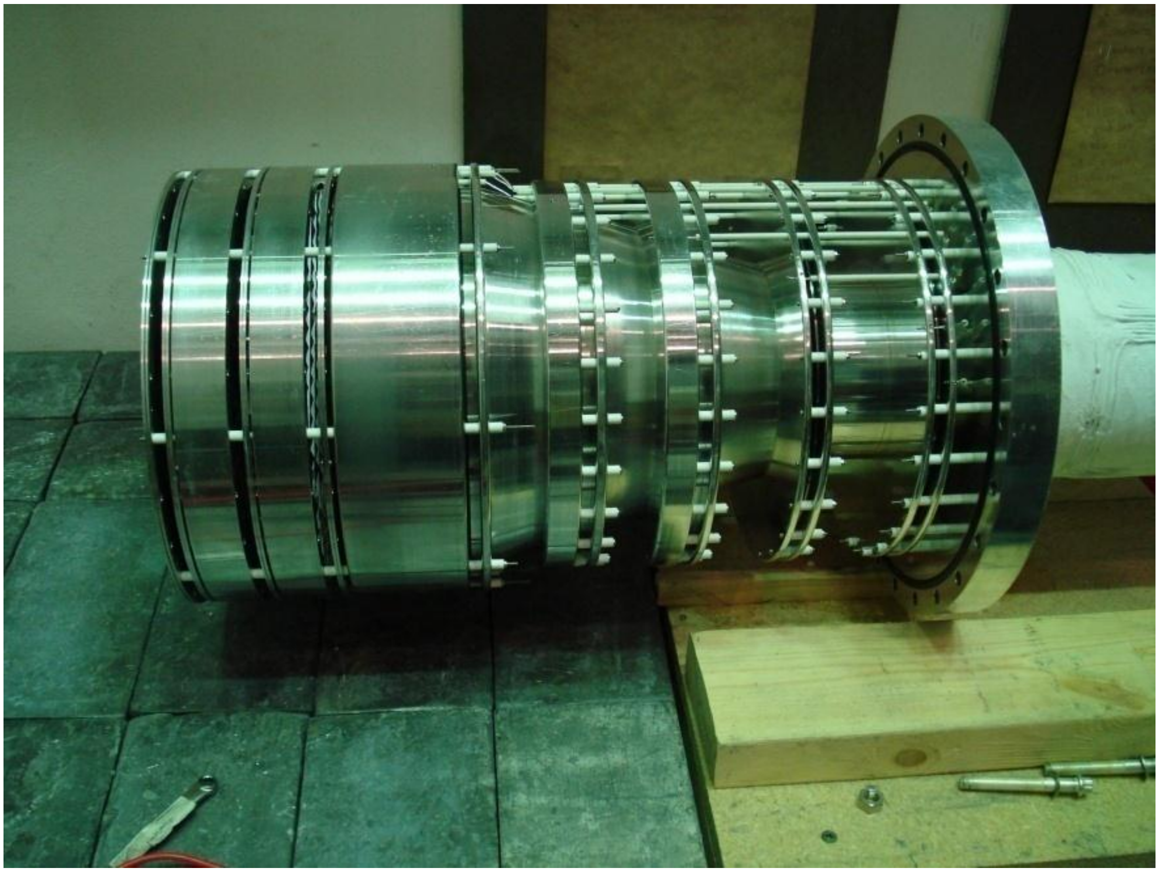

Fig. 2.22. Profile image of the assembled extraction optics of the slow positron beam.

Alumina tubes and spacer sets, purchased from Kimball Physics, Inc., were placed on the 0-80 threaded rods which served to electrically isolate the lens from the vacuum chamber and support the remaining internal components. The aluminum wire used to supply high voltage to the lenses were drawn through the lens assembly, isolated using the alumina tubes.

The remaining lens, extraction grid and moderator banks were supported from the final tapered lens using alumina tubes and 0-80 threaded rods. The interior face of each lens was coated in a layer of Aerodag G to ensure a well conducting surface providing a constant electric field. A thin sheet of tungsten, sandwiched between aluminum collars, acted as a repelling plate for the moderators and an extraction grid was constructed in the same way using a tungsten mesh. As can be seen in fig. 2.23, additional wires were drawn through the lens assembly to allow for the possibility to add an additional two banks of moderator arrays in the future.

Fig. 2.23. Images of the slow positron extraction optics with (right) and without (left) the moderators installed.

2.4.3 Vacuum Chamber Design

A single vacuum chamber is utilized to house the extraction optics of the beam and support the solenoid which guides positrons out of the reactor biological shield. A single 4” aluminum pipe was used to act as the vacuum chamber through the biological shield.

Aluminum cannot be welded to the typical stainless steel conflat flange, so a custom flange was utilized. The bulk of this 6” flange was machined of aluminum to allow the flange to be welded to the vacuum chamber, but a stainless steel surface was fused to the aluminum which contained the knife-edge required for sealing conflat flanges. A circular plate was attached to the opposite end of the vacuum chamber. A 0.28” groove, with an inner diameter of 9.66”, was machined in this flange to allow an o-ring to seal the solenoid vacuum chamber to the end cap. This end cap was 16.8” long and 10.9” in diameter and was machined from a single piece of aluminum to reduce the possibility of failure of the vacuum chamber at welds. Initially a Viton o-ring was utilized to seal the chamber but the resulting outgassing proved problematic, therefore this o-ring was replaced with a c-ring style seal made of aluminum, manufactured by High Tech Metal Seals of Belgium.

A customized cross was designed to support the positron beam at the outlet of the biological shield. This cross was fabricated at Nor-Cal Products and was composed entirely of aluminum. Because the cross contained aluminum conflat flanges, aluminum o-rings were required for sealing. The high voltage feedthrough was attached at this point to supply the potentials to the positron beam lenses. The cross also served as the pumping station of extraction portion of the beam. The pressure could be measured here using a glass envelope ionization gauge and a gate valve was installed allowing the front end of the vacuum system to be isolated from the rest of the beam line, therefore high vacuum could be maintained for this end of the beam, which houses the tungsten moderators, even with the rest of the beam at atmospheric pressure. A Varian Turbo-V 301 Navigator turbopump was utilized to maintain the vacuum of the beam. This pump has a pumping speed of 250 l/s [49] for nitrogen and could bring the pressure at the pumping station below 4×10^{-8} mbarr. A Varian Dry Scroll pump was used as the roughing pump for the turbo pump.

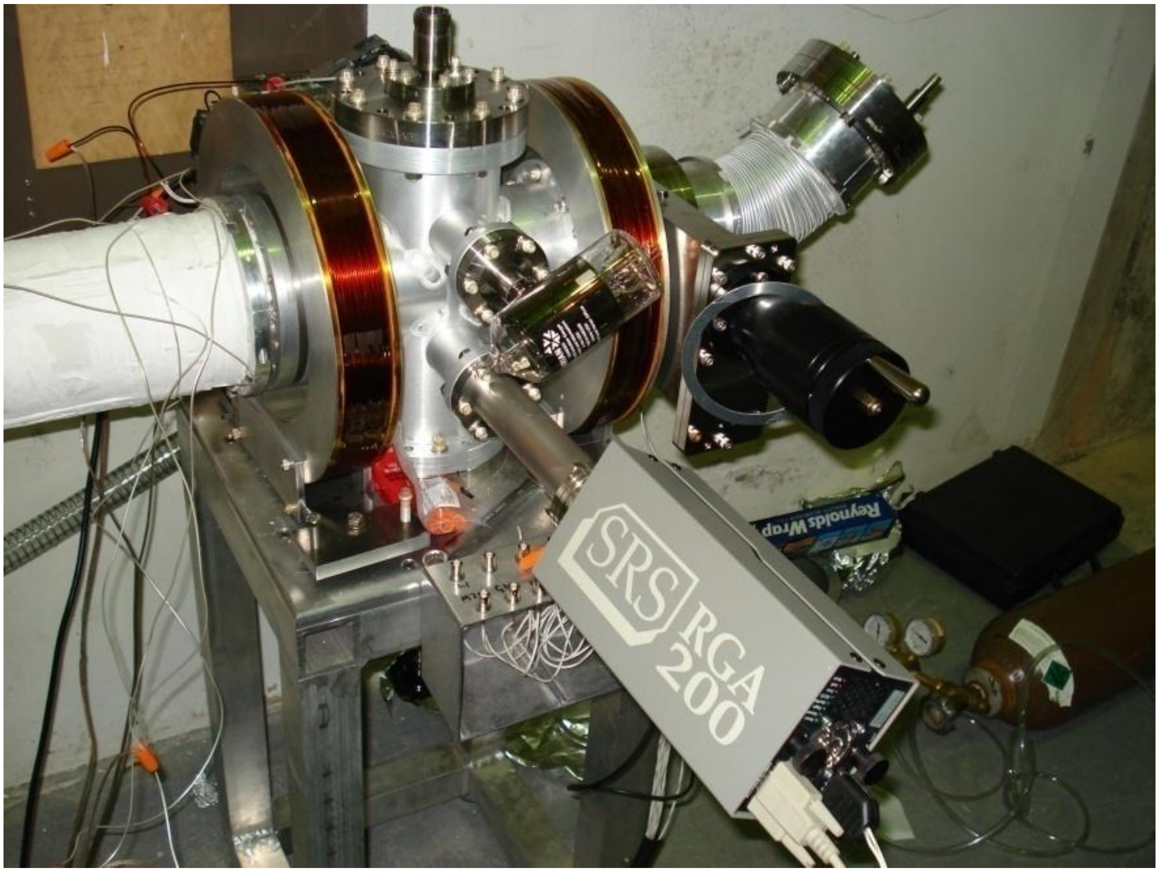

Fig. 2.24. Image of the pumping station of the reactor end of the slow positron beam.

The vacuum chambers for the switchyards were approximately 18” in diameter and constructed from stainless steel. The size of the chamber allowed plenty of room for the positrons to be guided to the desired destination. Each chamber contained a pumping port where a Varian Turbo-V 301 Navigator turbopump was attached, with rough pumping supplied by a Varian Dry Scroll pump. The switchyard chambers were designed with a removable lid. This allowed easy access to the inside of the chamber for cleaning and the ability to add internal lenses if the need ever arose. This lid was sealed using a standard large diameter elastomer o-ring. A 2-3/4” flange was also installed on each for the placement of pressure gauges if desired. A solenoid valve was installed on each roughing pump within the shielding cave. In the event of a loss of power, the solenoid valve would close, preventing a loss of vacuum.

Fig. 2.25. Images of the vacuum chambers for the two positron beam switchyards.

Many of the vacuum chambers were simply straight 4” tubes composed from stainless steel with 6” conflat flanges for sealing. These chambers connected the two switchyard chambers and lead from each switchyard into its respective spectrometer, penetrating the shielding. The 45° bend in the vacuum chamber was achieved by utilizing two standard 45° bends and a straight section making up the difference in height. This angled chamber was connected to the switchyard using a small bridging chamber. If additional moderators were installed in the beam, this small bridging chamber could be removed to make up for the additional length added to the front-end of the beam due to the addition of the moderators.

2.4.4 Magnetic Coil Design and Construction

An overview of the magnetic guidance system used to transport positrons from the moderator banks to the respective spectrometers can be seen in fig. 2.26. The solenoid guiding positrons through the biological shield of the reactor consisted of two layers of 8 gauge aluminum magnet wire, with a square cross section and aluminum oxide insulation, purchased from Oxinal, Inc..

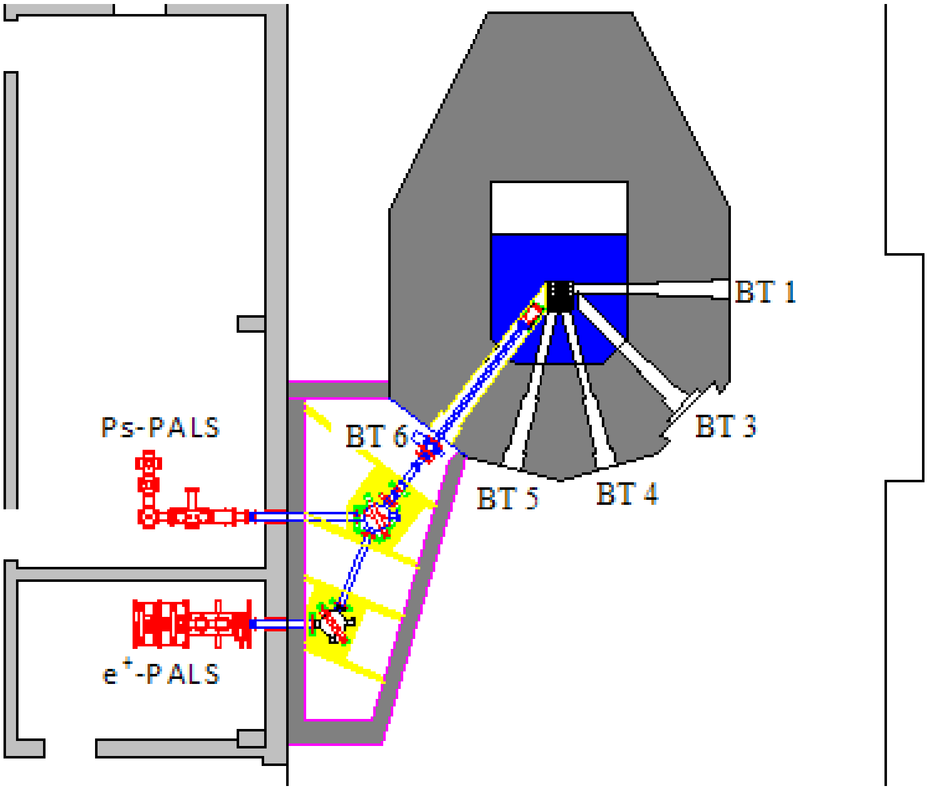

Fig. 2.26. Schematic overview of the positron beam from the vicinity of the core to the respective spectrometers.

This solenoid was wound directly on the vacuum chamber, the outer surface of which was first smoothed of rough patches and cleaned. The vacuum chamber was mounted to a welding positioning head, from All-Fab Corp., which could rotate the vacuum chamber at a constant speed, therefore pulling wire around the surface. The opposite end of the vacuum chamber was cradled between two rollers to support the weight of the solenoid and allow it to rotate. A layer of 3” wide aluminum oxide fabric tape, Cotronics Ultra Temp 390, was first wound around the support to insure the layers were electrically isolated from the vacuum chamber. While composed of high purity aluminum oxide fibers, this non-woven tape [50], is capable of being cut with scissors or simply torn. The tape layer was adhered at the ends of the solenoid using a ceramic adhesive, Resbond 989F from Contronics Corp, which was composed of mostly high purity alumina. [50]

Fig. 2.27. Image of the solenoid vacuum chamber mounted on welding positioning head prior to winding the solenoid.

When dry, the potting material formed an eggshell like consistency, which glued the fabric tape ends to the surface. The seams of the winding were then covered in the potting material, further strengthening the layer. Following the application of this insulating layer, the first layer of the solenoid was wound.

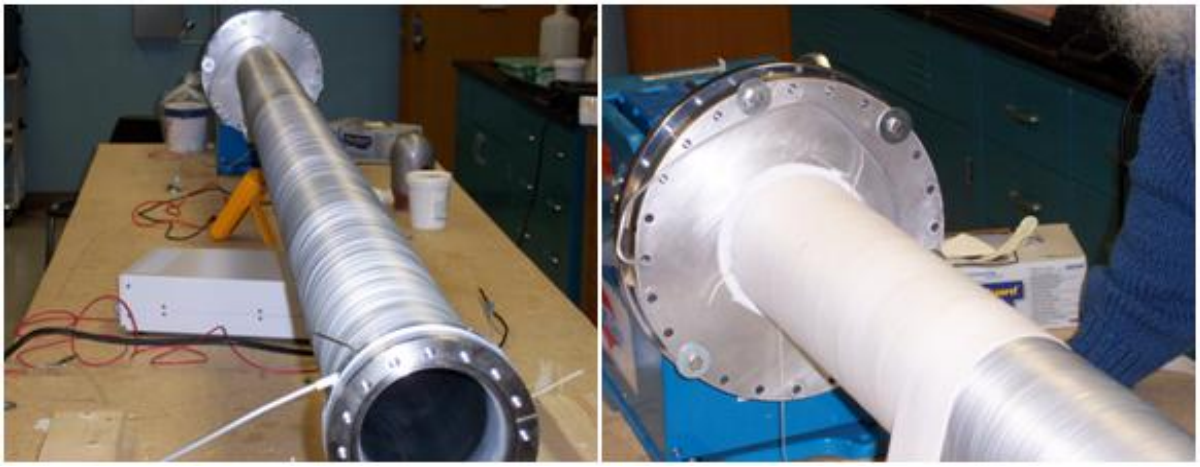

Fig. 2.28. Images taken during the winding of the main solenoid of the slow positron beam.

Care was taken to insure the wire did not twist as the coil was being wound to insure the resulting layer was a flat surface. After the first layer was wound, another layer of the 3" aluminum oxide fabric was applied to electrically isolate the two solenoid coil layers. One final layer of the aluminum wire was wound to complete the solenoid, followed by an additional layer of the 3" aluminum oxide fabric to protect solenoid.

The proposed racetrack coils were applied to the outer surface of the solenoid, on top of the aluminum oxide layer. These coils consisted of five loops of 14 gauge aluminum wire, circular in cross section and insulated with aluminum oxide manufactured by Oxinal, Inc., and conformed to the surface of the solenoid.

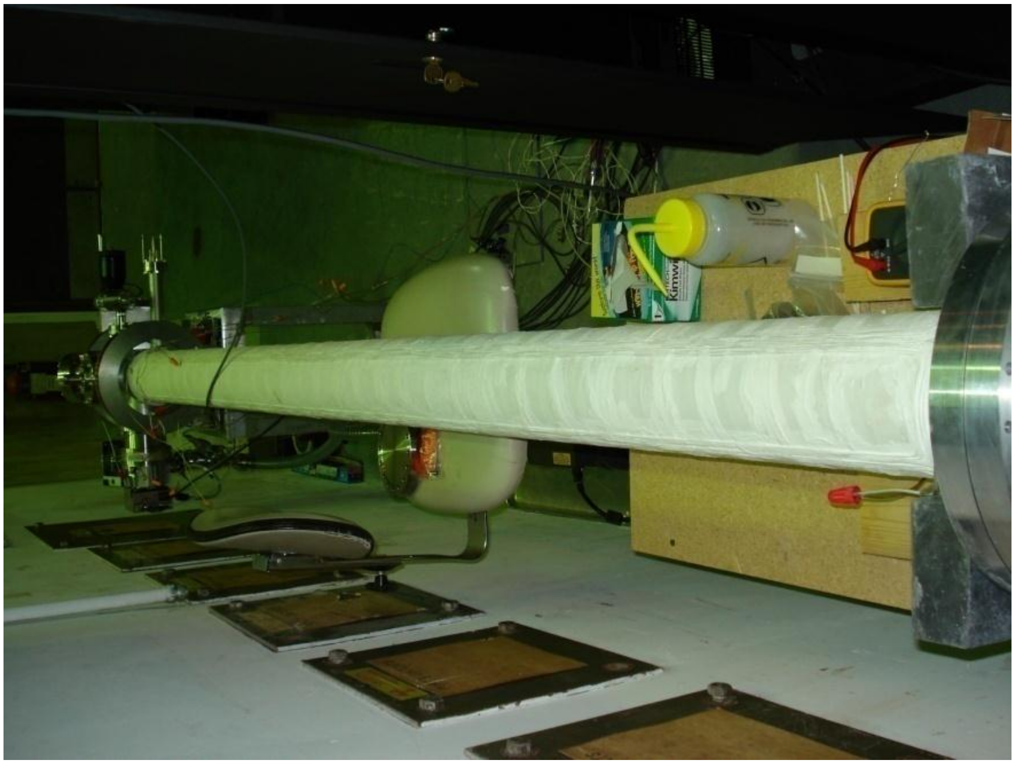

Fig. 2.29. Image of the completed solenoid used to transport positrons through the reactor biological shield. Racetrack coils run the length of the solenoid and are positioned 90° apart.

Two sets of coils were placed at 90° of each other. These coils were simply adhered to the beam using the Resbond 989F potting material used as glue for the aluminum oxide fabric.

The remaining long straight vacuum chambers served as forms for solenoids. Copper magnet wire with enamel insulation was used for these solenoids because they were far enough from the high neutron field that activation and damage to the enamel insulation was not expected. Because of the quantity of wire needed for the project, two venders were utilized, MWS Wire Industries and REA Magnet Wire Company, Inc. Because this wire was more robust, there was no need to wrap the vacuum chambers in the aluminum oxide fabric, although rough patches on the surface were smoothed. The welding positioner head was again used to wind these coils. Each of these solenoids consisted of two layers. A collar was applied to one end of the vacuum chamber to provide a flat surface for the coil to wind against, although the opposite end of the coil was free. After winding of the solenoids was completed, approximately three inches at the ends were wrapped in Kapton tape to prevent the coils from unwinding.

Coils with an outer radius of 6”, and inner radius of 4”, were used to bridge gaps in the axial field. A chuck was installed on the welding positioner, which could expand and clamp onto the inner surface of the coils. After mounting the coils on the chuck of the positioner, the edges and rough points of the coil form were smoothed. A layer of Kapton tape was utilized to isolate the magnet wire from the coil form. For these coils, 12 gauge copper magnet wire, with enamel insulation, was used. During the winding process, the coil was checked for shorts to ground after each layer was wound. After the coil was complete, a layer of Kapton tape was wrapped around the coil for protection.

The magnetic fields for the switchyard were produced with large diameter coils mounted to gimbals suspended from an aluminum plates. Most of the remaining coils where suspended from gimbals, allowing the individual coils to move freely about two axes. The first switchyard consisted of two gimbals which allowed the coils to share a common center and steered positrons either into the Ps-PALS spectrometer or send positrons to the second switchyard. The coils were large enough to surround the circular vacuum chambers of the switchyard. The larger of the two coil forms had an outer diameter of approximately 31", and produced a coil with a cross-section of 3"x3". The smaller coil had an outer diameter of 23" and had a cross-section of 1.25"x5". The second switchyard was constructed in a similar manner, except only one large diameter coil was needed to steer the positrons into the e^+-PALS spectrometer.

Fig. 2.30. Image of the gimbal and coil forms used to guide positrons through the first switchyard.[c]

---

[c] Image courtesy of the Precision Instrument Machine Shop, North Carolina State University.

These coils were wound with 10 gauge enamel insulated magnet wire, with a square cross section. These coils were too large and heavy to wind with the welding positioner used previously for winding; therefore they had to be wound by hand. Braces were attached to the coil which allowed it to be suspended on steel bar which served as an axle. This axle was then inserted into a cart which allowed the coil to spin freely by hand.

Fig. 2.31. Image of the coils used for the first positron beam switchyard.

As with the small coils, the large coils forms were first smoothed of rough patches and a layer of Kapton tape was used to cover the bottom of the coil form. The coil form was turned by hand which pulled wire onto the form. As with the small coils, the coil was checked for shorts after each layer. After winding, the coils were wrapped in Kapton tape for protection.

2.4.5 The Positron Beam Shielding Cave

In addition to the radiation shielding which surrounds the outlet of the biological shield and solenoid, a cave was constructed to house all the magnetic optics of the system. This allowed easy access to the positron beam in the event repairs are needed, without the need to dismantle most of the shielding.

A track was installed in the front of beam tube 6, extending in a radial direction away from the biological shield, with a turntable installed at the opposite end. A cart was placed on this track to allow the movement of the positron beam into beam tube 6. The positron beam was cantilevered from the cart, freeing the opposite end from supports, which allowed it to be pushed into the beam tube without a great deal of difficulty. Because one end of the positron beam was free from supports, a counterweight of lead was used to keep the cart from tipping over. This counterweight of lead also served as a beamstop for beam tube 6. The reason for the turntable was to enable the positron beam to be removed from beam tube 6 and rotated away towards the wall of the shielding for storage. This allowed the beam tube to be sealed and flooded, allowing the reactor to operate without the positron beam in place.

Fig. 2.32. Image of the cart and track used to support and guide the slow positron beam into beam tube 6 of the PULSTAR reactor.

The positron cave consisted of interlocking preformed concrete slabs and shared one wall with the adjacent radiography beam shield. Steel forms were constructed and filled with concrete. The rear wall of the positron cave was 18” thick, although the slabs against the northwest wall were only 12” thick. The shield against the northwest wall was designed with a cutout section to accommodate the location of the turntable. This cutout section was filled with a layer of lead and covered with 3” of borated polyethylene. The door of the positron cave was a prefabricated steel frame and door, filled with 7” of concrete. The interlocking blocks were lowered into place using the reactor bay crane. Once the individual blocks were in place and level, they were welded to each other. The roof of the shield also consisted of interlocking concrete blocks. Roof blocks were placed at both the front and back of the shield, working towards the center, where a cap block was used to bridge the two segments. In the event that the reactor bay crane is needed for work inside the cave, the roof can be removed and set aside for access.

Fig. 2.33. Images of the assembly of the positron beam shielding cave.

Chapter 3 Intense Slow Positron Beam Testing

3.1 Out-of-core Testing of the Intense Slow Positron Beam

Prior to insertion into beam tube 6 of the PULSTAR reactor, the slow positron beam went through an array of bench top testing. This was to ensure the beam was functioning properly without having risk of activation and contamination. The goals were to ensure the moderators could successfully convert gamma-rays into slow positrons and the extraction optics were functioning properly. Figure 3.1 displays an image of the positron beam while set up for out-of-core testing.

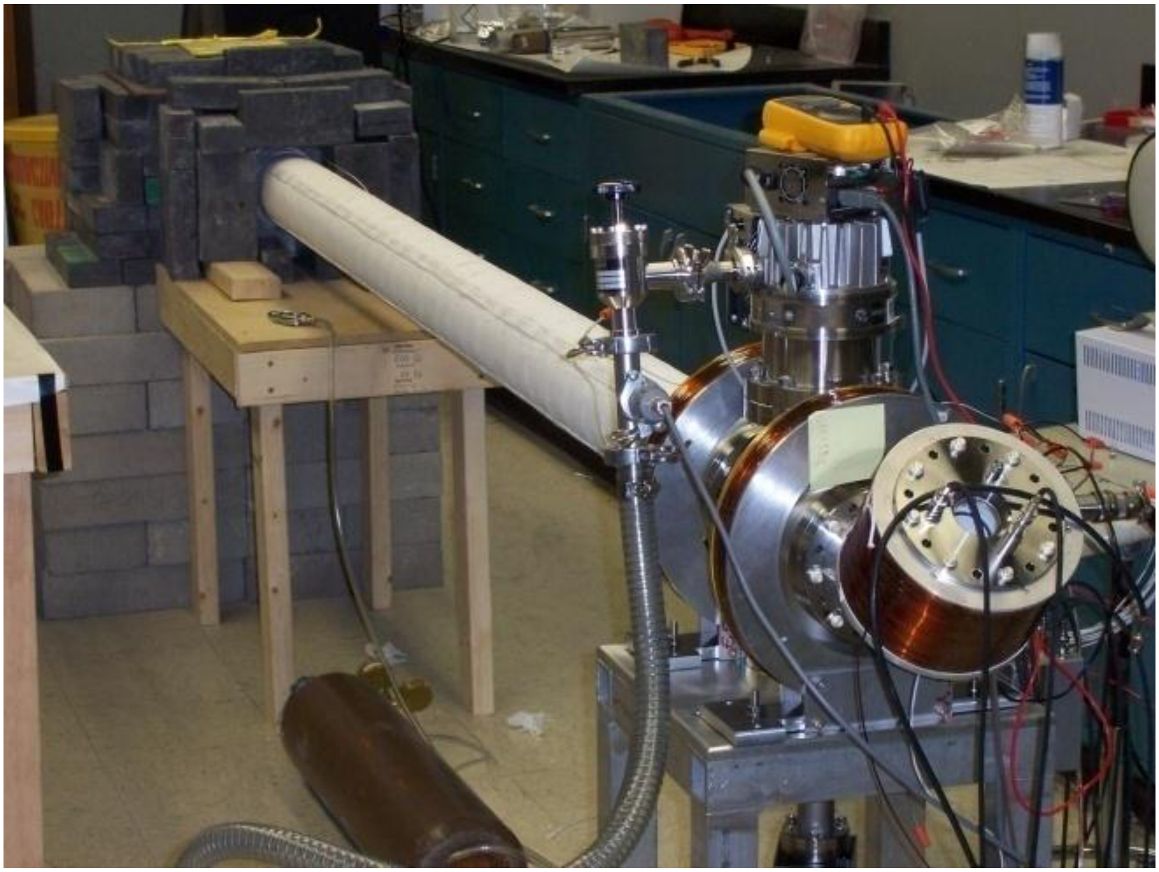

Fig. 3.1. Image of the intense slow positron beam while undergoing bench top testing.

3.1.1 Electron Gun Testing of Extraction Optics and Guidance

The focusing characteristics of the extraction optics were tested using electrons prior to testing the efficiency of slow positron production. Four electron sources were produced by placing Tungsten hairpin filaments 2 mm behind a plate which served as an anode. Electrons were extracted through 2.5 mm holes in the anode plate, the first hole being on axis and the fourth located 90 mm off axis. Each of the electron guns were separated by 30 mm. The anode plate was then mounted at the end of the extraction optics, replacing the moderator banks. The anode plate was biased to -910V, relative to ground, with the filaments biased to -30V relative the anode, to mimic the positron energies used in simulations. A current was supplied to the tungsten filament resulting in the emission of electrons.

The extracted electrons were imaged at the far end of the positron beam, after the pumping station, using a high luminosity P-22 (ZnSiAg) phosphor screen with a diameter of 3.8 cm (Kimball Physics Part Number PHOS-RP22GL-C7X7-R1500). The resulting image demonstrated successful focusing of each of the electron guns, each electron gun producing a circle on the phosphor screen, into a diameter of less than 3.75 cm. The electron gun tests provided valuable information on the performance of the extraction optics. Electrons emitted from the outer radius were greatly influenced by the voltage placed on lens 1; pushing electrons back to the center of the beam where they can be attracted by the high voltage lenses. Lenses 2 and 5 were relatively insensitive to the focusing. The drift lens and lens 6 were grounded. [42]

Fig. 3.2. Image demonstrating the effectiveness of the extraction optics of the slow positron beam using electron guns and phosphor screen.

The influence of the steering coils on the guidance of the beam was also tested using the electron gun. Only the axial electron gun was used to test the steering coils, which were able to guide the beam in both the up and down direction and the left and right direction. [42]

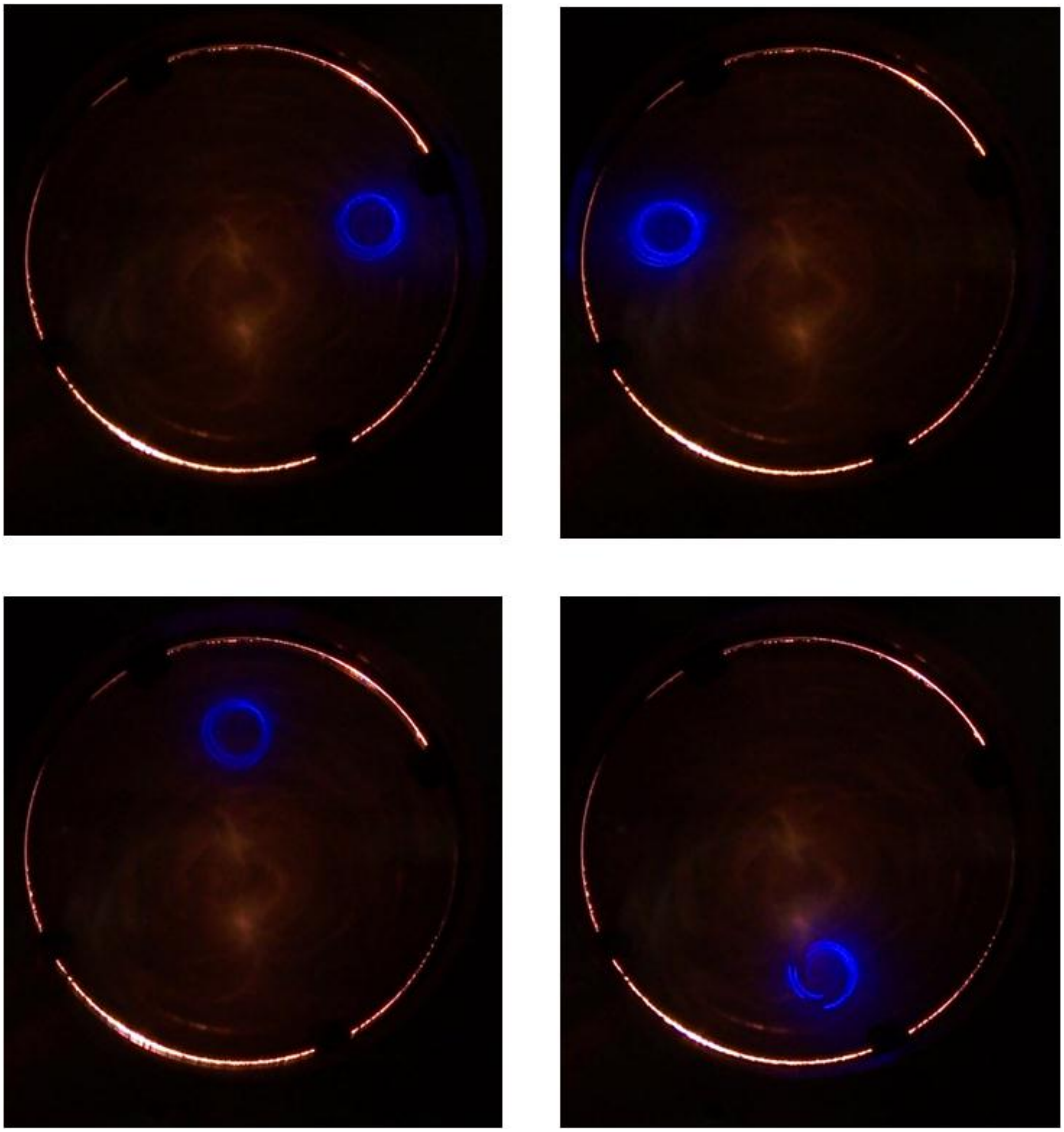

Fig. 3.3. Image demonstrating the effectiveness of the steering coils of the slow positron beam.

3.1.2 Na-24 Radioisotope Testing

Following the electron gun testing of the extraction optics, the annealed moderators were placed in the positron beam. The radioisotope sodium-24, Na-24, was utilized to test the ability of the moderators to generate slow positrons. Sodium-24 has a half-life of 14.7

hours and decays via the emission of a β^- particle and two prompts gammas with energies of 1.37 and 2.75 MeV. Because of the short half-life, the source was produced multiple times. The isotope was generated in the PULSTAR reactor by the irradiation of 9 g of $NaNO_3$ for up to 11 minutes. This resulted in calibrated source activities ranging from 4.6 to 44 mCi.

A micro-channel-plate (MCP) detector (El-Mul, part #: DC209/2) was utilized to measure the number of slow positrons generated. The detector was expected to have a detection efficiency of approximately 60%. The signals from the anode were processed by an Ortec 584 CFD operated in leading edge mode. The pulses were counted using an Ortec 871 counter/timer.

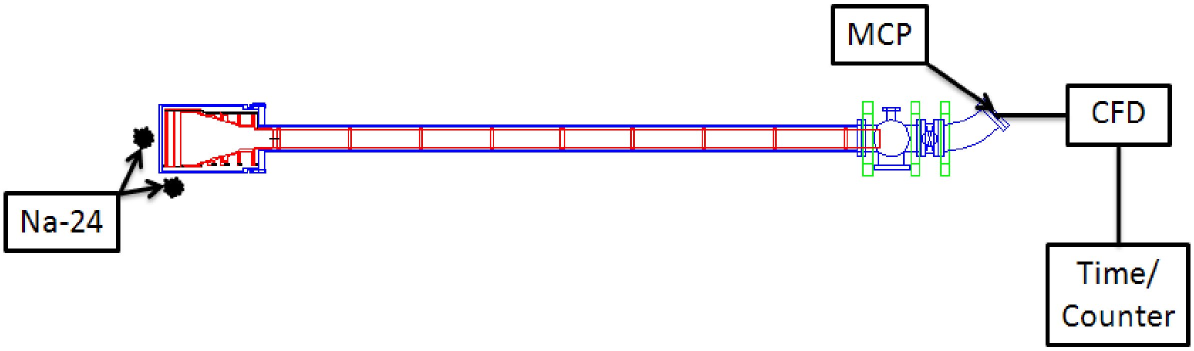

Fig. 3.4. Schematic overview of the out-of-core testing. This figure demonstrates the location of the MCP detector and the two source locations.

Once a count rate above background (approximately 2 counts/sec) was found, the rate was verified to be slow positrons by varying the applied voltages on the extraction grid. If a higher positive potential, relative to the moderators, was placed on the extraction grid, slow positrons generated by pair production in the moderators would be repelled away from the extraction optics, resulting in a drop in the count rate. Sodium-24 was therefore utilized to optimize the electrostatic lens voltages and the currents supplied to the magnetic coils guiding the slow positrons to the detector.

Data was collected with the source placed in two locations, one with the source as close as possible to the side of the moderators and one with the source placed at the center of the vacuum chamber behind the moderators. With the source on the side, both moderators were irradiated equally, so the relative contribution of each moderator bank to the beam was determined. Figure 3.5 demonstrates the typical data collected during the optimization of the lenses.

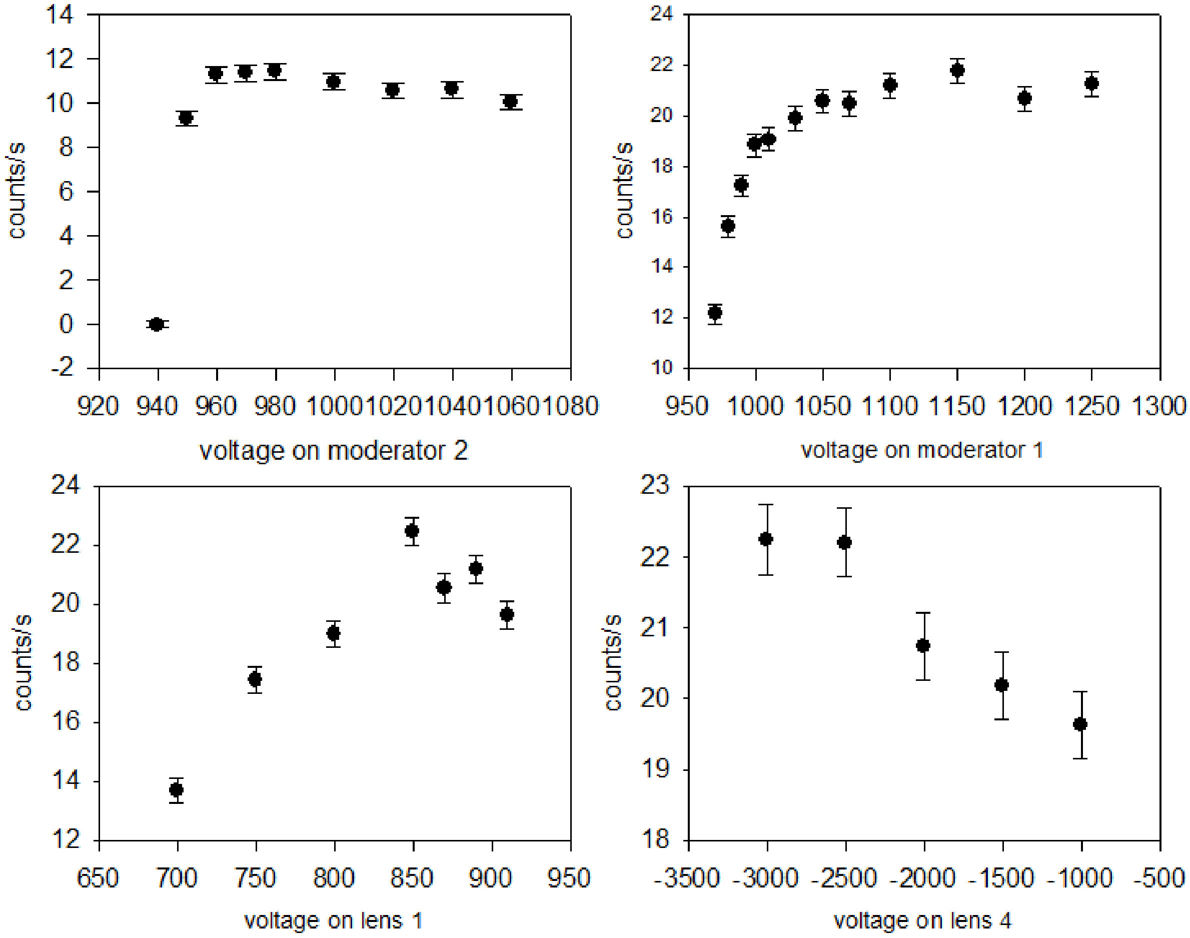

Fig. 3.5. Examples of typical data collected during the benchtop testing of the positron beam.

A potential of +960 V was applied to the extraction grid and the potential placed on moderator 2, the bank closest to the extraction grid, was varied to determine the optimum voltage. The maximum count rate of approximately 12 slow e$^+$/sec, occurred when the moderator was held at a +20V relative to the extraction grid. Once this optimum was determined, a potential of +980V was placed on moderator 2 and the voltage of moderator 1 was varied. The count rate increased to approximately 21 slow e^+/sec when this moderator was at a potential of +100V, relative to the extraction grid. Once the maximum count rate was achieved, further optimizations were performed on the voltages applied to the extraction optics. [42]

Following the optimization of the positron beam with the source located at the side of the moderator banks, the source location was moved to the center of the outside of the vacuum chamber behind the moderators. This was due to the previous test favoring the production of slow positrons near the edge of the moderators were extraction efficiency was lowest. Moving the source to the rear of the beam better estimates the geometry of the positron beam in the beam tube 6. The same optimization procedure was again performed resulting in an intensity, including the detector efficiency, of 6.81 ± 0.18 $s^{-1}mCi^{-1}$. [42]

Because the intensity should scale linearly with the photon flux, the measured positron rate is assumed to be equal to the product of the source flux, pair production cross section and a constant which encompasses the moderator conversion efficiency and efficiency of the extraction optics and magnetic transport,

$$N\left(e^{+}/s\right)=a\varphi\sigma$$

where N is the intensity, φ is the flux, σ is the cross section and a is the constant. This constant is determined to be $9.59\text{x}10^{19}$. MCNP was used to determine the photon flux greater than the pair production threshold through the moderators within beam tube 6 of the PULSTAR reactor. The scaled rate can then be calculated as:

$$R = a\sum_{i} \varphi_i(E)\sigma_i(E)$$

where R is the scaled rate, $\varphi_i(E)$ is the flux of an energy group and $\sigma_i(E)$ is the pair production cross section for an energy group. This calculation yields a predicted in-core intensity of $5.2\text{x}10^8$ s^{-1}.

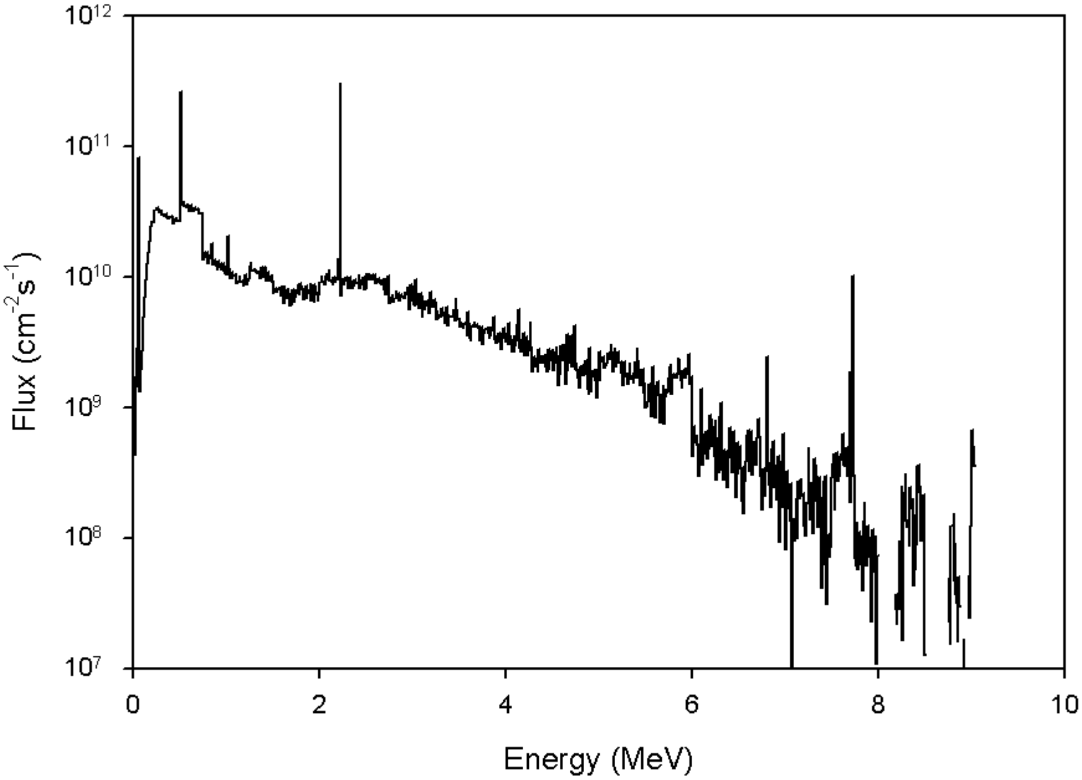

Fig. 3.6. MCNP calculated photon spectrum of the PULSTAR Reactor in the region of positron moderator.

3.2 Insertion of the Intense Slow Positron Beam into Beam Tube 6

Once out-of-core testing was complete, the beam was disassembled and cleaned for final assembly. For out-of-core tests, a temporary drift tube was used, which was replaced for the final assembly of the beam. Once reassembly of the extraction optics was complete, the solenoid and extraction optics were moved into the reactor bay along with the pumping station. Once in the reactor bay, the solenoid was reattached to the pumping station and the integrity of the high-voltage connections were tested. Out-of-core tests were once again performed to ensure the positron beam was still functioning properly after the move. Unfortunately, testing indicated the production rate decreased dramatically from the initial out-of-core testing. This was attributed to the time the moderators were out of high vacuum while the positron beam was being prepped for insertion into beam tube 6 of the PULSTAR reactor. The moderators were again annealed at Oak Ridge National Laboratory. This refreshed the moderators and brought the production performance back to the expected values.

Finally the positron beam was ready to be taken into the shielding cave for insertion into the beam tube. Once inside the cave, the pumping station was removed from its stand and placed on the cart already in place. The opposite end of the beam was then attached to the cradle by bolting the cradle to the vacuum chamber housing the extraction optics. Because the solenoid of the positron beam was substantially smaller than the cross-section of beam tube 6, internal neutron shielding was installed around the positron beam and cradle. This shielding was composed of 1” thick borated polyethylene sheets. Beam tube 6 possesses three tiers of decreasing cross section. The first twelve sheets where designed to rest within the smallest tier, having a cross-section of approximately 11.5”x11.5”. Because the sheets rested on the tier, these shielding blocks supported the reactor end of the positron beam. This was followed by ten layers with a cross-section of approximately 13”x13” and finally five layers with a cross-section of approximately 18”x18”. This neutron shielding was followed by eight 1” thick lead layers with a cross-section of approximately 18”x18” for gamma attenuation.

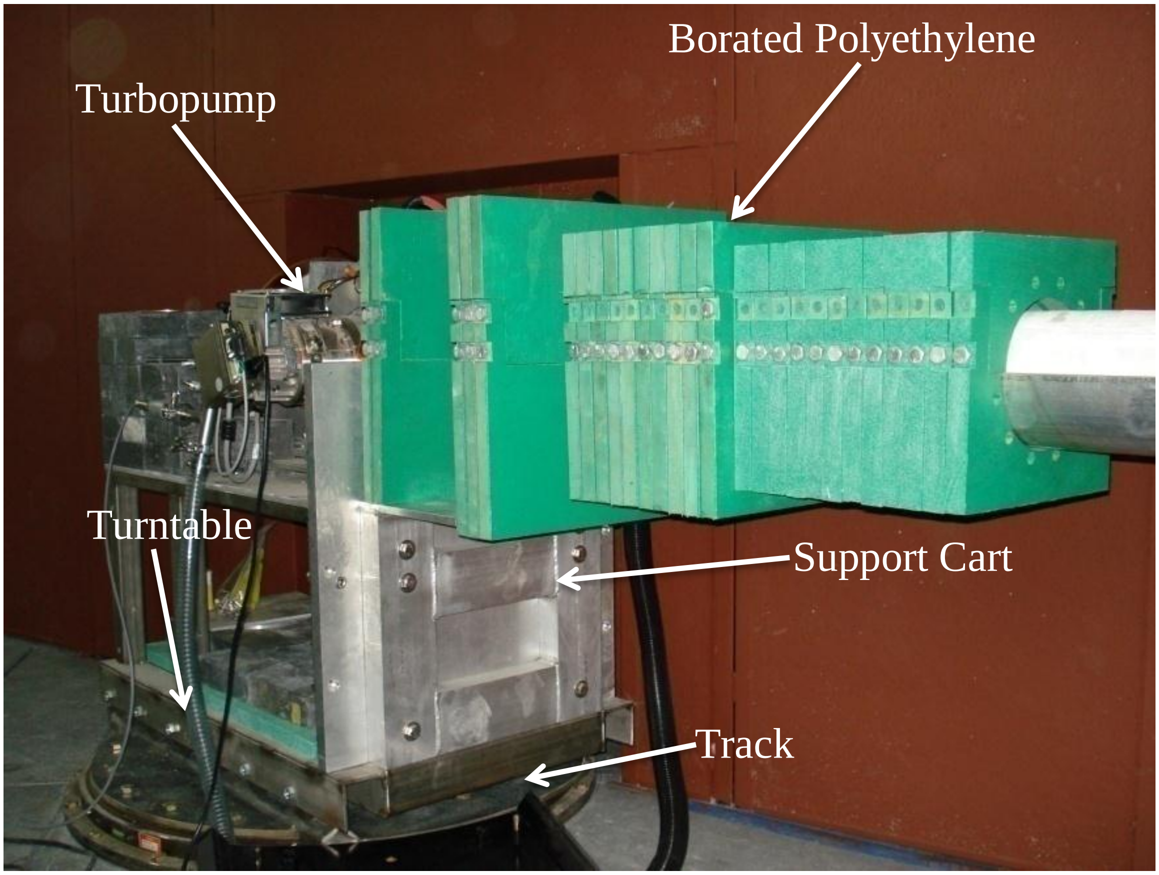

Fig. 3.7. Image of the positron beam installed on its cart with the borated polyethylene shielding.

Therefore 27” of borated polyethylene and 8” of lead were used to effectively reduce the neutron headlight for the full face of the reactor core to a diameter of approximately 6”.

Once the positron beam was installed on the cart, the cart could be rotated to be in line with the beam tube. The opposite end of the positron beam was supported by a hoist to help support the beam line during the insertion. The vacuum chamber of the positron beam was first slid into beam tube 6 until it cleared the smallest tier. Once the beam was safely within the smallest cross-section portion of the beam, some of the 11.5”x11.5” shielding blocks were installed which supported the beam within the biological shield, then the positron beam and the remaining shielding blocks could safely be slid into place within the biological shield.

Fig. 3.8. Images of insertion of the slow positron beam into beam tube 6.

An enclosure of borated polyethylene was constructed to shield the outlet of the biological shield of the PULSTAR reactor. This enclosure consisted of blocks constructed from 1” sheets of borated polyethylene. The left side of the enclosure consisted of eight sheets, with a cross-section of 48”x48”, assembled simply using threaded rods.

Fig. 3.9. Images of the Second Generation Intense Slow Positron Beam installed in beam tube 6 of the PULSTAR reactor.

The right side of the enclosure formed an angle with the neutron imaging shielding; therefore the first sheet was 48”x48” with the remaining sheets decreasing in length to fill in the gap between the positron beam and the shielding cave. To act as a beam stop, 8” of lead was stacked on the cart, followed by an enclosure wall which consisted of 8” of borated polyethylene that interlocked with the two side walls. The top of the enclosure was again fabricated from borated polyethylene, which was split in half so the entire roof would not have to be removed if access to the positron beam was required. Holes were placed in the roof of the enclosure to allow the passage of *S*-bend of the positron beam and the electronic connections.

The switchyard coils and vacuum chambers were designed to suspend from two aluminum plates mounted near the ceiling of the positron shielding cave. These plates provided tracks to limit the amount of travel the coils could achieve. The plates were bolted to aluminum bars spanning the width of the positron shielding cave. To reduce bowing of these bars, due to the weight of the switchyard, a few threaded rods mounted to the aluminum plate supporting the gimbals were attached to the roof of the cave. Once the plate was hung, the gimbals and coils holders were installed. The two coil holders which comprised the gimbal were mounted off a single threaded rod which passed through the plate. Once the coil holders were in place, the large diameter coils could be installed. First, the 31” OD coil was installed by balancing the coil on a hydraulic lift, so the weight of the coil was supported while being hung. Next, the smaller 23” OD coil could be installed. This coil could be rested on the larger coil then lifted into place for installation. Once the coils were in place, the vacuum chamber of the switchyard could be suspended within the coils from rods attached to the aluminum plate above. After the switchyard vacuum chambers were installed, the exact location of the core holes through the positron cave and lab walls could be determined. Three holes were bored through the shielding, two 12” holes allowed solenoids to penetrate the walls in the respective labs and one 4” hole allowed for electrical connections to pass from the lab to the equipment in the shielding cave.

Fig. 3.10. Image of the assembled coils used to magnetically guide positrons into the respective labs

Prior to the holes being bored, ultrasound images of the wall were taken to ensure the hole locations were free of obstructions, e.g. steel rebar. Once the penetration holes were cut, solenoids were installed in the respective switchyards. These holes are air tight so a negative pressure can be maintained in the reactor bay for confinement purposes. To achieve this, a circular aluminum plate was first mounted to the wall using anchors. A thin rubber sheet was wrapped around the solenoid and provided a buffer between the solenoid and an aluminum collar which then attached to the plate mounted to the wall. This served to support the end of the solenoid outside of the confinement wall.

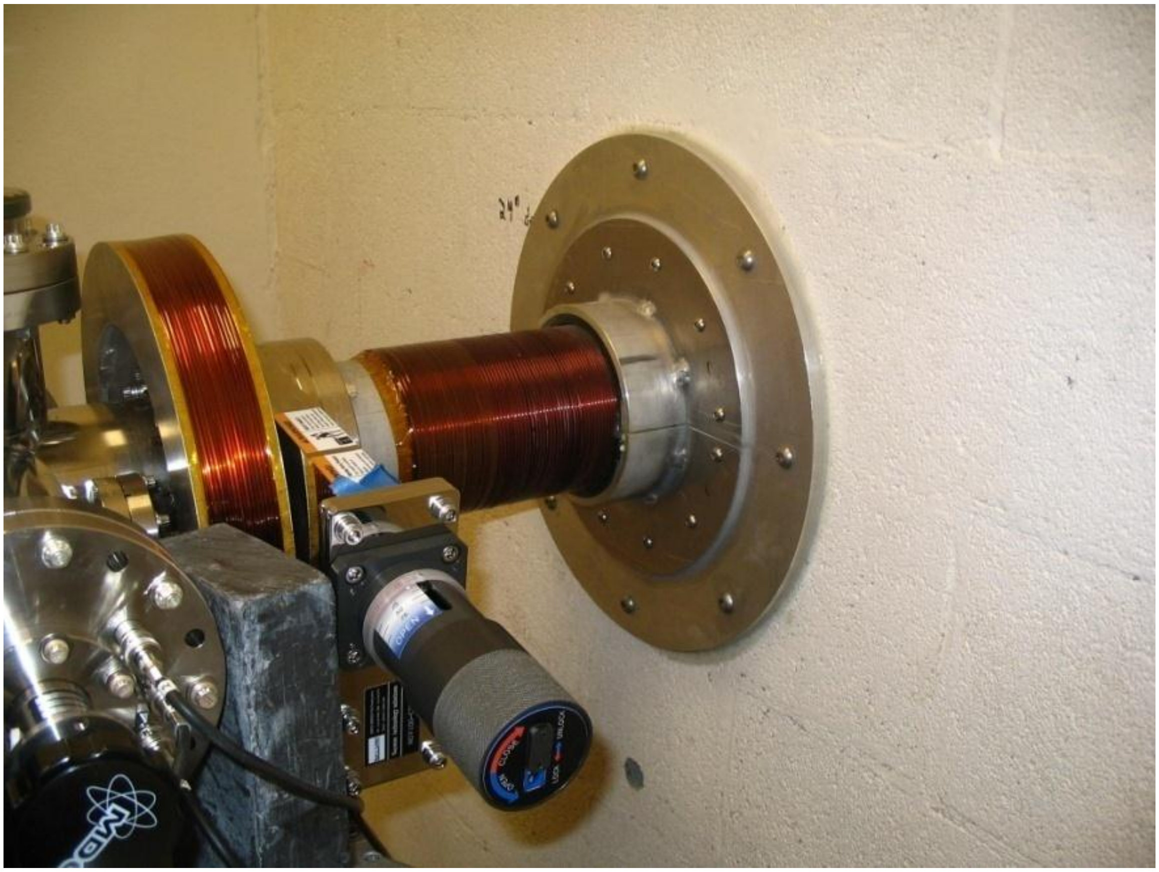

Fig. 3.11. Image of the solenoid penetrating the shielding walls into the e$^+$-PALS spectrometer lab with the accompanying gate valve.

To provide an airtight seal, the seams between the aluminum plates, the wall and the solenoid were sealed with silicone caulk. The ends of these penetrating solenoids were sealed with Varian gate valves; therefore the main positron beam could be isolated from the spectrometers when not in use.

3.3 In-core Testing of the Intense Positron Beam

Once installed, testing the positron beam with photons produced by the PULSTAR reactor could begin. Low power tests were first performed to not only ensure the shielding cave offered sufficient protection to personnel in the reactor bay, but also in the event of a problem which required removal of the beam for repair, the induced activities would be minimized. At low power, the slow positron beam intensity was measured using a microchannel plate which was installed directly after the first bend of the *S*-bend. As with bench top testing, a measurement was performed using the optimized potentials from out-of-core testing followed by a measurement with the potential of the extraction grid higher than that of the moderators, which pushed slow positrons away from the extraction optics. These low power runs indicated that the positron beam was successfully converting gamma rays from the core into slow positrons and extracting them through the biological shield.

While measurements using the microchannel plate demonstrated the positron beam was functioning, as power levels increased, the beam intensity quickly reached a level where the microchannel plate detector did not work effectively. For higher power runs, a BaF_2 scintillation detector was utilized. To reduce the dead time experienced by the detector due to the detection of background radiation from the beam tube, the straight portion of the *S*-bend was installed, removing the detector from the radiation headlight of the beam tube. This also allowed the lid of the borated polyethylene shielding enclosure to be installed, further reducing the radiation field. The detector was also placed within an enclosure of lead bricks, which provided collimation. The BaF_2 detector was calibrated using a Na-22 source placed in the location of the annihilation target. An example of the 511 keV annihilation peak for the spectra with the positron beam on can be seen in fig. 3.12. The difference in the peak area with the beam “on” and “off”, paired with the detector calibration using the Na-22 source, indicated the intensity of the resulting slow positron beam.

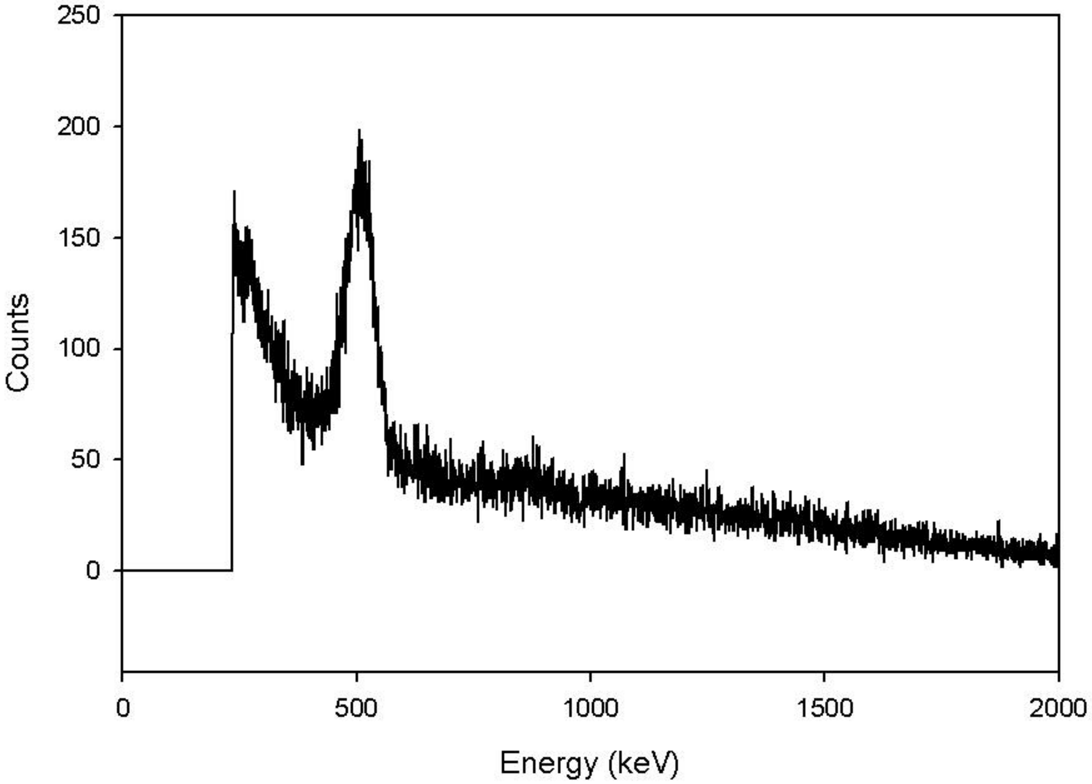

Fig. 3.12. Energy spectrum taken with BaF_2 scintillation detector while the positron beam was operating. The peak indicates the 511keV annihilation peak.

The reactor power was increased in 1 keV increments until power reached 10 kW. These tests were followed by 10 kW increments to 100 kW and 100 kW increments to 1 MW. This initial round of testing indicated the slow positron beam intensity scaled linearly with reactor power and surpassed $1x10^9$ s^{-1}, as seen in Fig. 3.13.

Unfortunately, after a short time of exposure, a problem with shorting between the moderators began to develop and a degradation of the vacuum was observed. The degradation of vacuum was attributed to the increased temperature due to the reactor power, but the positron beam was removed and unsealed to inspect and repair the internal components. The shorting issue was attributed to bowing in the grids behind the individual moderator banks, which contacted the adjacent moderators and lens components. This problem was alleviated with a modification of the grid holders to include thin supports that passed across the cross-section of the grid, which offered support to the large diameter grids and effectively prevented bowing.

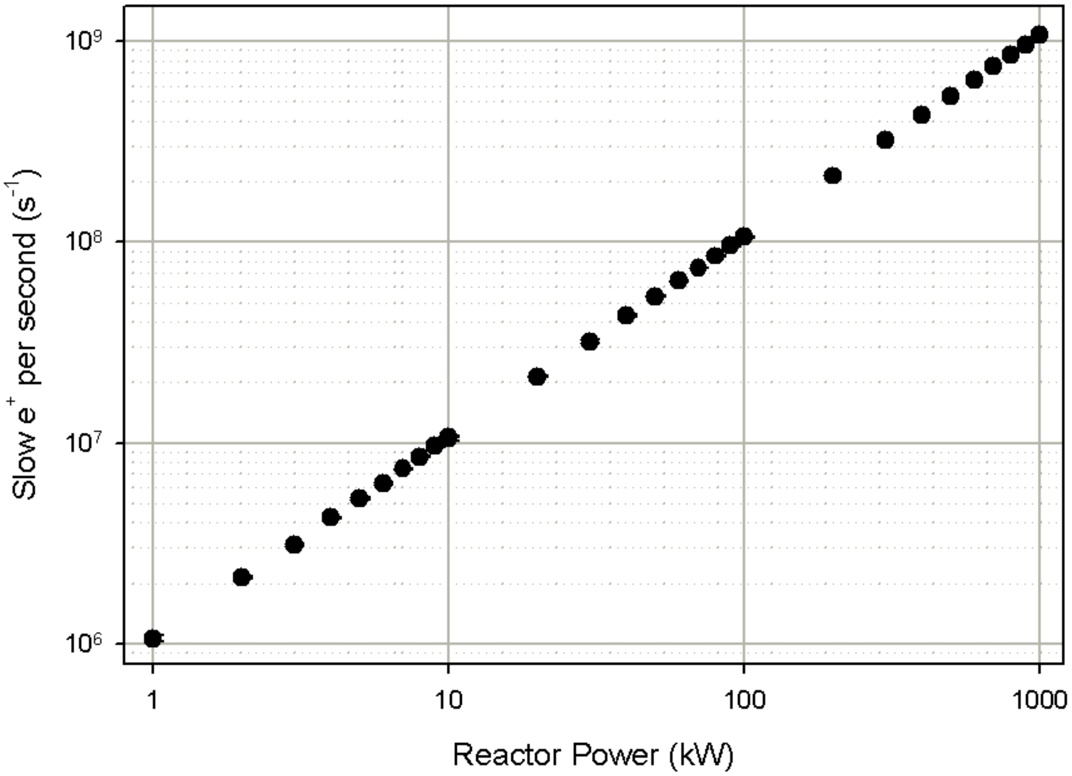

Fig. 3.13. Results demonstrating the linearity of the beam intensity to the reactor power.

Following the modification of the grid holders, the positron beam was reassembled and reinserted into beam tube 6. Testing indicated that after the positron beam was reinstalled, the repair of the tungsten grids and degradation of vacuum lead to the intensity of the beam stabilizing at approximately 6x10^8 s^{-1}. [51]

The loss in intensity was attributed to surface contamination due the degradation of the vacuum. This degradation was thought to be due to outgassing of the Viton o-ring used to seal the vacuum end cap to the solenoid vacuum chamber. A reactor based intense slow positron beam located at the FRM-II reactor in Munich also experienced a degradation of intensity during operation which was attributed to surface contamination of the platinum moderator foils used to produce positrons. Measurements indicated a loss of intensity with time constants of 5 minutes and 1 hour, with saturation occurring at 18 hours. With the introduction of 1 mbar of oxygen to the system for 150 s, the FRM-II positron beam rate was increased by approximately 90%. [71]

An RGA, residual gas analyzer, was used to measure the composition of the residual gas within the vacuum chamber. As the power increases, the pressure increases due to outgassing caused by the increase in temperature.

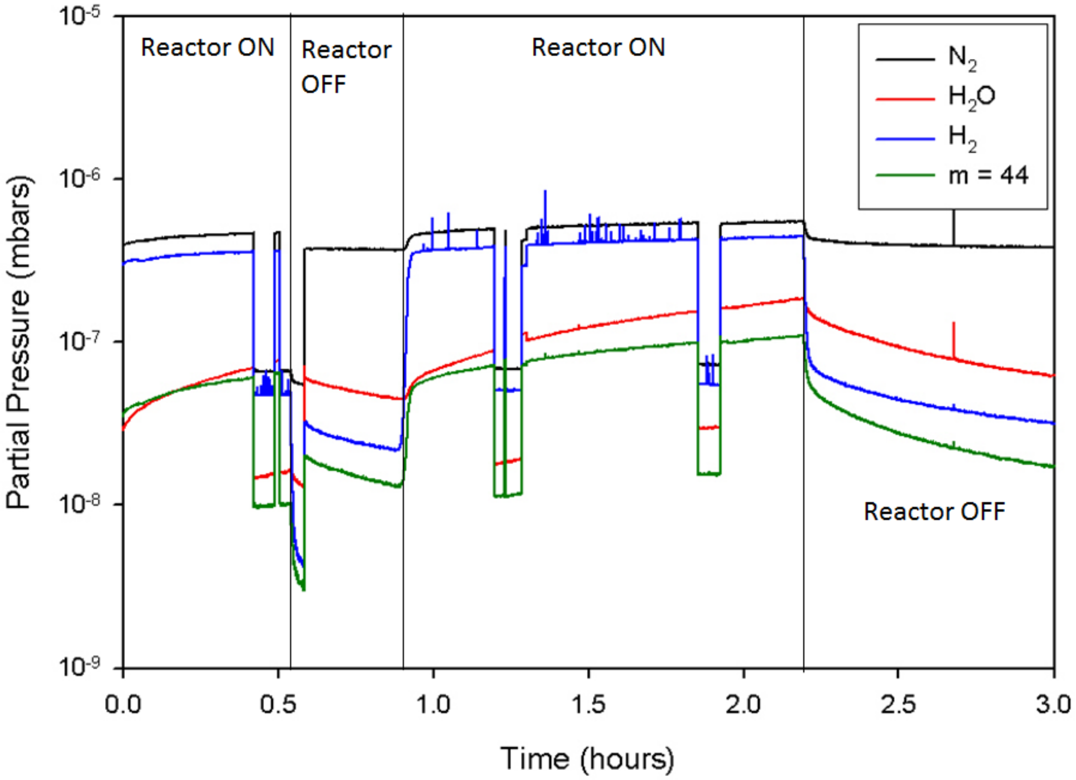

Fig. 3.14. RGA measurement of the partial pressures of the residual gas versus time with changes in reactor power.

The water arises from outgassing from the surface. The presence of nitrogen indicates the presence of oxygen which can possibly react with the surface

Measurements were performed on the moderator banks to determine the composition of the contamination. These XPS, x-ray photoelectron spectroscopy, measurements indicate the presence of a WO_3 layer which was not present prior to insertion of the tungsten moderator bank. A measurement of a piece of annealed tungsten which had not been inserted into the reactor, but was kept at atmospheric pressure, did not show this WO_3 layer. Therefore, the WO_3 layer was attributed to the degradation of vacuum in the elevated temperature and radiation environment in the vicinity of the reactor core.

The Viton o-ring originally used was eventually replaced with an aluminum c-ring seal manufactured by High Tech Metal Seals. Also, in order to minimize the pressure of the beam prior into insertion, after the new seal was installed, the vacuum chamber was heated with resistive heater tape and the solenoid was powered on to allow the vacuum chamber to outgas prior to insertion of the beam into the reactor. The temperature was maintained at approximately 140°F for one week. This allowed the vacuum chamber to outgas prior to insertion to obtain better vacuum.

Chapter 4 The Pulsed Positron Beam

By moderating fast positrons generated by a primary source, slow positron beams have been developed which allow for depth profiling of a sample, therefore demonstrating the evolution of the defect structure spatially. [7] This technique is based on the careful measurement of the positrons lifetime in a material, which is inversely proportional to the local electron density at the site of the annihilation. [4] While the detection of the 511 keV annihilation gamma-ray is a simple way to determine the end point of the positron's lifetime, a method to accurately determine a starting point for the lifetime is necessary to perform a PALS measurement.

As mentioned in the introduction, there is no prompt gamma to signal the birth of a positron in a beam generated by pair production. One successful technique used to generate the required timing signal for a PALS spectrometer involves "time-tagging" the positrons by generating equally spaced, in time, pulses of positrons. [6] In this case, the start signal is taken directly from the electronics used to generate the positron pulses, which is correlated to the time the positrons reach the sample.

The lifetime of positrons in metals and semiconductors is on the order of 100's of ps [32], therefore the spectrometer must have a time resolution on the less than 300 ps to discern these short lifetime events from the prompt peak due to pick-off annihilation. The time resolution of the spectrometer is taken as the quadrature sum of the detector resolution and the pulse width. The detector time resolution is limited to the properties of the detector, i.e. the rise time of the scintillator, the collection time of the photoelectrons, etc.; therefore it is set by the utilized detector. With the utilization of rf bunching techniques, the pulse width of the spectrometer can be controlled with optimization of rf fields applied to internal lenses. The time resolution of the electronics driving the rf fields is negligible, on the order of ps's, compared to the time resolution of the detector. Compression of the positron pulses, in time, decreases the deviation of the positron's arrival time from the signal generated by the pulsing electronics, increasing the overall time resolution of the spectrometer.

A spectrometer has been designed and built using the principles of longitudinal beam bunching paired with rf bunching techniques. The spectrometer was designed with the intent to produce the smallest pulse widths achievable to generate a spectrometer with a time resolution on the order of 250 ps, which requires a pulse width on the order of 150 ps, so measurements on metals and semiconductors can be performed. The ability to bias the sample was also included to allow control of the positrons kinetic energy, granting the ability to depth profile the sample.

Longitudinal beam bunching techniques, developed for bunching electrons and heavy ions, has proven to be successful for generating pulses of positrons with good time resolution. This technique involves the longitudinal compression of a steady-state beam in periodic pulses via velocity modulation using periodic electric fields. [33] The application of an rf potential to a particular lens produces high frequency electric fields between a lens with an oscillating voltage and lenses with a static bias. Upon reaching the acceleration gaps, positrons that lead the bunch are decelerated while positrons that lag the bunch are accelerated, producing bunches with a narrow time spread at the focal point due to the velocity modulation introduced by the acceleration gap.

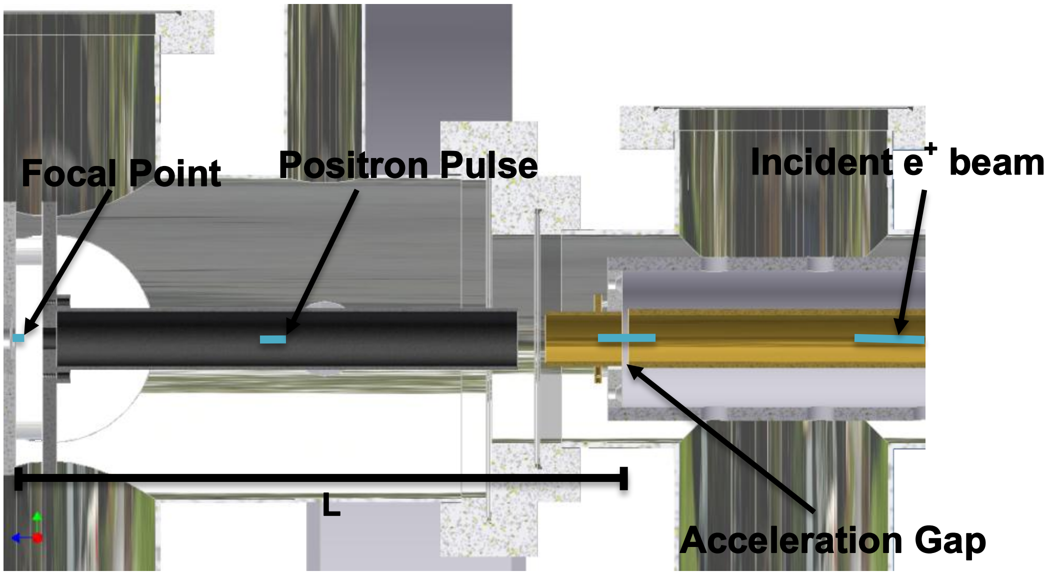

Fig. 4.1. Schematic of the bunching process using a single velocity modulation. The incident positron beam traverses an acceleration gap where it obtains a velocity modulation. The velocity modulation causes the positrons to cross at the focal point.

The parameters for the time focusing can be determined by considering conservation of charge. The amount of charge that passes any point of the beamline would equal the product of the beam current and the time interval at that point. Because of conservation of charge, it is assumed all particles passing an upstream observation point must pass a downstream point, so:

$$I_o dt = I(t) dt' \tag{4.1}$$

or

$$I(t) = \frac{I_o}{\left(\frac{dt'}{dt}\right)} \tag{4.2}$$

where I_o is the incident beam intensity, $I(t)$ is the instantaneous intensity at the focal point of the modulation, and dt and dt' are the time interval of the observation. Therefore, to determine $I(t)$, a relationship between t' and t must be determined. The time at the focal point would equal the sum of the time at the acceleration gap and the time of the particle drift.

$$t' = t + t_d \tag{4.3}$$

where the particle drift time would equal:

$$t_d = \frac{L}{v(t)} \tag{4.4}$$

In the previous equation, *L* is the focal length of the acceleration gap and *v(t)* is the modulated velocity. The modulated velocity is found from conservation of energy at the bunching gap. The total energy of the particle is equal to the sum of the initial kinetic energy of the particle and the modulated kinetic energy.

$$E(t) = E_K + E_m \tag{4.5}$$

where E_K and E_m are the initial and modulated kinetic energy of the particle. Therefore, considering classical kinematics:

$$\frac{1}{2}mv(t)^2 = \frac{1}{2}mv_K^2 + eV(t) \tag{4.6}$$

$$\frac{1}{2}mv(t)^2 = \frac{1}{2}mv_K^2\left(1 + \frac{eV(t)}{\frac{1}{2}mv_K^2}\right) \tag{4.7}$$

$$v(t) = v_K\sqrt{1 + \frac{eV(t)}{E_K}} \tag{4.8}$$

where *V(t)* is the modulation voltage and E_K is the kinetic energy, therefore:

$$t' = t + \frac{L}{v_K}\left(1 + \frac{eV(t)}{E_K}\right)^{-1/2} \tag{4.9}$$

Under the assumption and $E_K \gg eV(t)$, the relationship for the time to the focal point reduces to:

$$t' \cong t + \frac{L}{v_K}\left(1 - \frac{eV(t)}{2E_K}\right) \tag{4.10}$$

The derivative of this expression with respect to *t* is:

$$\frac{dt'}{dt} = 1 - \frac{L}{v_K}\frac{e}{2E_K}\frac{dV(t)}{dt} \tag{4.11}$$

therefore:

$$I(t) = \frac{I_o}{1 - \dfrac{eL}{2v_K E_K}\dfrac{dV(t)}{dt}} \tag{4.12}$$

For ideal bunching, the denominator of this expression must equal zero. This is due to the fact that as *dt'/dt* approaches zero, *I(t)* approaches infinity, signifying infinite intensity, i.e. ideal bunching, so, [33]

$$\frac{dt'}{dt} = 1 - \frac{eL}{2v_K E_K}\frac{dV(t)}{dt} = 0 \tag{4.13}$$

This equation provides the relationship between the design parameters of beam energy and focal length relative to a supplied voltage waveform.

4.1 Design Optimization Calculations

A double-gap buncher, similar to what was used at the pulsed positron beam located at FRM-II [55], was used to bunch the slow positrons from the primary beam. A high frequency time-varying potential in the form of a sine wave is applied to a suitable bunching electrode generating acceleration gaps at the ends.

$$V(t) = V_o \sin(\omega t) \tag{4.14}$$

Because ideal bunching only occurs near the zero crossing of the waveform, i.e. where the sine wave is most linear, the bunching waveform can be approximated as:

$$V(t) \approx V_o \omega t \tag{4.15}$$

where V_o is the amplitude of the applied waveform and ω is the angular frequency. The derivative with respect to time is constant:

$$\frac{dV(t)}{dt} = V_o \omega \tag{4.16}$$

Inserting this derivative into Eq.4.13**,** the relationship between the focal length and kinetic energy can be determined.

$$L = \frac{2v_o E_K}{e\omega V_o} \tag{4.17}$$

By considering classical kinetic energy, Eq.4.17 can be reduced to remove the velocity term.

$$L = \frac{\sqrt{\frac{8E_K}{m}} E_K}{e\omega V_o} = \frac{\sqrt{\frac{8}{m}} E_K^{3/2}}{e\omega V_o} \tag{4.18}$$

Because the energy can be taken as the product of the electric charge and the potential, $E=eV$, the relationship between the applied potential and focal length can be determined.

$$V_K^{3/2} = \frac{\omega V_o L}{\sqrt{\frac{8e}{m}}} \tag{4.19}$$

The optimum length of the bunching electrode can be determined using the definition of classical kinetic energy.

$$E_K = \frac{1}{2} m v^2 = \frac{1}{2} m \left(\frac{L_{buncher}}{\frac{1}{2} f_{buncher}} \right)^2 \tag{4.20}$$

By assuming the time it takes slow positrons to traverse the bunching electrode, i.e. the time it takes the slow positrons to reach the second acceleration gap from the first, is equal to half the period of the rf field, slow positrons must traverse the acceleration gaps in phase with the applied waveform. A bunching electrode length of 7” requires the incident positrons to be accelerated to approximately 900 eV. Because of the short distance separating the two acceleration gaps, the total energy modulation will be the sum of the acceleration gap potentials [33], therefore the focal length is taken to span from the center of the bunching electrode to the target. Taking the length between the center of the bunching electrode and the target as 35.6 cm and assuming a beam energy of 900 eV, the amplitude of the applied sine wave must be 143 V, or the waveform must have a peak-to-peak voltage of 286 $V_{p\text{-}p}$.

The effectiveness of the double-gap buncher design was tested using a user program created for SIMION. The model utilized can be seen in fig. 4.2.

Fig. 4.2. Image of the geometry supplied to SIMION to simulate the pulsed positron beam.

The program launches a particle every 10 ps in the axial direction. Each particle is given an energy sampled from a 0.4 eV Gaussian distribution centered at 2.8 eV to mimic the energy spread of positrons emitted from a transmission remoderator foil [55]. The results of the simulation indicate the buncher design is capable of bunching positrons with an initial assumed energy spread of 0.4 eV to a time focus of 120 ps.

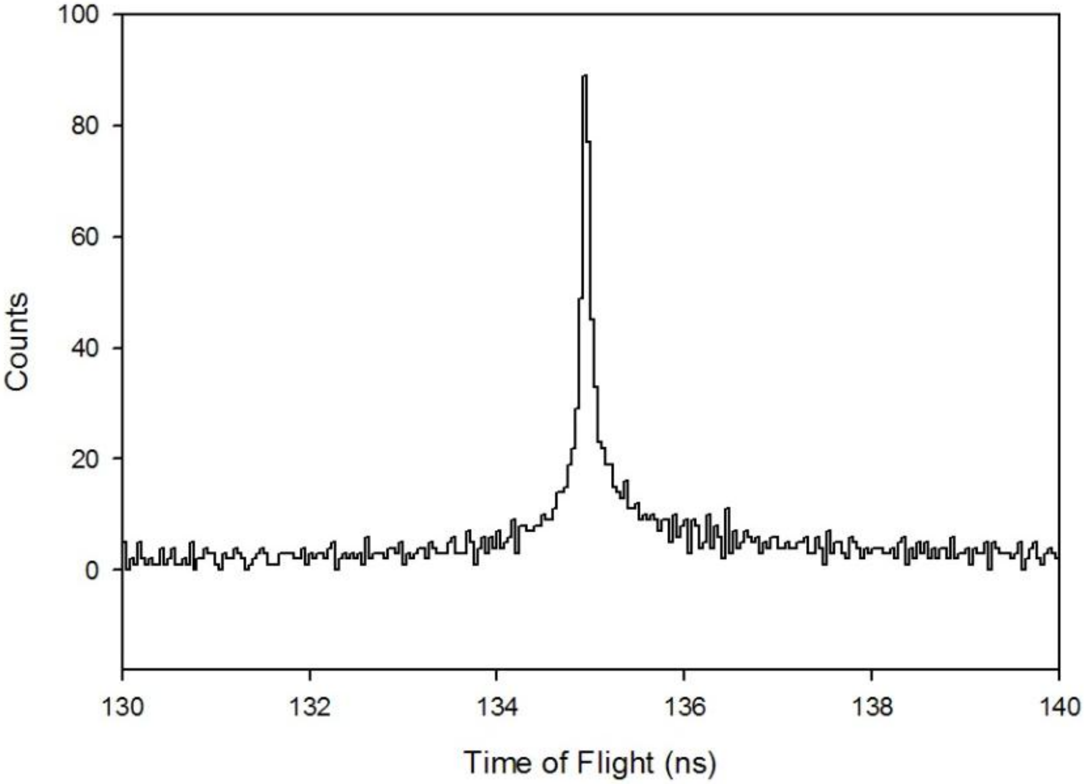

Fig. 4.3. Results of a SIMION3D simulation displaying the time focus at the target with emitted particles given an initial energy spread of 0.4 eV.

The bunching cavity is designed to act as a 50 Ω coaxial transmission line. A coaxial transmission line comprises two concentric cylinders separated by an insulating material. Electromagnetic waves propagate down the transmission line with a velocity which is dependent on the permeability and permittivity of the medium. [56] Because the gap separating the inner and outer conductors is a vacuum, the propagation velocity can be taken as the speed of light. Since the length of the electrode is designed to be 7”, 17.78 cm, it would take the rf wave approximately 593 ps to traverse the lens, meaning if the voltage was applied to the end of the electrode, the entrance and exit acceleration gap would be out of phase by approximately 11°. To compensate, if the rf potential is applied to the center of the electrode, the wave propagates to both ends with equal velocity. Meaning the voltages across the two acceleration gaps must be in phase with one another.

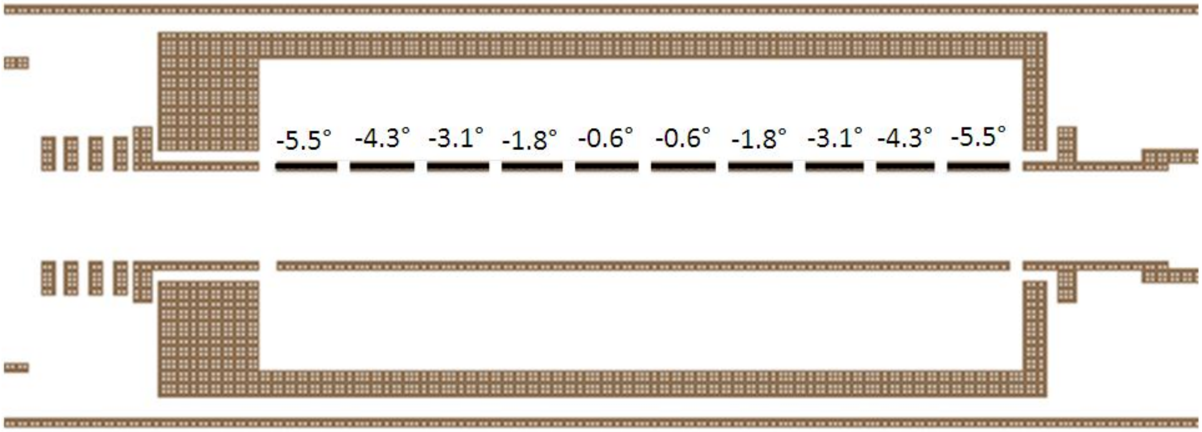

Fig. 4.4. Close-up image of the geometry defining the buncher used in the SIMION simulation. The electrode is broken into segments and a phase shift is applied to each to mimic the effect of an electromagnetic wave propagating down the surface.

To account for this effect in the simulation, the bunching electrode was broken into 10 segments, as seen in fig. 4.4, where each segment had an applied sine wave with a phase shift. The center of the bunching electrode would be 5.5° out of phase with the ends, so this total phase shift is split among the segments accordingly. Positrons were again emitted every 10 ps, without an initial energy distribution, in the axial direction. Multiple simulations were performed to see the effect of changing the drift potential on the time focus. The results of this optimization can be seen in fig. 4.5. When including the effects of the propagation velocity on the potential applied to the buncher, the new optimum drift potential is -800V relative to the potential applied to the simulated remoderating foil.

The pulse deviates from ideal due to a number of factors. If ideal bunching was achievable, the pulse width would be limited by the initial energy spread of the incident particles. A deviation of the energy of the positrons would lead to a spread in the ideal pulse width. Remoderating the primary positron beam decreases the longitudinal spread of the positrons acquired during focusing, giving the positrons a small energy spread about the work function of the moderator, but factors can lead to further energy spread. Non-homogeneous fields within the spectrometer can act on the positrons introducing an increased deviation in the longitudinal field. These fields can arise from fringing fields between adjacent lenses. Also, if rf fields applied to the bunching electrode are picked up by the lenses of the spectrometer, a low magnitude fluctuation on the bias applied to these lenses can arise. This would again provide an energy modulation to the positrons traversing the spectrometer.

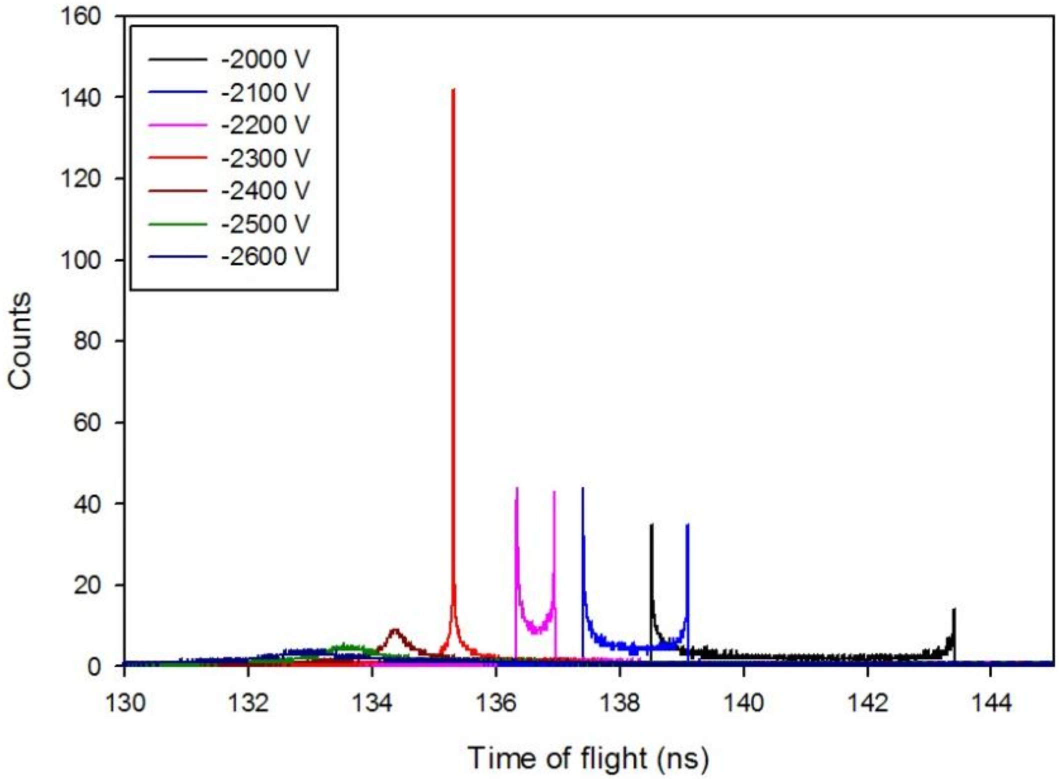

Fig. 4.5. Calculated time resolution at the sample position of the pulsed positron spectrometer while varying the drift potential to the target.

One factor causing a spread in the pulse width is a deviation of the pulse from ideal. Only a small portion of the applied sine wave is capable of mimicking the ideal waveform. Positrons arriving away from this ideal portion receive a slightly different potential from the ideal. This would increase the energy spread of the pulse leading to a wider pulse width.

The spot size of the beam can also lead to deviations in the pulse width. The fringing fields at the entrance and exit of the bunching electrode cause deviations in the magnitude and shape of the electric field at positions off the axis of the beam. This leads to deviations in the transit time of the positrons through the acceleration gaps, meaning the positrons would not acquire the ideal kinetic energy for bunching.

4.2 Beam Design and Construction

A diagram of the pulsed positron beam can be seen below and consists of 6 main components: magnetic coils for an axial field, magnetic steering coils, a moderator chamber, a drift chamber, a bunching chamber and a target chamber. The positrons are transported to the target using a combination of bridging coils and a solenoid. Two small coils bridge the moderator chamber and direct the positrons into a solenoid. The position of the small coils can be altered to fine tune the axial magnetic field. The solenoid transports the positrons to a set of large bridging coils, placed on gimbals for fine tuning of the field. To reduce the background created by positron annihilation within the transmission remoderator, the positrons are steered around an internal lead shield using an array of coils which supply transverse fields.

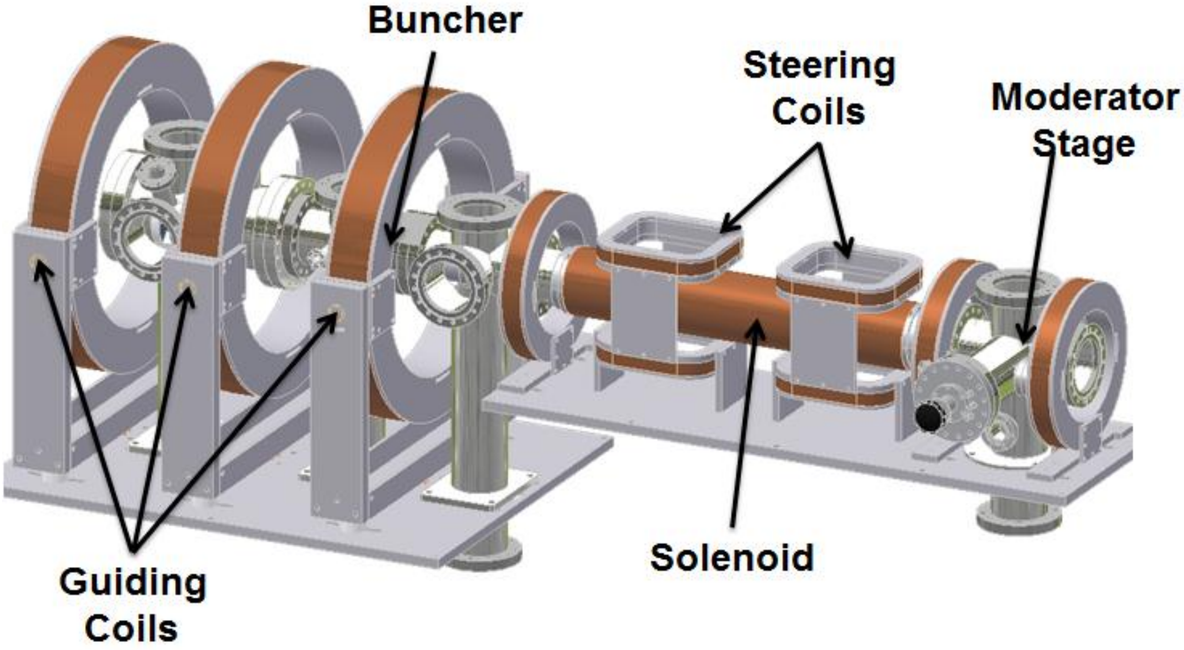

Fig. 4.6. Diagram of the pulsed positron spectrometer. This figure displays the placement of the magnets used to guide the remoderated slow positron beam.

4.2.1 Magnetic Guidance System

Positrons are magnetically guided through the e^+-PALS spectrometer from the moderator to the target. Two small 6" radius coils, with a 4.25" inner radius and a width of 1.5", were used to bridge the moderator chamber. The coils are mounted to small holders containing three standoffs. By varying the length of the standoffs, the vertical angle of the coil could be modified. Also, the holders are installed in small tracks to allow the horizontal angle to be fine-tuned. This ensures the positrons are efficiently guided through the moderator stage. After traversing the moderator chamber, the positrons are guided through a four layer solenoid. This provides a steady axial field for the guidance of the positrons while minimizing the amount of individual coils required. An additional coil, identical to the coils used to bridge the moderator chamber, is used at the outlet of the solenoid to aid in bridging the field between the solenoid and large coils which follow. Because of the placement of the vacuum chamber supports, three large coils are used to guide the positrons from the outlet of the solenoid to the target. These coils have a 3”x3” cross section to minimize the amount of current needed to produce a desired field and are separated by 11.75” to position them around the vacuum chamber supports. The coils are installed on gimbals to allow fine tuning of the axial field in the horizontal and vertical direction. The gimbals are mounted to the table using a single rod in the center of the gimbal, penetrating the table for stability. Teflon spacers are placed at the ends to support the gimbal and coil assembly while reducing the friction between the heavy coil and table surface to aid in positioning the coil.

The positrons are guided around an internal lead shield located in the solenoid to reduce background due to positron annihilation in the moderator. This guidance is achieved with two sets of transverse coils. These coils are rectangular with an inner cross section of 6.5”x7.5”. The coils are separated by 7.5” and are positioned so the solenoid passes through the center of the set. The coils are connected in series so each set receives identical current, but the current flows through each set in the opposite direction. This ensures one set of coils will push the positrons off axis and around the internal shield while the following set returns the positrons trajectory to the center of the beam.

The AMaze ion optics suite was used to test the effectiveness of this coil layout. An image of the coil definition file used in the simulation can be seen in fig. 4.7. Each individual coil is represented by a different color and consists of a reasonable estimation of the number of turns in the respective coil, except the four transverse coils, which are modeled as a single rectangular coil.

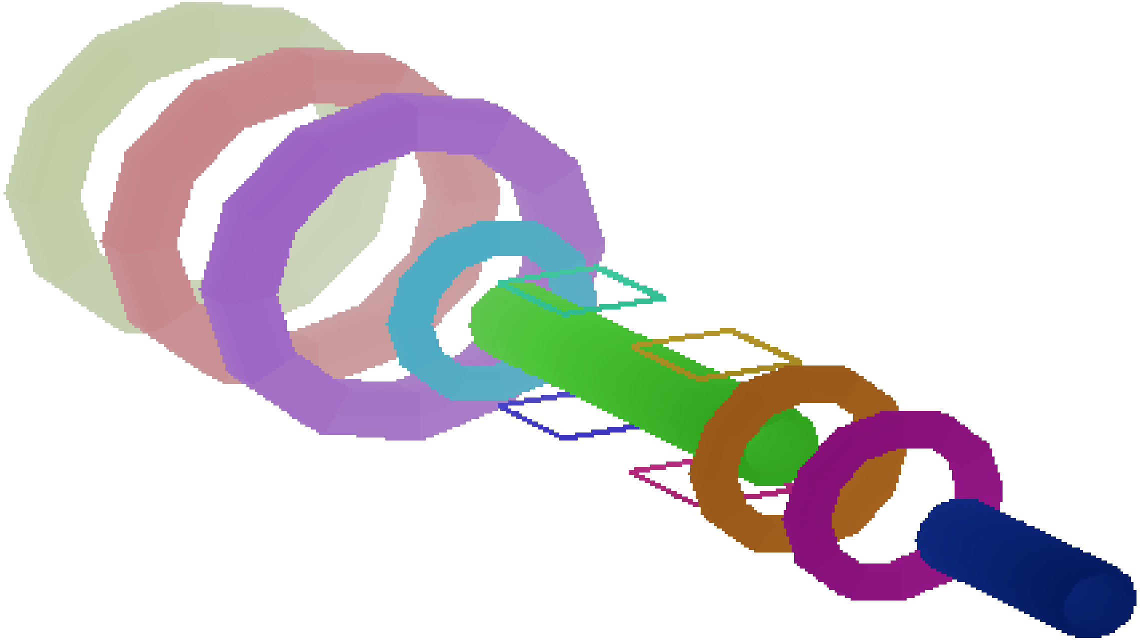

Fig. 4.7. The purposed coil layout for the slow positron spectrometer.

To test the effectiveness of the magnetic guidance, 9999 positrons were emitted randomly from a 1 cm diameter disk from a uniform angular distribution of +/- 5° and an initial energy of 2.8 eV. The final results of the simulation can be seen in fig. 4.8. The simulation demonstrates that the magnetic coil spacing should be capable of transporting positrons from the moderator to the target and the transverse coils should be able to successfully guide positrons around the internal shield, with 99.6% efficiency.

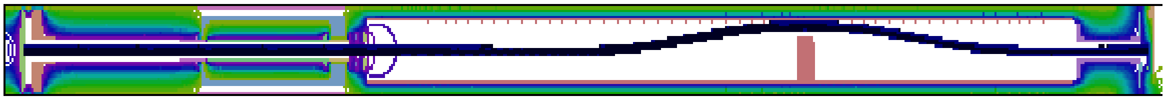

Fig. 4.8. Results of the magnetic guidance simulation of positrons from the moderator to the target.

4.2.2 The Vacuum System

The pressure of the spectrometer must be reduced to a point where the mean free path of the residual gas is on the order of the dimensions of the chamber. This ensures that the residual gas is more likely to interact with the walls of the spectrometers rather than with positrons traversing the chamber. Using the kinetic theory of gas the average distance between interactions can be estimated as:

$$\lambda = \frac{1}{\sqrt{2}\pi d_o^2 n} \qquad 4.21$$

where λ is the mean free path, d_o is the molecular diameter of the gas and n is the number density. This relationship arises by equating the volume swept out by a moving particle traversing chamber and the volume of a single molecule. For air at room temperature, an engineering equation to estimate the mean free path is [52]:

$$\lambda(cm) = \frac{0.67}{p} \qquad 4.22$$

where λ is the mean free path in mm and p is the pressure in Pa. Assuming the chamber is approximately 2 m long, therefore the distance traversed by the positrons is 2 m, the pressure of the chamber must be reduced to at least 2.5x10^{-5} torr to minimize the interaction of the positrons with the residual gas.

A Varian DS 102 mechanical pump is used to reduce the pressure of the spectrometer to less than 1 torr. At that point, a Varian 301 Navigator turbomolecular pump is used to quickly reduce the pressure to 1x10^{-5} torr. When the chamber is reduced to the 10^{-5} torr range, a Varian Diode ion pump is used to add additional pumping speed. After a night of pumping, the pressure of the chamber can be reduced to less than 5x10^{-8} torr.

4.2.3 The Moderator Stage

The moderator stage is suspended form a 6” to 2-3/4” zero-length-reducer conflat flange. Three SHV feedthroughs are welded into the flange to supply voltages to the internal components. The remoderator holder is attached directly to a direct rotary-linear manipulator, MDC part #: 672008, to allow the remoderator to be moved within the vacuum chamber.

The remoderator holder consists of a 2” OD disk composed of non-magnetic stainless steel. A Tungsten-Molybdenum (WMo) transmission remoderator foil is placed over a 0.45” diameter hole in the holder and is held in place with a corresponding stainless steel collar.

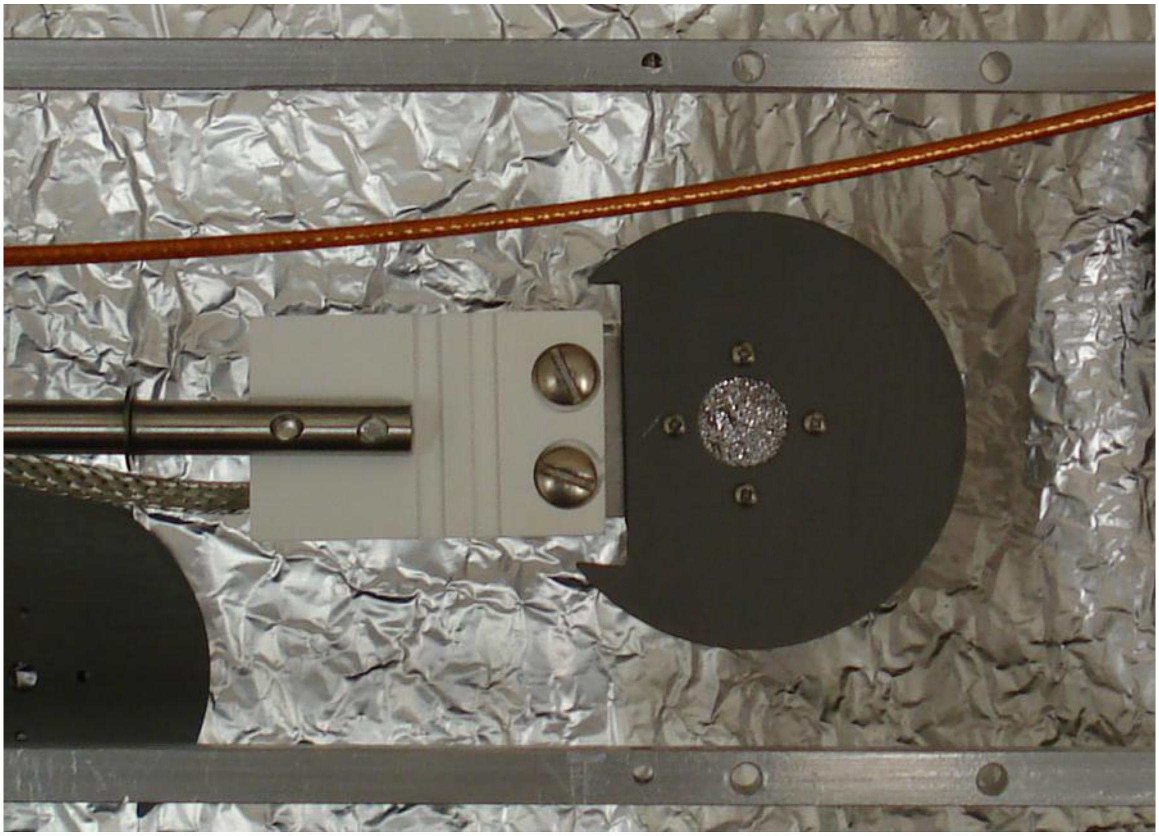

Fig. 4.9. Image of the moderator holder. Groves were milled into the boron nitride insulator to prevent arcing to ground when applying have voltage to the moderator for *in situ* annealing.

The remoderator is electrically isolated from the manipulator using a boron nitride ceramic block, with groves machined across the surface to minimize the possibility of arcing down the surface of the insulator. The lengths of the remoderator holder and insulator were chosen so the center of the remoderator is located on the axis of the beam when the manipulator is fully inserted into the vacuum chamber. The time-varying potential is applied to the moderator through a 50 Ω coaxial cable with the outer insulation removed. Each end of the outer conductor is grounded to minimize degradation of the applied waveform.

An aluminum bracket is installed directly in front of the manipulator to hold an aluminum grid support. This support holds a tungsten mesh which provides a constant bias in front of the remoderator. The application of the time-varying potential to the remoderator is used to chop the DC primary beam.

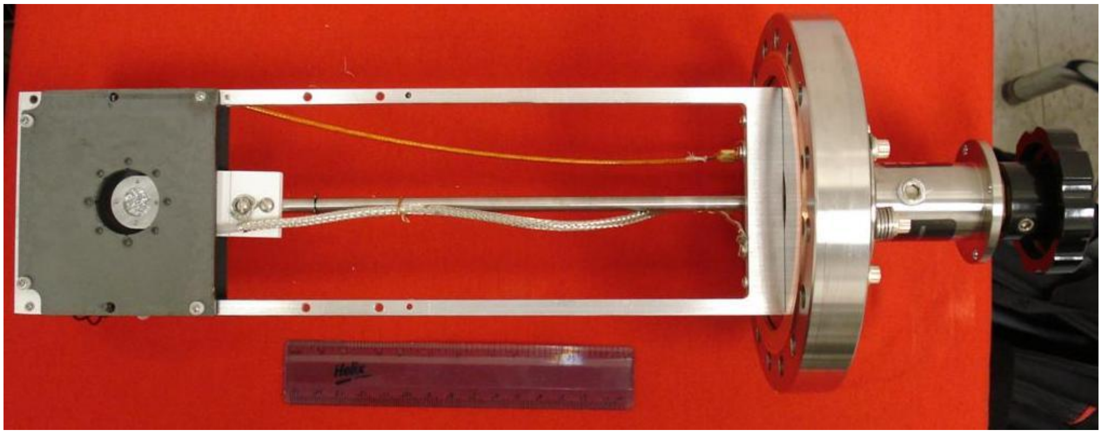

Fig. 4.10. Image of the assembled moderator stage.

The potential bias is supplied to this electrode using a 50 Ω coaxial cable with Kapton insulation. This electrode is grounded through a 1 nf capacitor, with a breakdown voltage of 3 kV, which acts as a DC block. Figure 4.10 and 4.11 demonstrate how the remoderator lies at the center of the beam line when the manipulator is fully inserted into the vacuum chamber.

A grounded aluminum plate is also placed directly behind the remoderator. This screens the primary positron beam from the electric fields due to the moderator and fringing fields from the extraction grid in front of the moderator in an attempt to minimize defocusing of the positron beam.

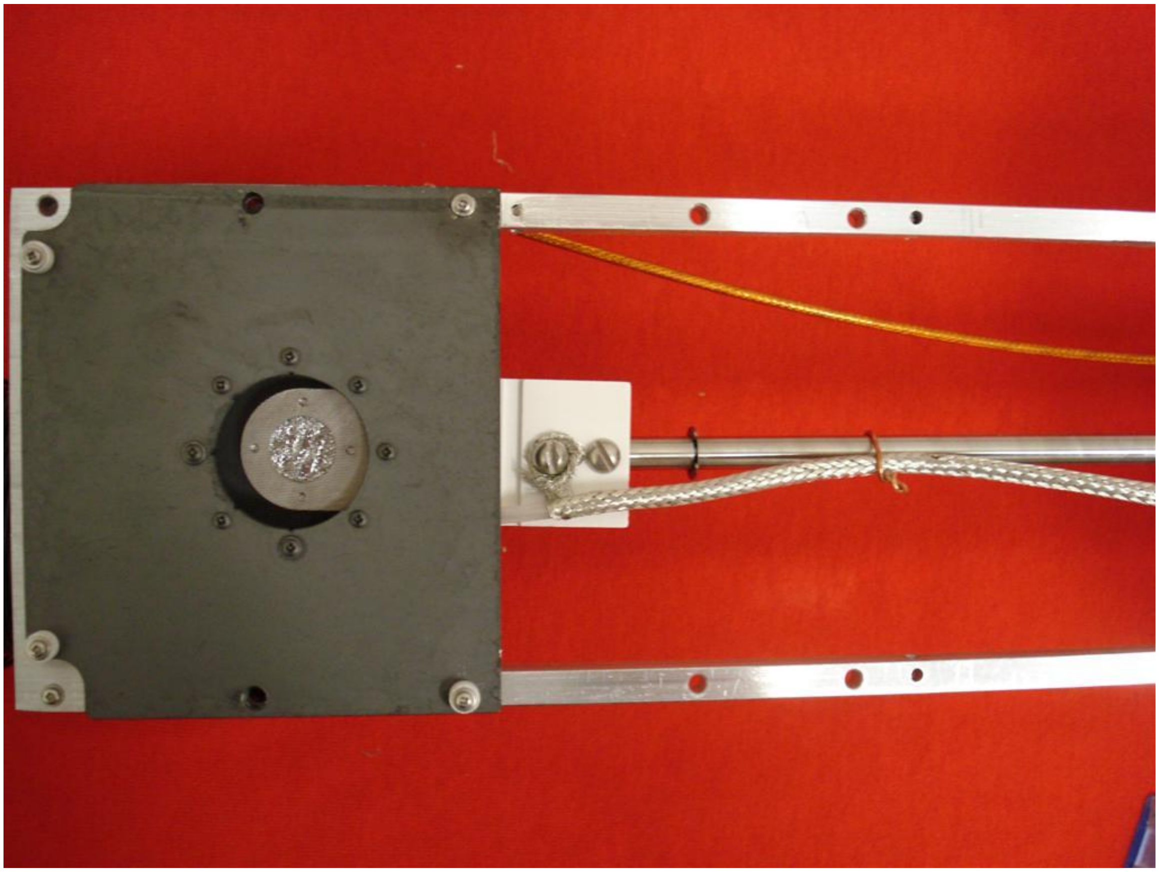

Fig. 4.11. Close up of the moderator in position behind the extraction grid. The tungsten foil lines up with the center of the beamline when the manipulator is fully inserted into the vacuum chamber.

The diameter of this aperture is approximately 10 mm. Because the primary beam diameter is 30 mm, a loss in beam intensity can be attributed to the primary beam traversing the aperture.

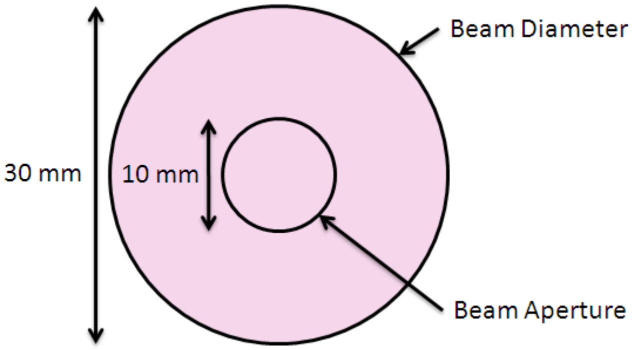

Fig. 4.12. Schematic of the beam diameter compared to the open aperture.

Assuming the primary beam is uniform in cross section, the loss in intensity can be estimated by taking the ratio of the aperture area to the beam cross sectional area. The ratio of the cross sectional area is simply the ratio of the square of the radii, resulting in an estimate of 11% of the primary beam is capable of successfully traversing the aperture to reach the moderator.

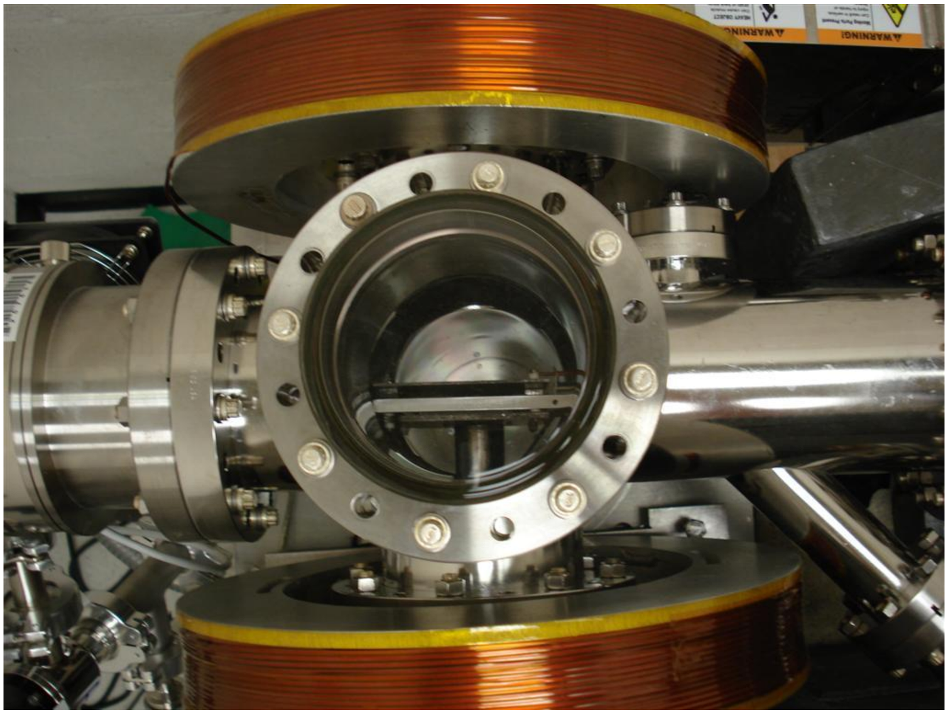

Fig. 4.13. Image of the chopper stage installed in the pulsed positron spectrometer. The viewport allows for checking of the position of the moderator.

A view port is placed on the top of the remoderator vacuum chamber to allow the inspection of internal components to ensure the remoderator is in the proper orientation for operation.

4.2.3.1 The WMo (Tungsten-Molybdenum) Transmission Remoderator

Typically, a 100 nm Tungsten (W) transmission foil is utilized to remoderate the primary positrons for the bunching process because of its large negative work function resulting in higher reemission efficiency. As mentioned in the introduction, moderating the primary positron source decreases the energy and angular spread of the positrons. For transmission moderators, the transmitted fraction of slow positrons is approximately equal to or less than the number of positrons emitted from the opposite side. The "reflected" positrons are effectively lost from the positron beam. [52]

A rectifying transmission moderator can be created by growing a moderator composed of two layers in contact. When W and Mo (Molybdenum) foils come into contact, the electron Fermi levels equalize at the interface via charge transfer. This charge transfer therefore introduces a dipole at the interface. The size of this step potential is determined by the difference of the chemical potential of the two metals. This dipole, combined with the differences between the positron chemical potential in the two metals results in a difference between the ground state energy of the positron in the total foil. For the WMo foil, the potential step has an experimental value of 0.64 eV. [61] Therefore positrons gain energy when entering the Mo foil from the W foil by crossing this step potential. After thermalization in the Mo layer, positrons are not able to penetrate the step potential to return W layer and are therefore reflected towards the Mo face. A transmission efficiency of 17% has been measured for a 110 nm WMo foil (composed of 10 nm W and a 100 nm Mo layers) with an implantation energy of 3 keV. [52]

4.2.3.2 *In-situ* Annealing

Prior to the operation of the spectrometer, the moderators can be refreshed with the utilization of *in-situ* annealing. This will maintain the performance of the moderator by minimizing the formation of non-equilibrium defect and cleaning of the surface from contaminants. This annealing is achieved using electron bombardment annealing.

The electrons are emitted from a hot tungsten filament. The tungsten filament is fabricated by winding tungsten wire around a small diameter rod. Once wound, each end of the filament is spot welded to a 16 AWG stainless steel wire. The filament is then thermally and electrically isolated from the support flange using aluminum oxide insulators. The support flange is a 2-3/4" conflat flange with a 2 pin, 2 kV, 16 A feedthough. The copper feedthrough connections are then attached to the stainless steel wires at the ends of the filament using inline electrical clamps.

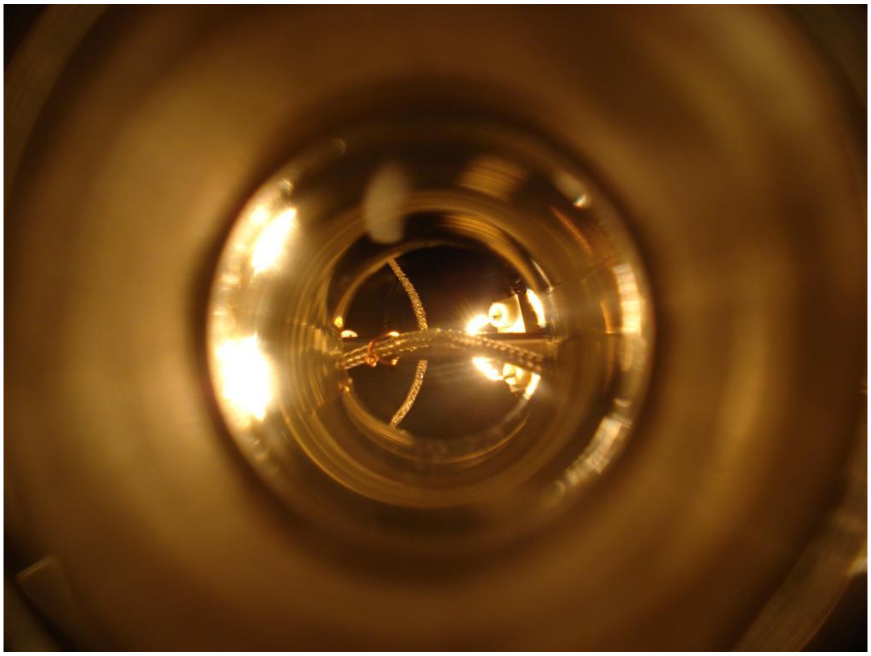

Fig. 4.14. Image displaying filament with 1 A of applied current while the remoderator is within the beamline.

A current of 1 A is applied to the filament using a GW Laboratory DC power supply, model #: GPS-1850D. This is enough to sufficiently heat the filament and allow for outgassing. After outgassing, the current supplied to the filament is removed and the moderator is extracted from the axis of the beamline and placed directly in front of the tungsten filament. A Glassman High Voltage high voltage power supply, model #: PS/EQ010P120-22, is used to apply +10 kV of potential to the moderator at a current of 0.1

A. Once the potential is applied, the application of current to the filament will eject electrons from the filament surface where they are accelerated towards the moderator, providing the annealing. The moderator is annealed in flashes to minimize the possibility of melting the holder.

4.2.4 The drift stage

Following the moderator stage, a straight segment is required to allow the positrons to drift to the buncher and around an internal shield. The drift stage is simply a 4” OD solenoid 33.25” long vacuum chamber.

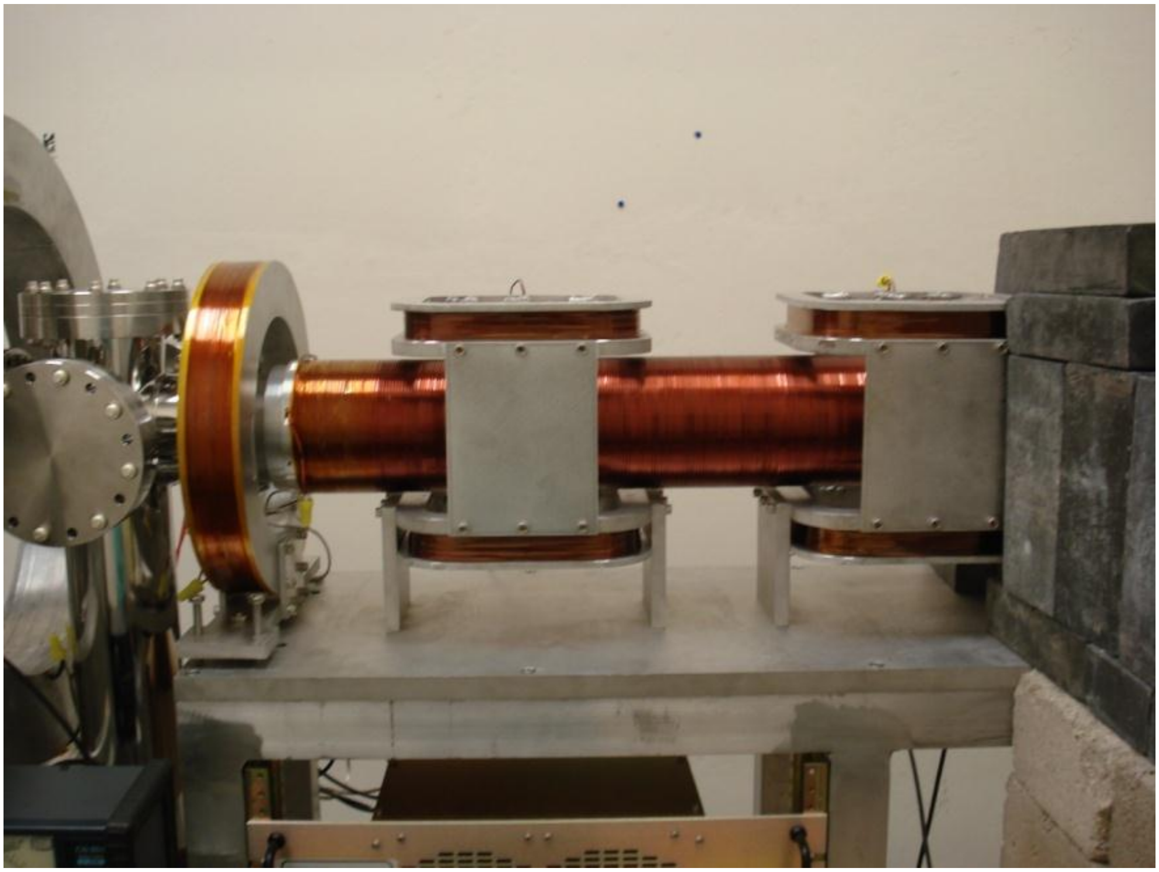

Fig. 4.15. Image of the solenoid, termination coil, and steering coils for the drift portion of the pulsed positron beam.

A four layer solenoid, composed of 10 AWG square copper magnet wire with enamel insulation, is wound directly on the surface of the vacuum chamber. The solenoid was wound using the welding positioner and winding began next to an aluminum collar which supported one end of the solenoid windings. The final 3” of the solenoid layers are wrapped in Kapton tape to prevent the layer from unwinding. As seen in fig. 4.15, one end of the solenoid is supported by the moderator chamber, which is hidden by lead bricks in the image, while the opposite end is supported by a customized 6-way cross.

Figure 4.15 also displays the two sets of steering coils which are placed around the solenoid to guide the positrons around an internal lead shield. The steering coils were mounted to the chuck of the welding positioner which expanded to grasp the coil form. Rough edges were smoothed from the side and base of the coil forms to reduce the risk of surface imperfections damaging the wire insulation. Small channels are placed in the side of the forms to allow the wire to penetrate the form to ensure smooth coil layers. Kapton tape is wrapped around the wire to again reduce the possibility of the form cutting through the wire’s insulation. Once the coils were wound, one transverse coil set was assembled to measure the transverse field strength. A current of 2A was supplied to the assembly and the magnetic field strength was measured at 0.5” increments through the center of the set. The coils were wired in series so each coil would receive the same current. The results of this measurement are displayed in fig. 4.16. The 2A current is capable of generating a transverse field in excess of 6G. This measurement indicates that the available power supplies can generate transverse fields which are capable of successfully steering the positrons around the internal shield.

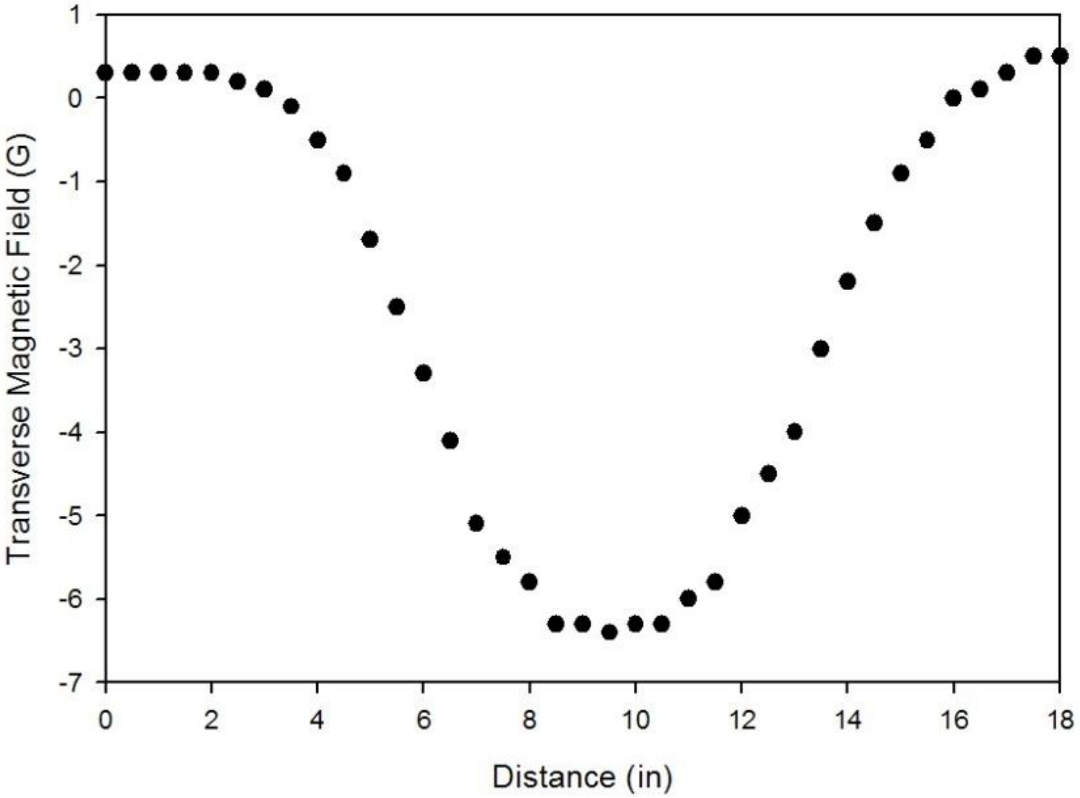

Fig. 4.16. Map of the transverse magnetic field produced by a steering coil with the application of a 2 A current.

Because the moderator must be held at a negative potential to enable slow positrons to be emitted from the opposite surface of the transmission moderator, the entire beamline must be capable of being negatively biased. This requires that a drift lens must run the length of this chamber to maintain the proper kinetic energy, i.e., if the beam were held at ground potential, re-emitted positrons would be attracted back to the surface of the remoderator. The drift lens consists of an aluminum tube split down the middle to allow the inner surface to be cleaned. Aerodag G is again applied to this lens, preventing surface charging that could alter the transport of the beam. The 1” lead shield is placed within the lens with 4-40 screws preventing the shield from shifting. The lens is reassembled using Teflon and aluminum rings. The aluminum rings maintain the two lens halves at the same potential, while the

Teflon rings have a larger diameter and isolate the lens from the inner walls of the vacuum chamber.

Fig. 4.17. Image of the drift lens for the pulsed positron spectrometer. The lens is cut in half and reassembled to allow the application of graphite to the internal surface and the installation of the internal shield.

4.2.5 The Double-gap Harmonic Buncher

The buncher consists of a 7" long cylindrical electrode, mounted to a 6" double-sided conflat flange. The application of a 50 MHz rf voltage results in the production of two acceleration gaps at the entrance and exit of the electrode. Five additional lenses are placed before the bunching electrode to accelerate the positrons to the desired potential. The first four lenses are simply 0.125" thick disks while the final lens extends through the conflat flange to maintain the elevated potential to the bunching electrode. An aluminum disk is attached to the double sided conflat flange to support the buncher's outer cavity. An array of 8 holes are bored through the assembly to allow 0.125" alumina tubes to pass through. These tubes are used to support the lenses, which are placed on the outside of the conflat flange, and the bunching electrode. Each lens is isolated using 0.1" spacers, manufactured by Kimball Physics Inc. The assembly is secured using 0-80 threaded rods, which pass through the alumina tubes.

Fig. 4.18. Images of the assembled double gap buncher.

The outer diameter of the bunching cavity is 2.5” to simplify the fabrication of the components. This meant the outer diameter of the bunching electrode must be 1.086” to yield a 50Ω transmission line.

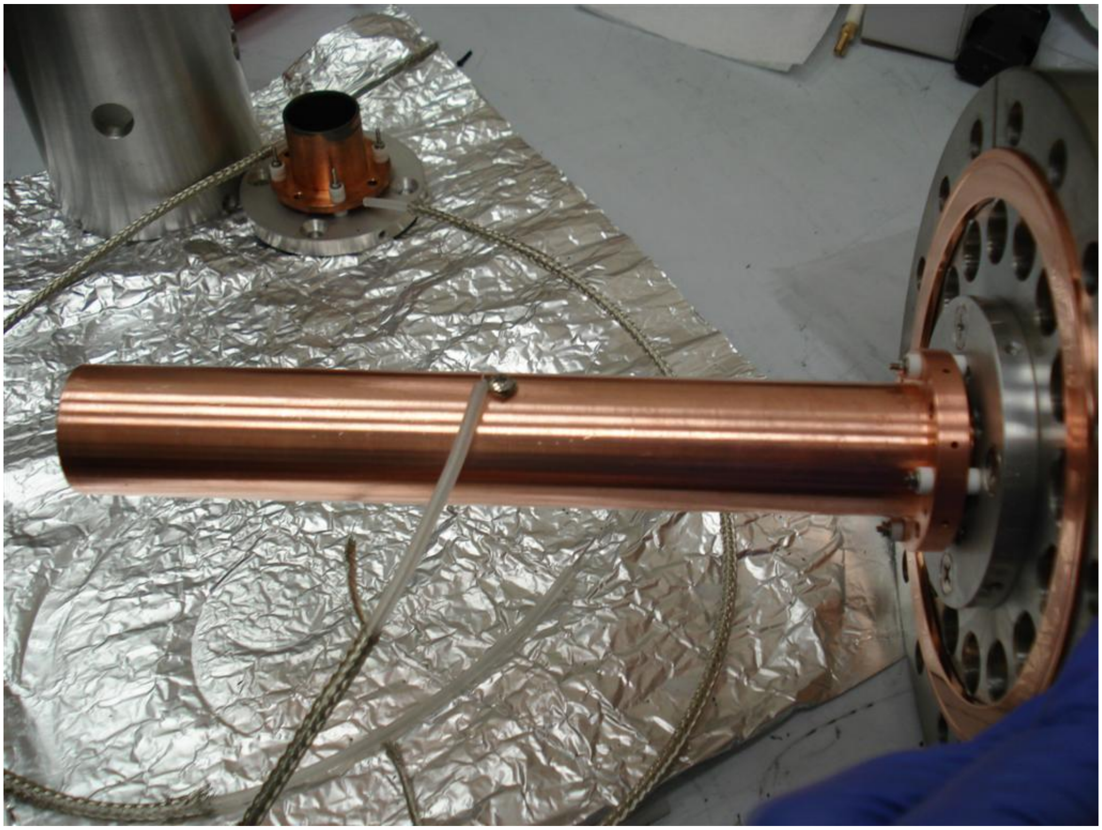

Fig. 4.19. Image of the bunching electrode with the power supply cable attached.

Prior to assembly, the copper bunching electrode was cleaned using a nitric acid solution to remove the oxide layer on the surface. Holes are bored through the outer cavity of the buncher to aid in pumping. A RG-58/U coaxial cable is used to supply rf power to the bunching electrode. The outer insulation layer is removed from the cable to minimize outgassing into the system, exposing the outer braided conductor. One end of the coaxial cable is attached to the center of the bunching electrode. The outer conductor of the coaxial cable is then attached to the grounded outer cavity of the buncher. The opposite end of the cable is attached to an MHV connector.

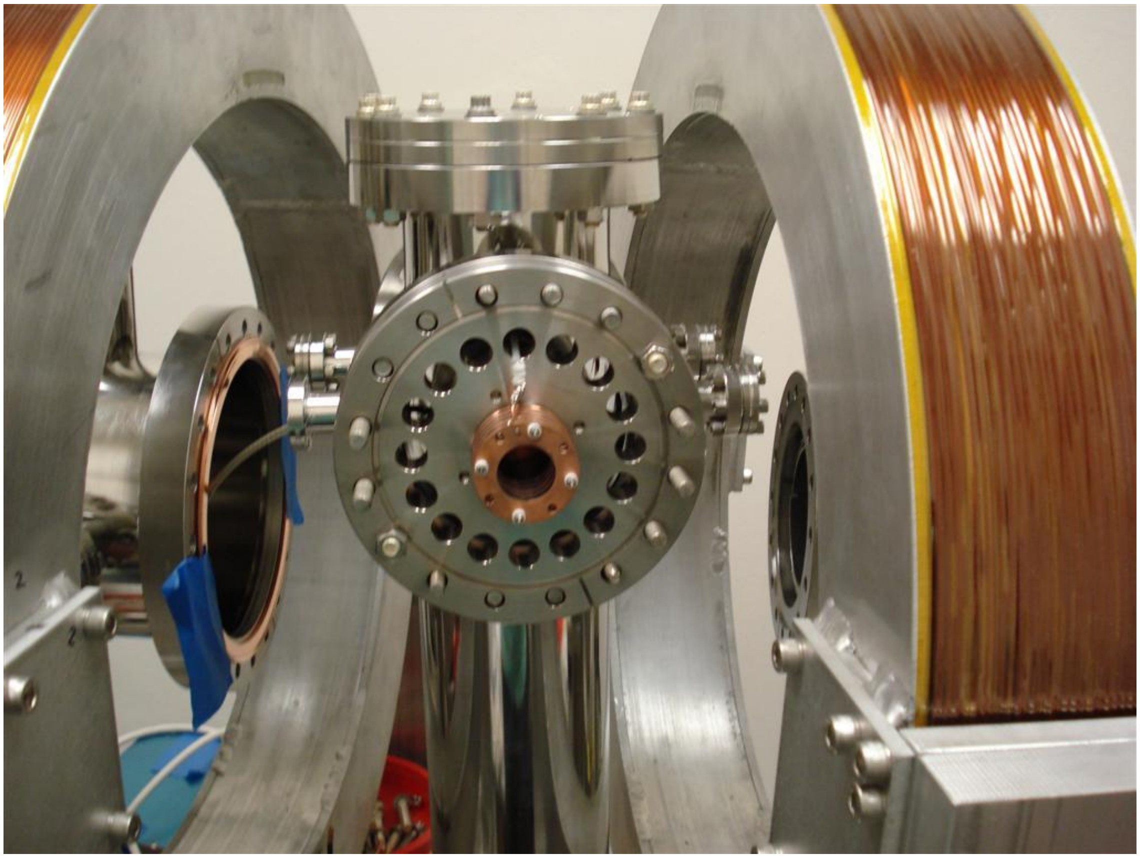

Fig. 4.20. Image of the double gap harmonic buncher installed in the bunching chamber prior to assembly of the vacuum system

Utilizing a MHV connector within the vacuum chamber and attaching the connector to a MHV feedthrough on a 1.33” conflate flange ensures that the supplied rf is shielded from the rest of the beam. Once assembled, the buncher was inserted into the buncher vacuum chamber, where it was temporarily supported by two bolts. Voltages on lenses near the bunching electrode are supplied using coaxial cable, with the outer insulation removed. The shielding conductor of each cable is grounded to the outer cavity of the buncher, with the opposite ends also grounded, in an attempt to minimize the effect of residual rf from reaching the lenses surrounding the buncher. The high voltage feedthrough is placed on the bunching chamber, therefore the bunching chamber contained all the electronic connections for lenses around the buncher, aiding in the assembly of the vacuum chambers. The bunching chamber was then rotated to be in line with the rest of the beam, the temporary bolts were removed and the chamber with buncher flange was slid into place, mounting to the solenoid support chamber.

4.2.6 The Target Chamber

The target vacuum chamber is constructed from a 12” long 8” outer diameter stainless steel tube. The chamber is attached to the rest of the buncher using an 8” to 6” zero length reducer flange. A Lesker fast-entry door is installed on the target chamber to allow easy access to the internals of the beam to change samples. A glass envelope ionization gauge is also installed to the target chamber to measure the pressure of the beam.

The end of the target chamber is sealed with an 8” conflat flange fabricated with a detector well. This well allows the detector to be placed as close to the sample as possible and the thin walls minimize attenuation of the annihilation gamma-rays. A Teflon spacer is attached to the inner surface of the detector well to support the sample electrode. The sample holder is a 0.25” plate which clamps onto the sample under investigation.

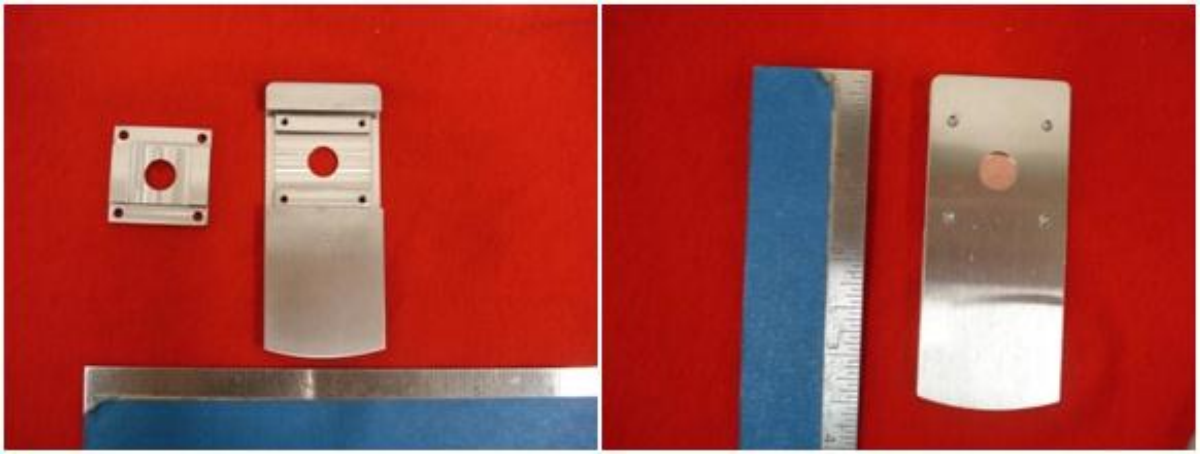

Fig. 4.21. Image of the stainless steel sample holder.

A 0.45” in diameter hole is machined through the holder, which is located to correspond to the axis of the beam line when the holder is fully inserted into sample electrode, therefore centering the sample in the beamline.

Fig. 4.22. Image of the sample holder and accompanying drift lens. The lens stack is attached to the detector well of the vacuum chamber using a Teflon holder.

A clamp is placed behind a cutout in the sample holder to hold samples in place. This clamp contains small ledges to prevent samples from sliding out of the holder, but limits the size of samples to 0.75"x0.75". This holder is machined to slide into a 0.25" support plate, also composed of stainless steel, which provides a constant bias to the sample. The close tolerances of the sample holder allow good contact between the holder and sample holder support, meaning the application of a negative potential to the sample support biased the sample for depth profiling.

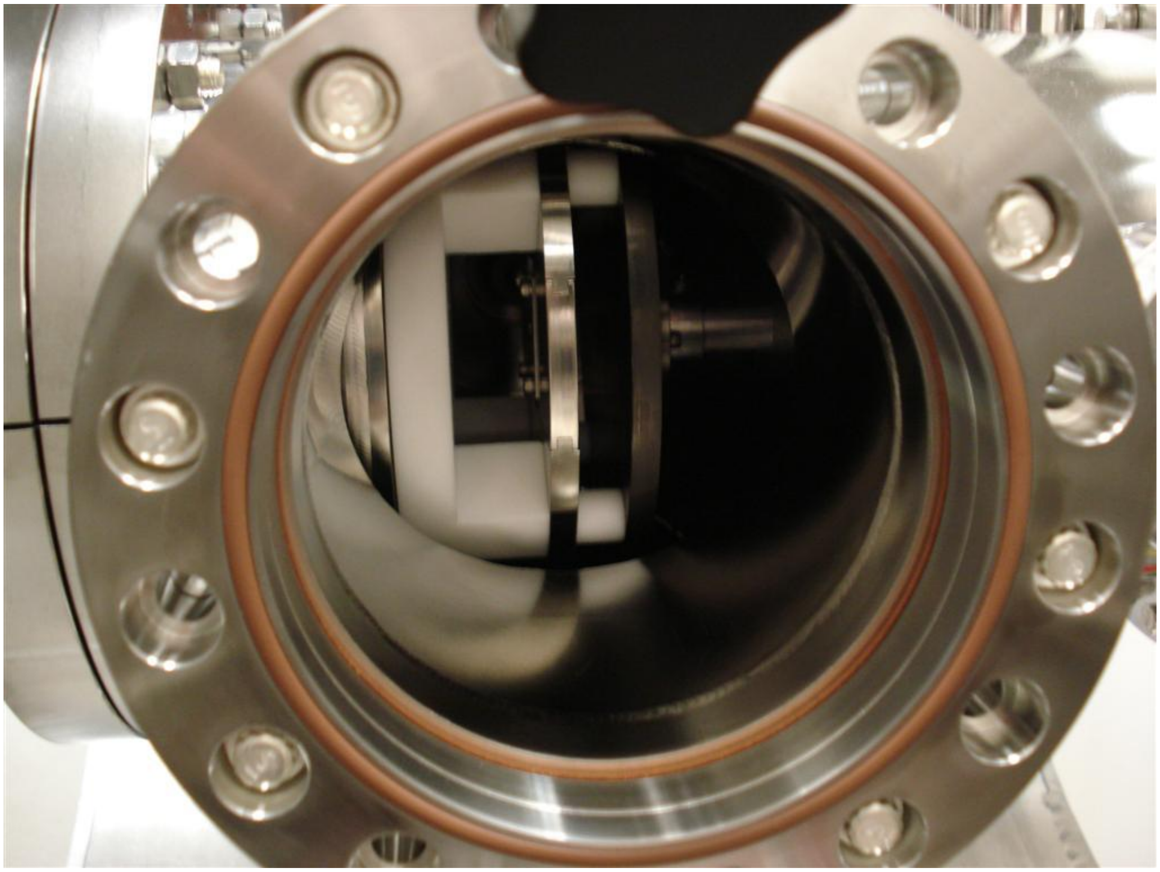

Fig. 4.23. Image of drift lens and sample holder installed in the pulsed positron beam.

An additional plate is placed behind the sample electrode to ensure a constant field between the drift lens from the buncher and the sample electrode. An image of the assembled target assembly can be seen in fig. 4.22. The sample holder is separated from the drift lens by 0.5" and from the end of the detector well by 1.375”. This spacing should ensure that the sample bias should reach up to -30kV.

4.3 RF-electronics system

All periodic waveforms utilized by the pulsed positron beam are generated by a Tektronix 3102 dual channel arbitrary function generator. This function generator is capable of producing a sine wave with a frequency of up to 100 MHz and user defined arbitrary functions up to a frequency of 50 MHz, with peak-to-peak voltages up to 10 V_{pp}. The phase of the two channels can be adjusted relative to each other.

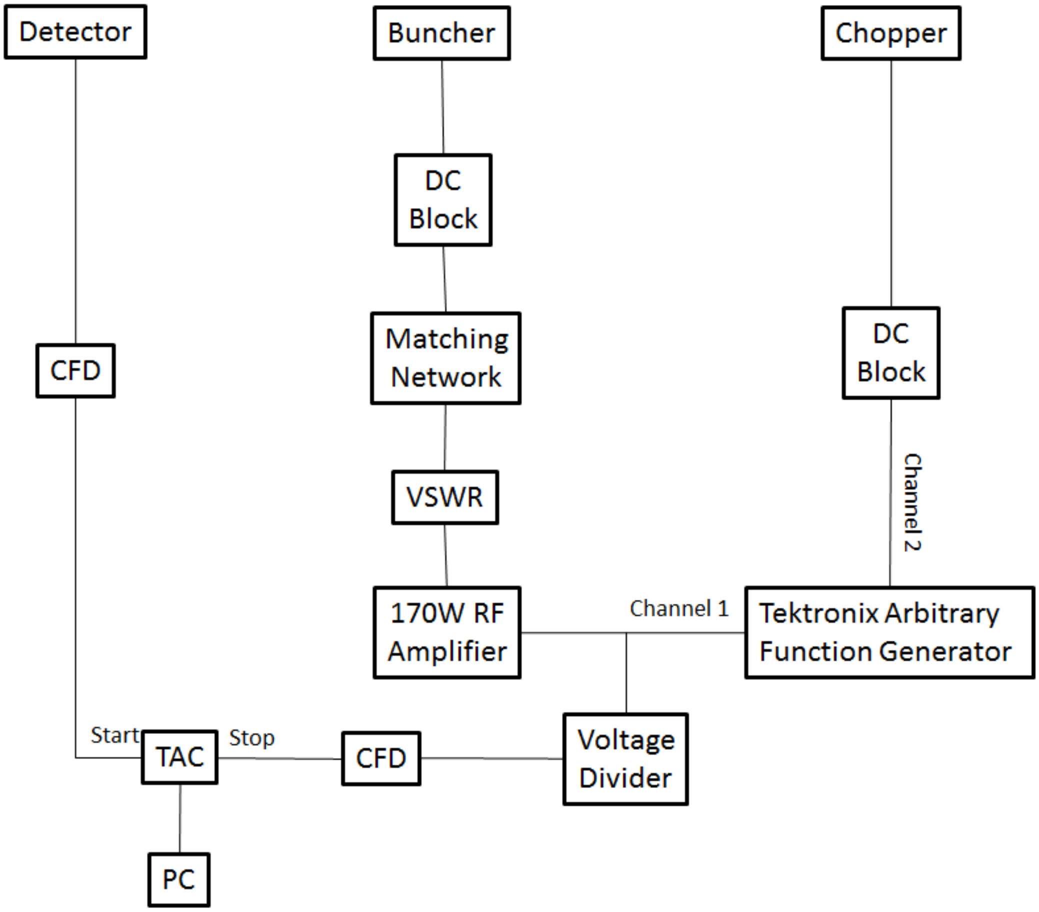

Fig. 4.24. Flow diagram of the rf electronics used for the pulsed positron spectrometer. A single arbitrary function generator is used to provide power for the rf amplifier, a stop signal for the TAC and the square waveform for the chopper.

A 50 MHz sine wave is produced by the first channel of the arbitrary function generator and is sent to a 50 MHz, 170 W rf amplifier, manufactured by TE Systems, where the input power of the AFG is amplified to its final power level. The amplifier is set up so the maximum output power of the AFG, 0.25 W, corresponds to the maximum output power of the amplifier, 170 W. The amplified signal is then sent to a VSWR meter, which displays the forward and reflected power and the standing wave ratio (SWR). A lower SWR indicates the better impedance matching between the source and the load.

Matching the impedance of the amplifier and the load is necessary to ensure the optimum power transfer to the load.

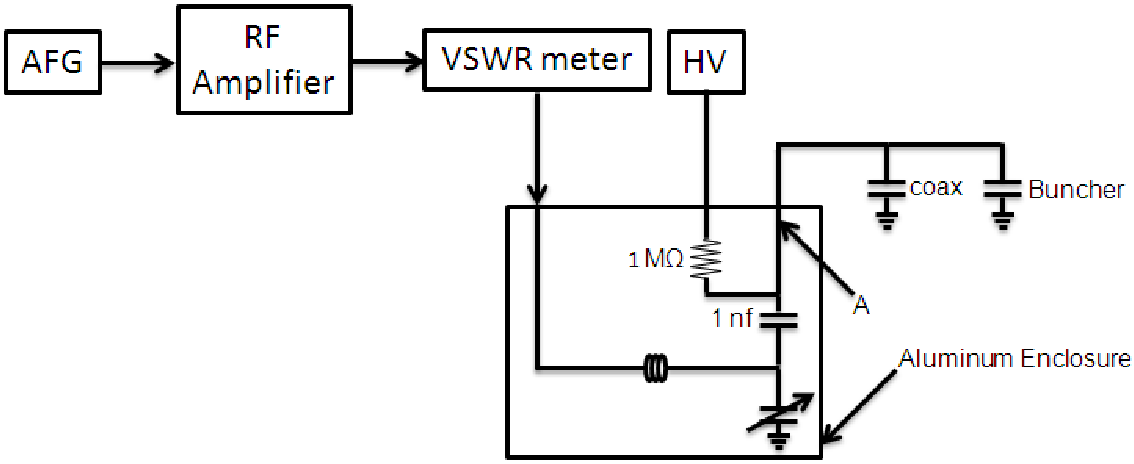

Fig. 4.25. Flow diagram for power applied to the buncher, including a wire diagram for the impedance matching network.

The impedance matching network is contained within an aluminum enclosure. The buncher acts as a coaxial capacitor and forms a series LC circuit, with a variable capacitor in parallel to the buncher and an inductor in series with the capacitors. Changing the capacitance of the variable capacitor modifies the equivalent capacitance of the network and allows the circuit to come into resonance. At resonance, the impedance of the inductor is equal to the impedance of the capacitor network, but is 180° out of phase, therefore cancelling the complex impedance of the load.

The value of the inductor must be determined to bring the circuit into resonance at 50 MHz. The capacitance was measured at the contact of the BNC bulkhead installed on the enclosure. The measurement indicated the capacitance of the coaxial cable and the buncher, which are in parallel, was 114 pf. This was combined in series with a network of 2 1 nf capacitors in parallel. These two capacitors have a breakdown voltage of 6000V, therefore the rf signal is capable of propagating past the capacitors, but a DC voltage up to -6000V applied to the bunching electrode is isolated from the rf electronics. The reactance of the 1nf capacitor at 50 MHz is only 3Ω; therefore the equivalent impedance of the two capacitors is only 1.5Ω and would not significantly affect the reactance of the circuit. The equivalent capacitance of capacitors in series can be determined by:

$$C_{eq} = \frac{C_1 C_2}{C_1 + C_2} \tag{4.23}$$

and was found to be 102 pf. It was assumed that the variable capacitor would supply a capacitance of 50 pf, with an equivalent capacitance found by:

$$C_{eq} = C_1 + C_2 \tag{4.24}$$

resulting in an equivalent capacitance of 152 pf for the network of capacitors.

The resonance condition for an LC circuit is that the angular frequency ω must be equal to the inverse of the square root of the product of the inductance of capacitance of the circuit.

$$\omega = \frac{1}{\sqrt{LC}} \tag{4.25}$$

Therefore, the inductor strength required to bring the circuit into resonance can be determined as:

$$L = \frac{1}{4\pi^2 f^2 C} \qquad 4.26$$

Inserting the equivalent capacitance, 152 pf, and the desired resonant frequency, 50 MHz, the inductor must have an inductance of approximately 0.067 μH. The next task is the determination of the dimensions of an air wound coil which results in the desired inductance. This can be estimated by:

$$L = \frac{d^2 N^2}{18d + 40l} \qquad 4.27$$

where d and l are the diameter and length of the coil, respectively, in inches, and N is the number of coils. [77]

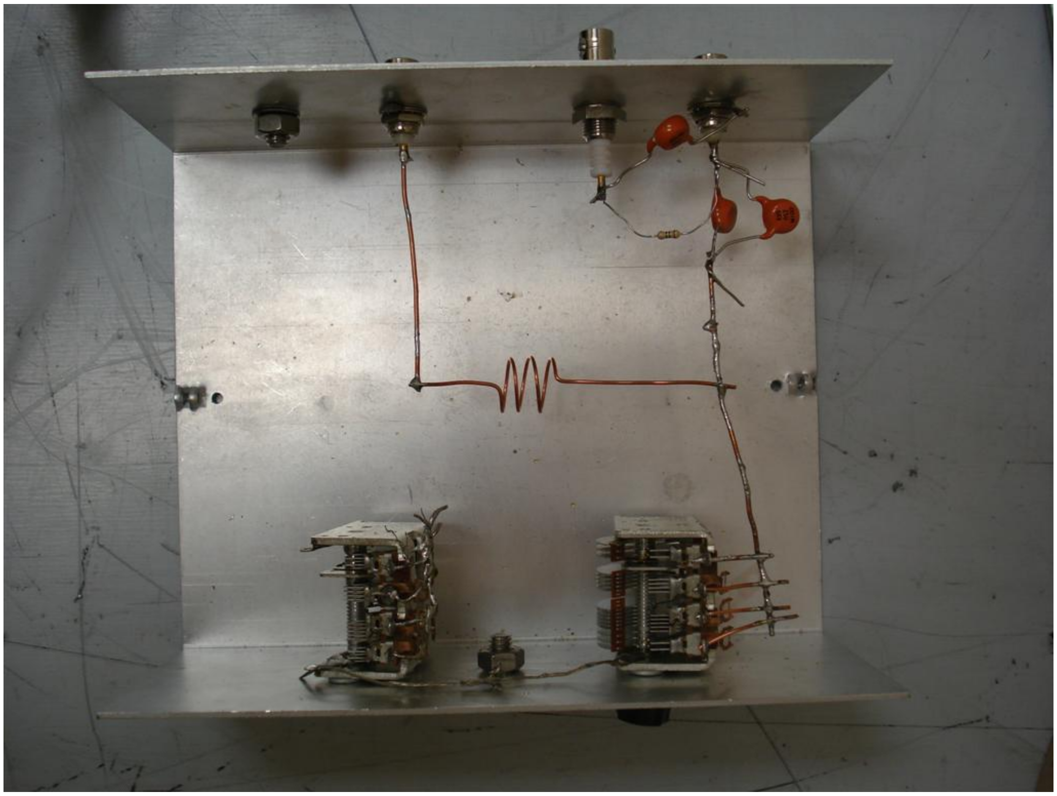

Fig. 4.26. Image of the assembled impedance matching network.

A coil composed of 3 0.5” coils spread over 0.625” results in an inductance of approximately 0.066 μH. Channel 2 of the arbitrary function generator is split to supply a 50 MHz time-varying-potential to the remoderator and a stop signal to the time of flight electronics.

4.4 Power Interlock

When the rf amplifier is first engaged, there is a short transient time of instability where the amplitude of the applied rf fluctuates. Once the amplifier has operated for a period of time, the applied waveform becomes stable. The amplifier stability can be maximized by allowing it to operate continuously. This leaves the buncher vulnerable to possible damage due to the input power supplied to the buncher being dissipated as heat. If the applied power were to melt the internal wiring, the pressure of the spectrometer could dramatically increase, leading to shorts in the system. To account for this possibility, a power interlock was constructed which would turn off power to the amplifier in the event of an increase in pressure.

The interlock is simply a comparator integrated circuit which supplies a control voltage to a relay. A comparator IC compares the magnitude of two input voltages. If the non-inverting signal is higher than the inverting signal, the comparator outputs a desired output voltage. When the magnitudes of the voltages are switched, the comparator does not output a voltage, eliminating the control voltage to a relay. When the relay is tripped, power supplied to the rf amplifier power supply and AFG would cease, effectively shutting of the buncher. Because the AFG would also be powered through the relay, the AFG would reset, meaning the buncher would not turn on again until the AFG is reset manually.

A wiring diagram for the power interlock can be seen in fig. 4.27. The pressure of the spectrometer is monitored using a Bayard-Alpert (hot filament ionization gauge) Board in a Varian Multigauge controller.

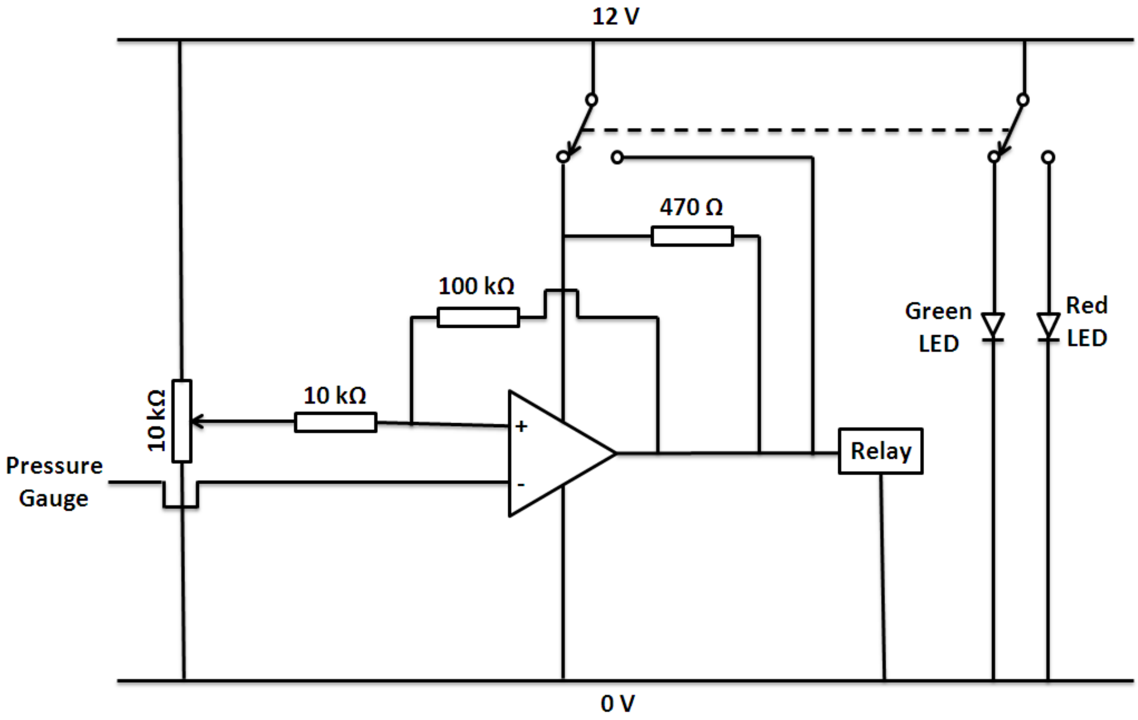

Fig. 4.27. Wire diagram for the power interlock.

The B-A board outputs a reference voltage which can be used as a pressure recorder. The output voltage is calibrated to the pressure measured by the ionization gauge and therefore can be used as the inverting signal for the comparator. The non-inverting voltage can then be a reference voltage produced by a potentiometer calibrated to a desired shut-off pressure. If the pressure in the spectrometer were ever to increase to a point where the recorder output voltage was in excess of the set point, the control voltage supplied to the relay would cease and the power supplied to the amplifier and AFG would shut off, therefore protecting the beam from damage. If the pressure increase were due to the power applied to the buncher, shutting off the amplifier would allow the beam to return to its base pressure. The interlock also has a bypass so the pressure gauge can be disabled but the relay will still provide power to the amplifier if needed for testing purposes.

As the pressure of the spectrometer decreases and the gauge output voltage nears the reference voltage, the relay could cycle on and off as the gauge voltage fluctuates about the reference. This would lead to oscillations in the power supplied to the electronics, which could lead to damage to the amplifier and AFG. To prevent this, a hysteresis must be added to the circuit. The hysteresis will cause the reference voltage at which the relay trips off to be higher than the reference voltage at which the relay turns on. This will mean that the relay will not turn on until the pressure of the spectrometer is well below the shutoff point. To accomplish this, the 12 V output of the comparator is sent to the non-inverting input through a 100 kΩ resistor. Therefore the reference voltage for the non-inverting input would be the sum of the voltage from the potentiometer and the output of the comparator. If the pressure of the spectrometer was to increase higher than the set point, the 12 V control voltage from the comparator would not be sent back to the non-inverting input, therefore the reference voltage would only be supplied by the potentiometer, changing the set point to a lower value. This decreased value means the pressure must reach lower levels before the control voltage is supplied to the relay.

To determine the reference potential supplied potentiometer Kirchhoff's law must be applied to the non-inverting input. The current flowing into and away from the non-inverting input must be equal, therefore:

$$\frac{V_r - V_-}{10\ k\Omega} = \frac{V_- - V_0}{100\ k\Omega} \tag{4.28}$$

where V_r is the reference voltage from the potentiometer, V_o is the output voltage of the comparator, and V_- is the input voltage of the non-inverting input. The output voltage of the comparator is 12.09 V. Assuming that V_- is 4.45 V, which would provide a shutoff voltage that corresponds to a pressure of $4.9\text{x}10^{-7}$ torr, V_r must be set to 3.74V.

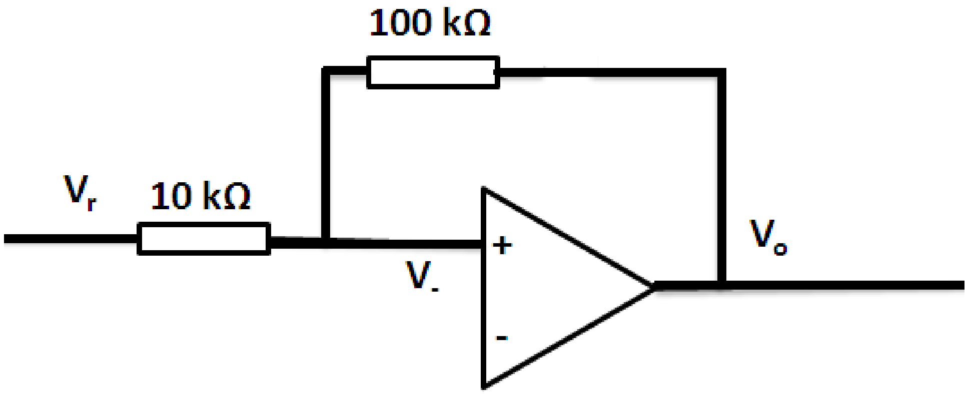

Fig. 4.28. Circuit diagram for the non-inverting input of the comparator.

Chapter 5 Testing and Results

Positron annihilation lifetime spectroscopy has proven to be a valuable tool in characterizing the nanophase structure of materials. There are many techniques that are capable of probing these defect structures, but the use of positrons results in a nondestructive measurement technique which is able to probe open and closed volume defects. The typical bulk positron lifetime measurement is carried out using a “fast-fast coincidence” setup, where a radioactive source (Na-22) is placed between the samples under study. Positrons enter the sample and thermalize, annihilating in defects within the sample. This sample geometry is placed between two scintillation detectors with short rise times to ensure high timing resolution. The electronic signals produced by the photomultipliers of the scintillators are processed using constant fraction discriminators to produce conventional fast timing logic pulses. The discriminators also provide energy selectivity to the two detectors, therefore one detector only recognizes the 1.27 MeV gamma ray produced by the Na-22 source, while the other detects the 511 keV gamma ray produced by the annihilating positron-electron pair. The fast timing pulses produced by the discriminators are then sent to the start and stop, including a sufficient delay in the signal arrival time, to a time-to-amplitude converter (TAC) which outputs a signal whose amplitude is proportional to the time interval separating the start and stop signals. [8] A majority of beam based positron lifetime spectrometers use Na-22 for their primary positron source, but the time correlation between the 1.27 MeV gamma and the birth of the positron is lost. For beam based slow positron lifetime spectrometers using pulsed positron beams, regardless of the source of the primary positrons, the 1.27 MeV gamma used to trigger the start of the timing electronics is replaced by a signal taken directly from the pulsing system of the spectrometer. By decreasing the pulse width, the deviation of the positrons from the electronic start signal is reduced. If perfect bunching were achievable, i.e. all particles arrived at the sample after the same time interval, the time resolution would be that of only the detector.

To fully understand the time resolution of the spectrometer, the various lifetime components involved should be examined. Once a positron is implanted in a material it reaches the thermal energy $\left(\frac{3}{2}kT\right)$ in approximately 10^{-12} seconds. [52] After thermalization, the lifetime of the positron can range from approximately 100 ps for a free diffusing positron to hundreds of picoseconds for positrons trapped in defects. [53] The actual time of the annihilation process of the positron and the electron is 10^{-21} seconds [6]. The dominant contribution to the positron lifetime is the time spent diffusing in the bulk or trapped in a defect. Following annihilation, the generated photons traverse the gap from the sample to the scintillation detector, which can take 10's to 100's of picoseconds depending on how far the sample and detector are separated. Because this time is fairly constant for every annihilation event, it contributes little to the final timing resolution.

The overall time resolution of the spectrometer is the quadrature sum of the positron pulse and the detector. The detector resolution is taken as the quadrature sum of the individual components which contribute to the spreading of the energy deposited into the scintillation crystal. [72]

$$\sigma^2 = \sigma_L^2 + \sigma_{edge}^2 + \sigma_{TTS}^2 \qquad 5.1$$

Assuming the spreading components are Gaussians, the overall time resolution of the detector is the product of 2.35 and σ. [65]

The value σ_L is attributed to the time spread due to variations in the optical path length of the photons in the scintillation detector. The interaction of the gamma ray excites the electronic states of the crystal introducing electron hole pairs. This excitation decays with the recombination of the electron-hole pairs, resulting in the isotropic emission of prompt fluorescence, and has a characteristic time period which is dependent on the scintillation material chosen. To maximize the light collected by the photomultiplier, the scintillator crystal is surrounded by a reflective material. Reflection from the surface of the crystal results in a deviation in the path length of the light to the photomultiplier. To minimize this time spread, smaller crystals can be used, because the path length of the photon in the scintillator would be smaller. The reduced time spread comes at the expense of detection efficiency. [65]

The crystal chosen will also emitted a certain amount of light per gamma interaction. A crystal which has a larger light yield will therefore produce larger pulses in the timing electronics. Larger pulses would have less timing jitter because the amplitude of the pulses would have less variation. [65] This is related to the term σ_{edge}, which is related to the timing jitter of the rising edge of the photomultiplier's output pulse. This jitter is proportional to the number of electrons *(N_{PE})* emitted by the photocathode of the photomultiplier.

$$\sigma \propto \sqrt{\frac{1}{N_{PE}}} \qquad 5.2$$

By narrowing the discriminator levels about the timing peak of interest, the timing jitter due to the rising edge would be proportional to the energy of the detected photon. [72] Therefore a scintillator with high light output per gamma interaction would produce a greater number of photo electrons from the photocathode, leading to a lower jitter due to deviations in the rise time of the pulse.

The photomultiplier used to increase the pulse height generated by the incident gamma-ray interaction can also generate spread to the detector resolution, which is related to the term σ_{TTS}. There is the potential to have a deviation in the transit time of the electrons through the photomultiplier. This can be decreased by increasing the voltage applied to the dynodes of the photomultiplier, which will increase the velocity of the electrons through the instrument, minimizing the transit time spread. Therefore, the time resolution of the detector is then composed of the decay time of the scintillator's excited states and the time resolution of the photomultiplier tube used to amplify the signal produced by the scintillator to a usable pulse.

5.1 The $LaBr_3$ Scintillation Detector

The detector used for the pulsed positron spectrometer is a Lanthanum-Bromide ($LaBr_3$) scintillator crystal (BrilLanCe 380) mounted on a Photonis XP20D0 photomultiplier tube. While most inorganic scintillators have a slow decay time for the excited states, cerium doped inorganic scintillators have been found to generate faster decay times with good light yield. When a charged particle created by a photon interaction traverses the scintillator, coulombic interactions within the crystal create electron-hole pairs. The electron and holes migrate to the dopant atoms, therefore ionizing the dopant atom, because the ionization energy is less than that of the host lattice. The electrons are free to migrate within the lattice until it falls into the energy bands of the dopant atoms. If the electron falls into one of the exited states of the dopant, there is a high probability of quickly producing a scintillation photon in the visible range, if the proper dopant is used. One advantage to producing scintillation photons with dopant atoms is the crystal is transparent to the resulting photons. This is because these photons have energies less the band gap of the bulk of the crystal; the scintillation photons cannot excite the crystal and reabsorb, therefore increasing the light output. [65] While the rise time of $LaBr_3$ is slower than the more typically used BaF_2 scintillator, because of this higher light output, the output pulse is larger, decreasing the effect of timing jitter on the pickoff time of the pulse. The time resolution of a pair of $LaBr_3$ detectors in an analog bulk PALS system was measured to be 192 ps using Co-60 as a source, while the same setup had a time resolution of 210 ps using BaF_2 detectors. [70]

The detector is placed within a holder mounted in the detector well at the end of the pulsed positron spectrometer. The detector holder consists of an aluminum tube welded to an 8” circular aluminum plate. An array of twenty 0.5” holes are bored in this aluminum plate to mount the holder to the endcap. The completed detector holder is aligned with the mounting holes of a standard conflat flange and was supported with four bolts. This configuration ensures the detector is on axis and as close to the target as possible. Unfortunately, while this is an ideal location for the detector, it places the detector within the axial field produced by the three large magnetic coils of the spectrometer. The magnitude of the field ranges from approximately 45 G at the scintillator to 30 G at the photomultiplier base. Photomultipliers are sensitive to magnetic fields due to their dependence on the use of electrostatic fields to accelerate the electrons through the array of dynodes to amplify the pulse. [65] The large axial field produced by the coils caused the detector to stop functioning. In an attempt the remedy this, the detector is placed within a magnetic shield, which is typically sufficient to shield photomultipliers from stray magnetic fields. This shield was purchased from Ad-vance Magnetics, Inc. and was a 10” long cylinder with a

0.040” wall thickness composed of their AD-MU-80 material. Unfortunately, the magnetic shield was not capable of attenuating the residual field to a point where the detector could function. To further decrease the magnitude of the residual field within the photomultiplier, a four layer solenoid is wound on the surface of the magnetic shield. This solenoid is wound using 22 AWG hookup wire which is rated to a temperature of 80°C. The application of 2.0 A, supplied by a GW Instek PSS-2005 5A-20V power supply, to the solenoid, in the direction opposite to the current passing through the guiding coils of the spectrometer, reduces the field to a point where the detector can successfully operate. By decreasing the axial field of the spectrometer in the region of the target to 1.75 A, the required current through this detector coil could be reduced to 1.7 A.

5.2 Discriminator Energy Selection

The timing electronics of the pulsed positron beam determines the time difference between logic pulses generated by constant fraction discriminators. The best timing characteristics occur when the input pulses are bound to a narrow range of amplitudes, therefore minimizing the effect of amplitude walk on the time pick-off, leaving time jitter to add uncertainty to the timing. [65] A constant fraction discriminator can be used to set an energy window about the 511 keV annihilation peak, therefore limiting the range of pulse amplitudes used for timing. The upper and lower level discriminators must be set so the output logic pulse is only generated when a pulse height corresponding to the 511 keV energy peak is detected.

To set the upper and lower level discriminators, the dynode pulse of the photomultiplier is sent to an amplifier, the output of which is sent to the input of the MCA. The anode pulse of the photomultiplier is sent to the discriminator. The logic pulse generated by the discriminator is sent to a gate/delay generator, which delays the pulse and sends it to the gate of the MCA. The gate/delay generator is needed to compensate for the slower pulses generated by the amplifier. When the MCA is run in coincidence mode, the MCA will only display an amplified dynode pulse when the logic pulse triggered by the anode arrives in coincidence.

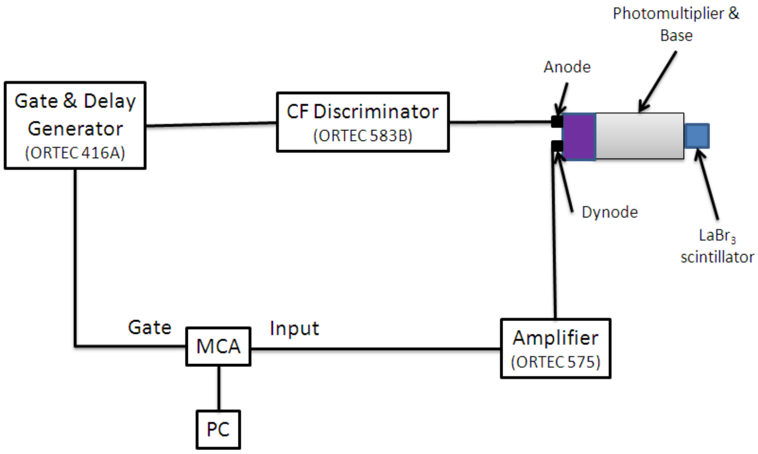

Fig. 5.1. Flow diagram for setting upper and lower discriminator levels of the constant fraction discriminator.

The discriminator only outputs a logic pulse when the pulse height of the detector anode falls within the specified window.

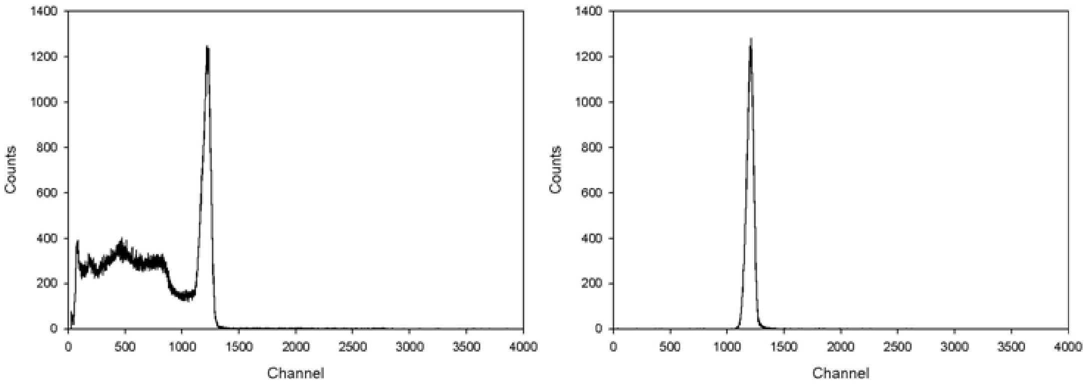

Fig. 5.2. Energy spectra taken with LaBr$_3$ scintillation detector of 511 keV annihilation peak with discriminator levels fully open (left) and energy window set around 511 keV peak

Therefore the energy spectrum only displays dynode pulses that correspond to the window set by the constant fraction discriminator. The upper and lower level discriminators are adjusted so only the detection of the 511 keV annihilation gamma rays yield a logic pulse.

5.3 Detector Efficiency

The $LaBr_3$ scintillation detector is placed within a detector well at the end of the pulsed positron spectrometer 1.625” behind the target. To minimize the detection of positronium annihilation and the annihilation of positrons re-emitted from the surface, 4 lead plates, 0.0625” thick, are mounted directly behind the sample holder. An addition 0.5” disk is placed within the vacuum directly behind the sample holder. A 1 cm hole is bored in the center of each producing a collimator to the detector. If a positron, or a positronium atom, is emitted from the surface of the sample and annihilates outside the bounds of this collimator, the chance of the 511 keV annihilation gamma-ray reaching the detector without scattering is reduced to 3%.

To determine the detection efficiency of this geometry, a Na-22 source was mounted in the sample holder. The sample was counted for 10 minutes, resulting in the energy spectrum presented in fig. 5.4. The count rate of 511 keV gamma-rays, corrected for background radiation, was found to be 330 cps.

The source strength was determined to be 10.1±1.7 μCi on June 30, 2010. On the day of the measurement the activity was calculated to be 9.7 μCi because 51 days had elapsed since the source calibration.

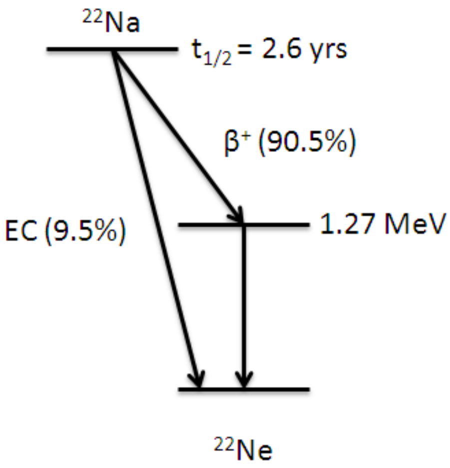

Fig. 5.3. Decay scheme for Na-22.

Sodium-22 decays via positron emission 90.5% of the time, resulting in a 1.27 MeV and two 0.511 MeV gamma-rays. This means 6.5×10^5 annihilation gamma-rays are emitted per second. The detection efficiency for the annihilation gammas is then taken as the ratio of the detected count rate to the calculated source intensity, or 0.05%.

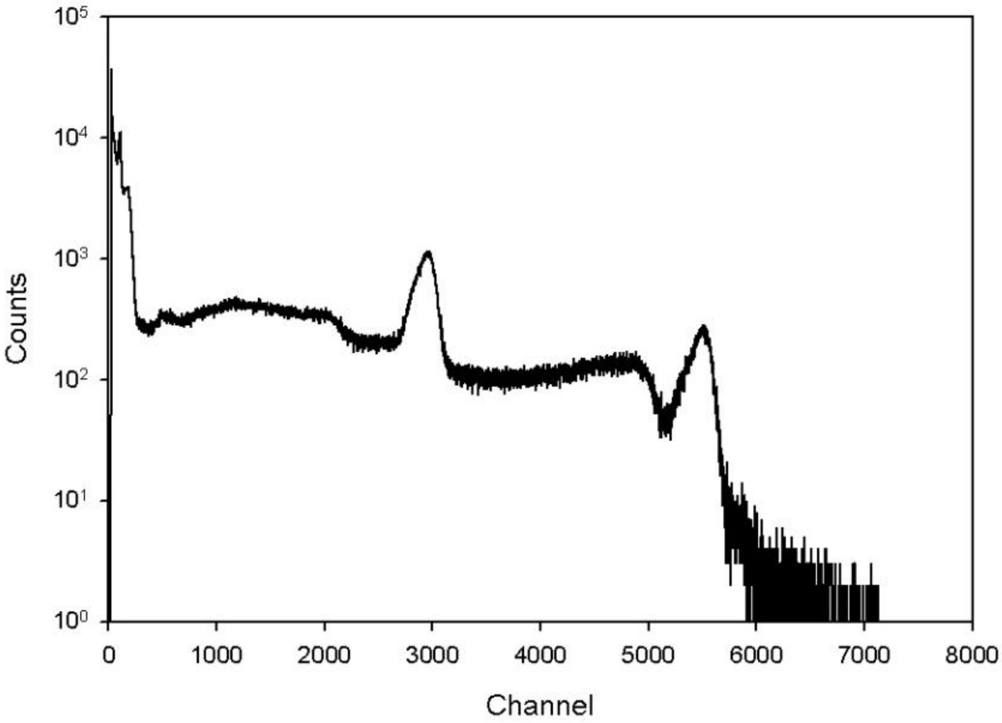

Fig. 5.4. Energy spectrum for Sodium-22 source placed in the sample holder within the target chamber using a $LaBr_3$ detector.

5.3.1 Increasing the Detection Efficiency

The sample is separated from the detector by a 1.375” Teflon spacer and the 3 mm thick wall of the vacuum chamber. Nothing is behind the sample, so a new spacer was fabricated allowing the sample to be located closer to the endcap which contains the detector. A Teflon disk with a thickness of 0.6” is sufficient to cover the end of the endcap and lead collimator while still providing 0.1” of insulation from ground.

Fig. 5.5. Image of the current target stage of the spectrometer (Left) compared to a modified moderator stage (right) with an expected detection efficiency of 0.21%.

This allows the sample to be 0.775” closer to the detector, leading to an increase in detection efficiency. The same Na-22 source used to previously measure the detection efficiency was again placed in the sample holder, although 251 days had elapsed since the previous measurement of the detection efficiency. A 600 second energy spectrum was recorded and the net number of counts in the 511 keV annihilation peak was determined. Moving the sample 0.775” closer to the detector increased the detection efficiency to 0.21%, an increase by a factor of 4.2.

5.4 Detector Timing Resolution

Because the $LaBr_3$ detector used to detect annihilation gamma-rays was placed within the axial magnetic field of the pulsed positron spectrometer, the time resolution of the detector was measured to determine the effect of the residual magnetic field on the timing performance on the detector. To determine the time resolution, two identical $LaBr_3$ detectors were utilized.

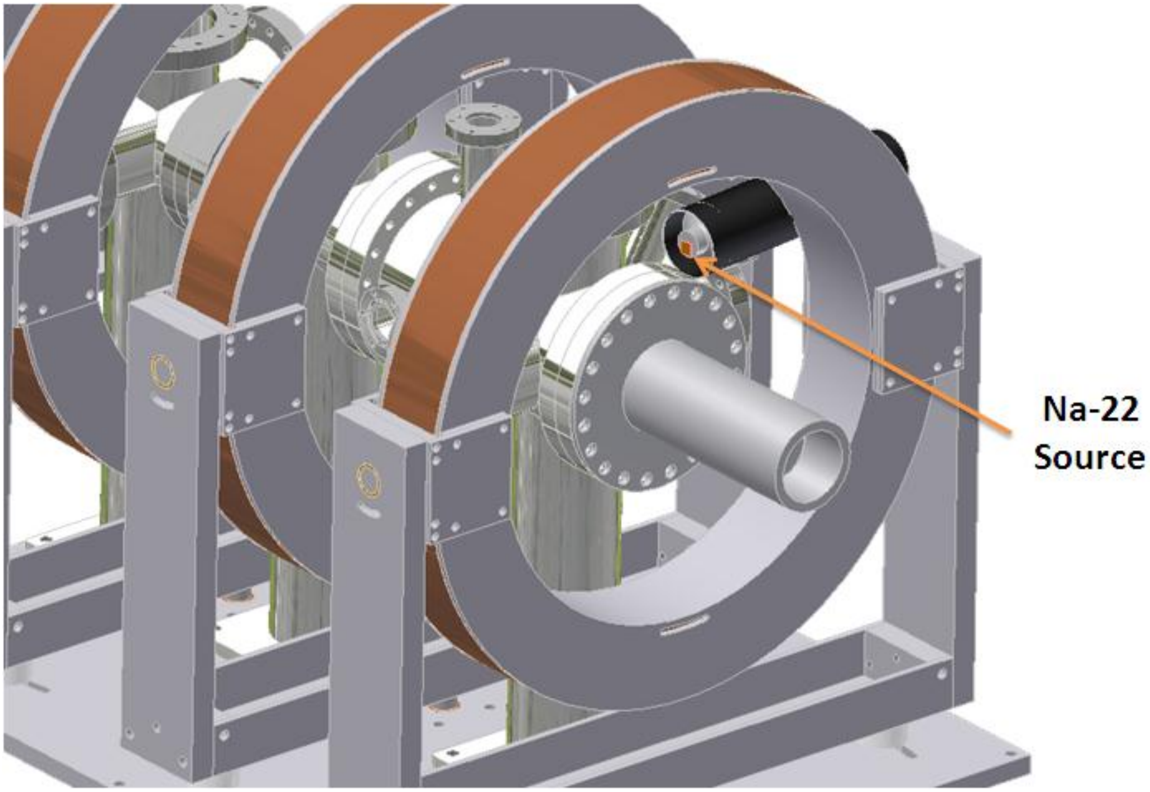

Fig. 5.6. Diagram of the detector placement for the determination of the time resolution of the $LaBr_3$ detector.

One detector, which acts as the detector for the spectrometer, was placed within the detector well at the end of the spectrometer and housed in the magnetic shield wrapped in coils used to decrease the internal axial field. The second detector was placed transverse to the axial field as close to the first detector as possible. This detector was also placed within a magnetic shield, but was oriented perpendicularly to the applied axial magnetic field of the coils. The Na-22 source was placed between these two detectors and energy windows were set so the arrangement would detect the coincident collinear 511 keV gamma rays generated by the source. A coincidence spectrum was collected with the axial magnetic field on and off. With the magnetic field off, it was assumed that the timing resolution for each detector was identical. Because the magnetic shield works best when the applied field is transverse to the shield, it is further assumed that the applied field has a negligible effect on the performance on the transverse detector. Therefore, differences between the coincidence spectra are attributed to the effect of the magnetic field on the spectrometer's detector. The results of the measurement are presented in fig. 5.7.

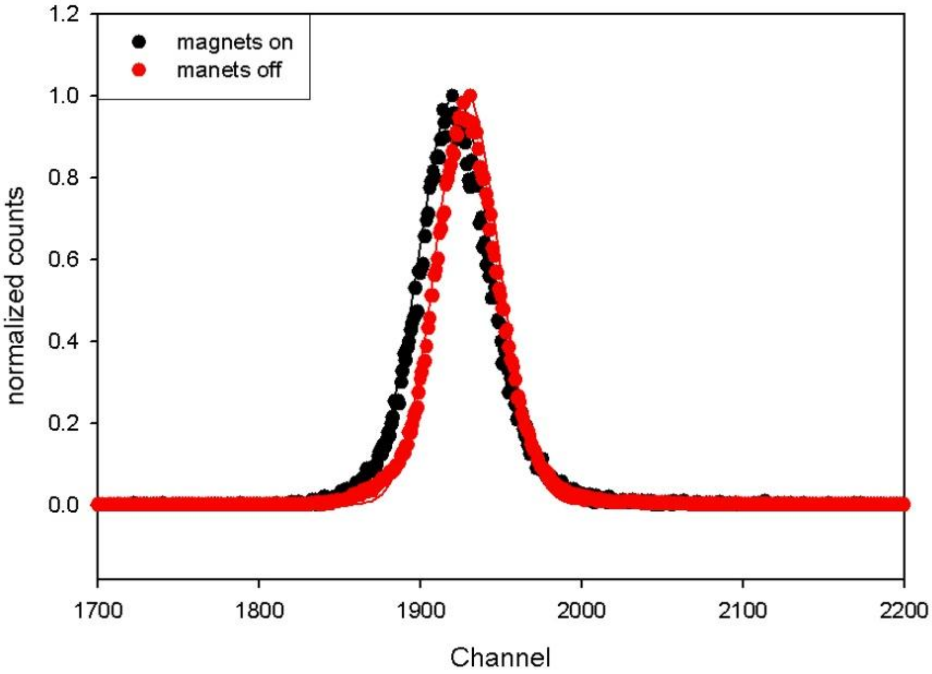

Fig. 5.7. Normalized coincidence spectrums for 511 keV gamma rays emitted from Na-22 source with axial magnetic field on and off.

A Gaussian distribution was fit to each of the plots showing that the time resolution of the detector arrangement was 320 ps when the magnets were on and 280 ps when the magnets were off. Because the overall timing resolution of the arrangement is assumed to be the quadrature sum of the time resolution of the two individual detectors, assuming each detector is identical with the magnetic field absent, the time resolution of the individual detectors is found to be 198 ps, i.e. the overall time resolution of the detector arrangement divided by the square root of 2. It is therefore assumed that the time resolution of the transverse detector is 198 ps, regardless of the presence of the magnetic field. Again, because the time resolution of the system is taken as the quadrature sum of the two detectors with an applied axial magnetic field, the time resolution of the spectrometer's detector is determined to be 251 ps.

5.5 Determination of the Phase Space of the Primary Beam

The primary positron moderator produces positrons with an angular distribution due to extraction and focusing from the moderator. The distribution can be measured within the pulsed positron spectrometer using a lens which applies a positive retarding potential to the primary beam. The retarding potential sets up an axial electric field which repels the incident positrons. If the positron's parallel energy is less than the magnitude of the applied field, the positron is reflected, resulting in a decrease the detected count rate at the end of the spectrometer. By measuring the count rate while increasing the retarding potential, the axial energy distribution of the incident positron beam can be determined. This axial energy distribution can then be related to the angular distribution of the primary positron beam.

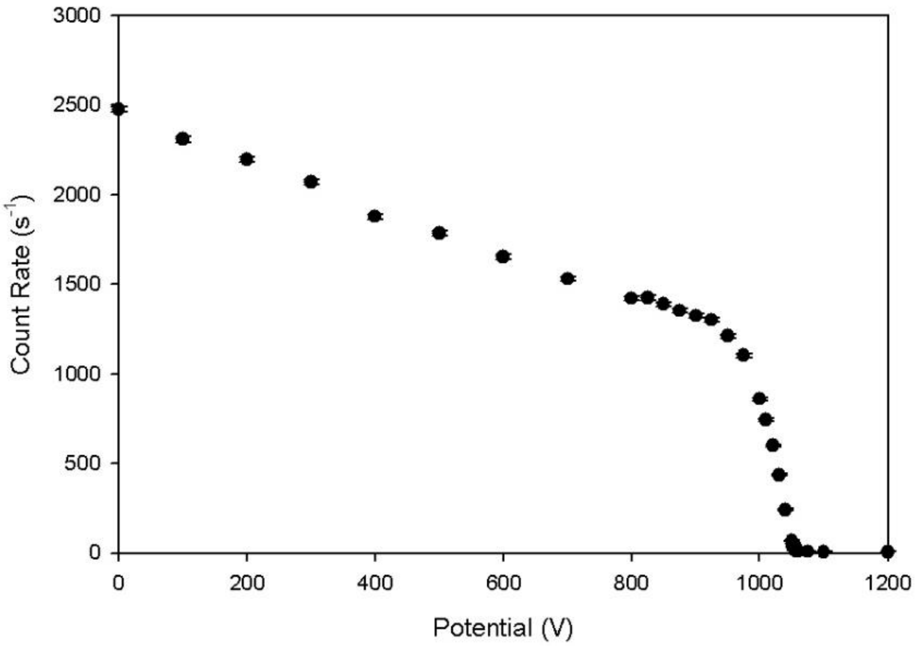

Fig. 5.8. Retarding potential vs. detected count rate for the primary positron beam.

The total momentum of a positron spiraling in the guiding axial field is the vector sum of the perpendicular and parallel momentum.

$$\mathbf{p}^2 = \mathbf{p}_{\parallel}^2 + \mathbf{p}_{\perp}^2 \qquad 5.3$$

The tangent of the angle between the perpendicular and parallel momentum is equal to the ratio of the two vectors.

$$\tan\theta = \frac{\mathbf{p}_{\perp}}{\mathbf{p}_{\parallel}} \qquad 5.4$$

For non-relativistic particles, the relationship between the energy and momentum is:

$$p = \sqrt{2mE} = \sqrt{2meV} \qquad 5.5$$

where ***p*** is the momentum, m is the mass of the positron and E is the energy. Using Eq.5.3, 5.4 and 5.5, the angle between the components of the momentum can be determined based on the energy of the beam and the applied retarding potential:

$$\theta = \tan^{-1}\left(\frac{V_{\max}}{V_{\|}} - 1\right) \qquad 5.6$$

where $V_{\|}$ is the magnitude of the retarding potential and V_{max} is the potential where the beam is almost fully eliminated. This is taken as the maximum energy because it would correspond to positrons with most of the momentum in the axial direction; therefore most of the kinetic energy is in the axial direction. From fig. 5.8, a retarding potential of 1057 V is statistically insignificant from the background, so it is taken as the maximum energy of the beam. Numerically taking the derivative of the results presented in fig. 5.8 and converting the retarding potential to angular values yields the angular distribution of the primary positron beam, as seen in fig. 5.9. The results indicate that 50% of the primary positron beam has an angular spread of 17° (FWHM) although there is a higher energy tail due to the two moderator banks and focusing.

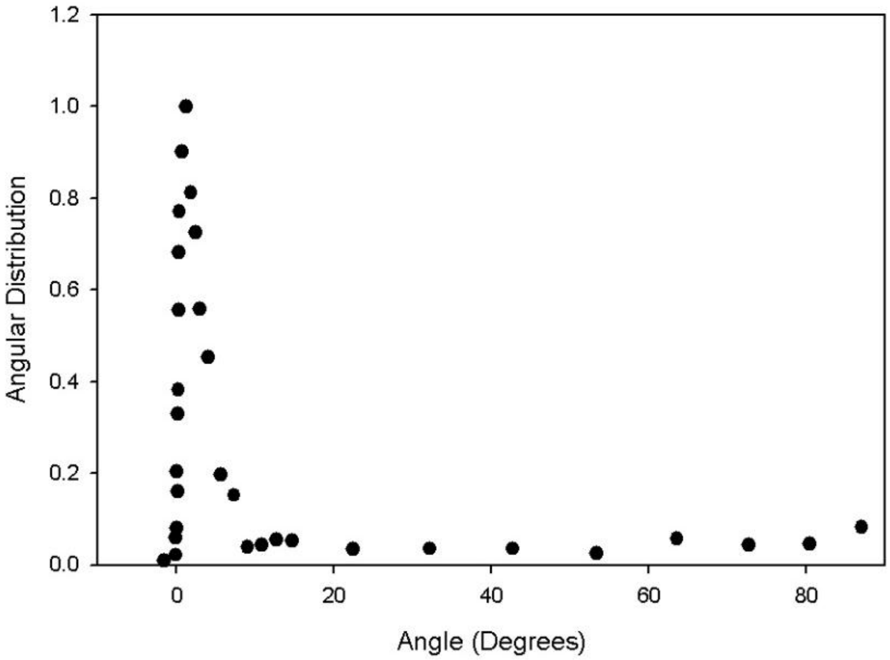

Fig. 5.9. Angular distribution of positrons from the primary positron beam normalized to 1.0.

5.6 Detection of the Presence of Slow Positrons

The positron transmission moderator foil could then be placed within the beam line to remoderate the primary positrons and minimize the angular distribution of the positrons utilized within the buncher. The first step was to flash anneal the moderator foil to condition the surface for optimum slow positron emission. The application of a retarding potential to a lens element will block positrons from reaching the target end of the spectrometer, i.e., if the retarding grid was less negative than the moderator, emitted slow positrons are attracted back to the surface of the moderator. A sharp jump in the detected count rate (occurring over a few volts of retarding potential) indicates the presence of slow positrons. The width of the step should be approximately equal to the work function of the moderator because the maximum energy of the reemitted positrons is equal to the work function.

As indicated in results presented in fig. 5.10, the detected count rate increases by a factor of 7 by reducing the extraction potential (relative to the moderator potential) by approximately 3 V. By fitting the data to a cumulative Gaussian distribution, the standard deviation of the distribution fit to the data can be related to the full width at half max (FWHM) of the energy spread of the positrons by: [65]

$$FWHM = 2.35\sigma \tag{5.7}$$

where σ is the standard deviation of the distribution. The energy spread of positrons emitted from the remoderator is found to be 2.3 eV. Because the positrons are emitted from the Molybdenum side of the remoderating foil, the positrons should have an energy spread which is characteristic of the Molybdenum positron work function. From literature, the work function of Molybdenum is -2.2 eV. [7]

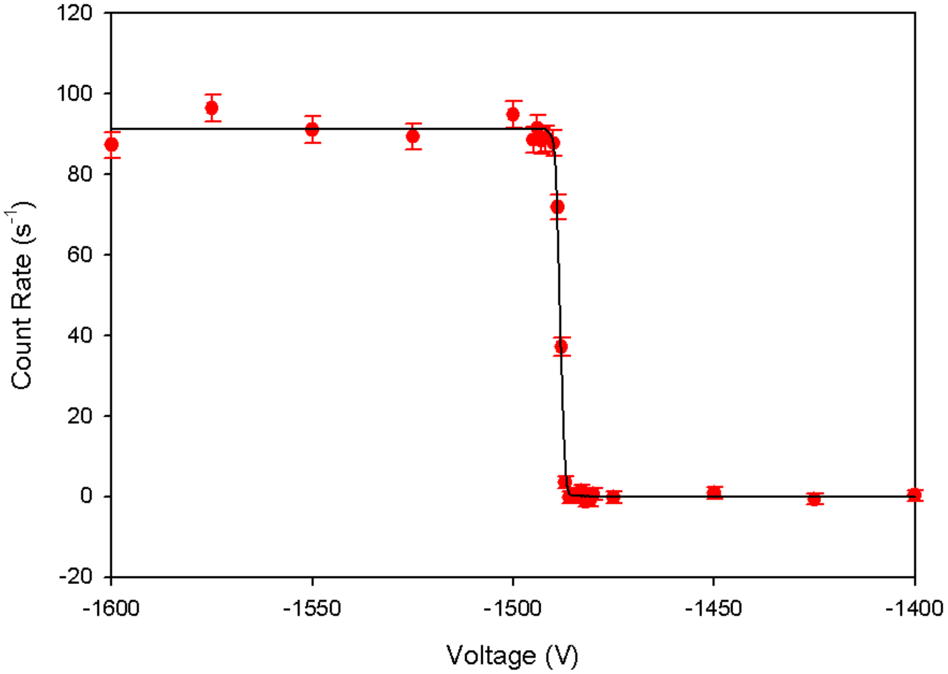

Fig. 5.10. Detected count rate vs. retarding potential for positrons emitted from a WMo moderator foil.

5.7 Slow Positron Remoderation Efficiency

The remoderation process increases the brightness of the positron beam, by decreasing the energy spread, at the expense of losing beam intensity due to annihilation in the foil. Brightness can be considered as the intensity of the positron beam normalized to the spot size and angular spread of the incident beam. A large diameter beam with large angular spread would have a low brightness and would indicate a lower quality beam. By remoderating the positrons, the angular and energy spread which the positrons obtain via the initial focusing is reduced to that of the reemitted positrons from the remoderator. As presented in the introduction, positrons are reemitted nearly normally to the surface with an energy spread about the work function of the remoderator. This reduction in the energy and angular spread increases the brightness.

This remoderation efficiency can be determined by measuring the detected count rate with the moderator extracted from the beam line and in place. When extracted, the full beam is able to reach the end of the spectrometer. A 100 second count was taken, with both in-core moderator banks operating, and the resulting count rate was 4571.2±6.8 s^{-1}. The moderator was then moved into the beam line and a new 100 second count was taken, resulting in a count rate of 190.7±1.4 s^{-1}, when the implantation energy was approximately 2500 keV. Because the remoderator foil was slightly smaller than the aperture within the moderator holder, a correction must be made for primary positrons entering the spectrometer through small gaps at the edges of the foil. This was achieved by performing one additional count where potential on the extraction grid was increased by +100 V, relative to the moderator potential. Because the potential placed on the moderator was more negative than the extraction grid and the energy of the slow positrons emitted from the grid was on the order of a few eV, remoderated positrons were repelled by the extraction grid back into the moderator. The resulting count rate consisted of primary positrons which are able to bypass the remoderator foil. Because their kinetic energy is approximately 1 keV, and all the potentials in the beam are negative, these positrons are not prevented from reaching the target by this retarding potential. The difference between the “beam on” count rate and “beam off” count rate is the number of slow positrons produced by the foil, which was determined to be 162.3±1.5 s^{-1}. The ratio of the detected slow positron rate emitted from the foil to the rate of the primary positron beam through the aperture before the moderator is taken as the efficiency of the moderator to produce slow positrons, which is determined to be 3.55±0.03%.

One method to increase the intensity of the positrons reaching the target is to increase the moderation efficiency of the transmission remoderator. The current moderation efficiency has been measured as 3.55±0.03% for a 190 nm WMo (10 nm W and 180 nm Mo) foil with an implantation energy of 2.5 kV. Moderation efficiencies as high as 17% have been reported for 100 nm WMo foils by Jørgensen et al. with an implantation energy of 3 kV. [60]

By annealing the moderator foil for a longer duration, more of the nonequilibrium defects can be removed from the foil, therefore removing defects which can acts as trapping sites for the slow positrons. For testing, the moderator was flash annealed to a white hot temperature four times, each flash lasting only seconds. In total, the moderator may have been at a white hot temperature for 20 seconds. The reason for this was to minimize to possibility of melting the moderator holder or damaging the foil. Rather than annealing the moderator for one long duration, more annealing flashes can be performed. Each flash would remove more of the non-equilibrium defects. Care should be taken to prevent the thin tungsten layer from diffusing into the bulk of the Mo layer, although the melting point of the W is higher than that of Mo so this should not be a major concern.

The 17% moderation efficiency quoted previously was for positron implantation energy of 3 keV, but the foil analyzed was only 100 nm thick. Because the foil used has a Mo layer twice as thick, the kinetic energy of the slow positrons can be increase to allow them to implant deeper into the foil. This would allow the more of the incident beam to reach the opposite face of the foil for reemission.

5.8 Time-of-Flight electronics

The timing setup for the pulsed positron spectrometer is the same as that for the bulk fast-fast coincidences setup, except the stop signal, which is produced by the detection of a 1.27 MeV gamma ray for the bulk setup, is generated by the pulsing electronics of the spectrometer.

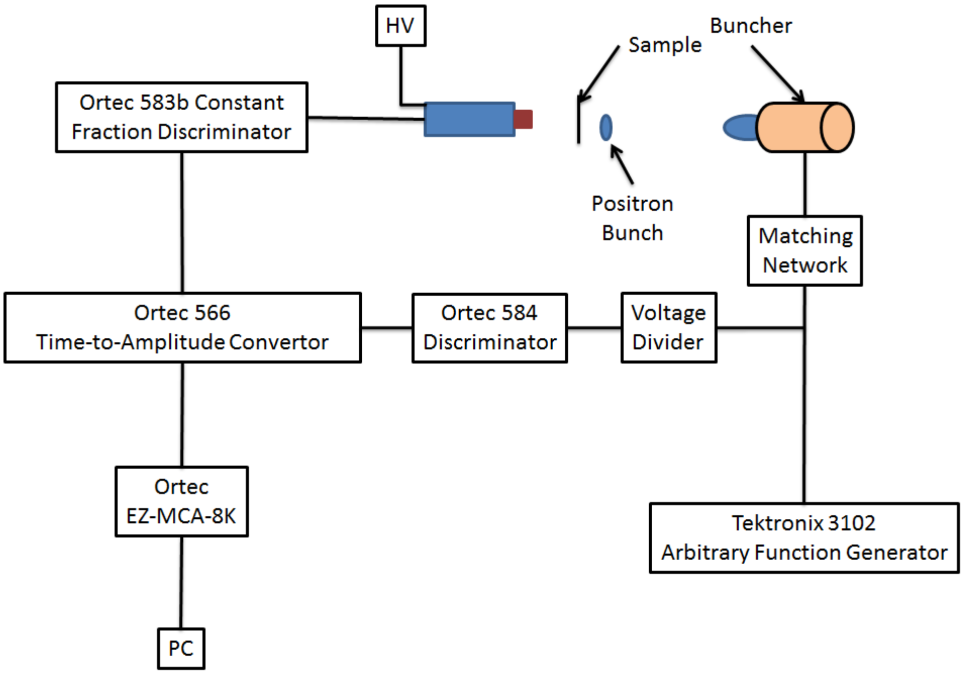

Fig. 5.11. Flow diagram of the setup of the timing electronics of the pulsed positrons spectrometer.

To trigger the timing process, pulses generated by the scintillation detector are analyzed by an Ortec 583B Constant Fraction Discriminator. [68] As the name suggests, this discriminator uses the constant fraction technique to determine the pickoff time of the input pulse. In this method, the discriminator produces an output pulse a fixed time after the leading edge of the pulse reaches some desired constant height of the final peak height. The advantage of this method is the pickoff time of the input pulse is almost independent from the amplitude, for pulses with similar shape but different amplitudes, reducing the effect of amplitude jitter on the timing properties. For constant fraction timing, the input pulse to the discriminator is attenuated to some desired fraction of the final pulse height in addition to being inverted and delayed. The attenuated and delayed pulses are then summed, resulting in a bipolar pulse with a zero crossover which occurs and the point in time where the pulse height crosses the desired constant fraction. [65] The Ortec 583B discriminator also includes a single channel analyzer which allows the flexibility of setting energy windows around the 511 keV pulse height, resulting in a decrease in background counts. By narrowing on the 511 keV annihilation pulse, the range of acceptable pulses is reduced, further reducing the effect of amplitude jitter on the time resolution.

As mentioned previously, the signal generated by the arbitrary function generator is used as the second logic signal for the TAC. The waveform supplied by the AFG is sent to a voltage divider, which is designed to reduce the amplitude of the waveform by a factor of approximately 10. The voltage divider is simply a 470 Ω resistor in series with the signal path, with a 47 Ω resistor shunted to ground.

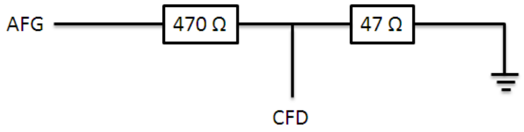

Fig. 5.12. Wire diagram for the voltage divider used to decrease the amplitude of the sine wave sent to the discriminator used to produce a stop signal for the TAC.

Because the signal path is parallel to the 47 Ω resistor, the same potential drop is seen in both. The signal is reduced by a factor of 10 because of the 470 Ω resistor in series. The attenuated signal is then sent to an Ortec 584 constant fraction threshold discriminator to yield the second fast logic pulse for the TAC.

An Ortec 566 Time-to-Amplitude convertor is used to determine the time interval separating the arrival times of pulses to the start and stop channels. The TAC operates as a start-stop type, where the arrival of a suitable start signal triggers the charging of a capacitor by a constant current source. The arrival of a stop pulse terminates the current source, therefore stopping the charging of the capacitor. The stored charge is therefore proportional to the time difference separating the pulses. The advantage of this method is the high linearity of the output to the input interval. [65] The detection of the 511 keV gamma ray supplies the start signal for the TAC, with the stop signal produced by the arbitrary function generator. This technique is recommended by the manufacturer due to the large number of pulses generated by the AFG because it reduces the amount of dead time occurring in the TAC. [69]

5.9 Optimization of the Drift Potential

The previous chapter demonstrated that the relationship between the focal length, particle velocity and amplitude of the applied waveform can be determined with consideration of the conservation of charge,

$$V^{3/2} = \frac{\omega V_o L}{\sqrt{\frac{8e}{m}}} \qquad 5.8$$

To test the effectiveness of the buncher, a 50 MHz, 286 V_{p-p}, sine wave was applied to the bunching electrode. The voltage applied to the drift electrode, which connects the buncher to the target, was varied and the resulting spectra were examined. The results of this scan can be seen in fig. 5.13. Each time spectrum is normalized to the average background level.

Equation 5.8 demonstrates that as the drift potential decreases, the focal length decreases. This results in overbunching of the beam which manifests as the characteristic double-peaked time spectra. This double-peak is due to positrons passing each other prior to reaching the target because the focal length is now closer to the buncher than the target.

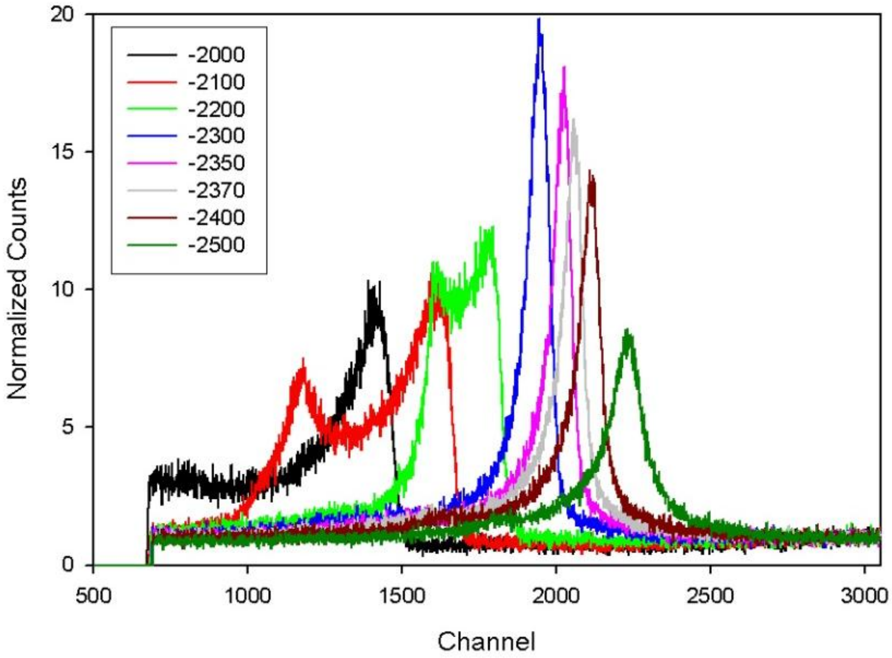

Fig. 5.13. Results displaying the effect of the drift potential bias on the time resolution.

As the drift potential increases, the focal length moves farther downstream away from the target, meaning the positrons are not able to reach the optimum time resolution. The time resolution with the highest peak results in the optimum time resolution because this value corresponds to the greatest number of positrons focused into the smallest time interval. The optimum voltage was found to be -2300V, with respect to ground. The kinetic energy of the positrons was approximately 800 eV.

5.10 Optimization of the Bunch Potential

For double gap harmonic bunching to be successful, the positrons must arrive at the entrance and exit acceleration gaps in phase with the applied waveform. The potential applied to the bunching electrode must be optimized so positrons gain the proper kinetic energy to arrive in phase with the rf potential. The results of this scan can be seen in fig. 5.14. As before, the time spectra are normalized to average constant background to account for possible fluctuations in the count rate.

When the potential applied to the buncher was -2300 V with respect to ground, the maximum peak in the time resolution was achieved. This implied that the positrons were in phase with the applied waveform.

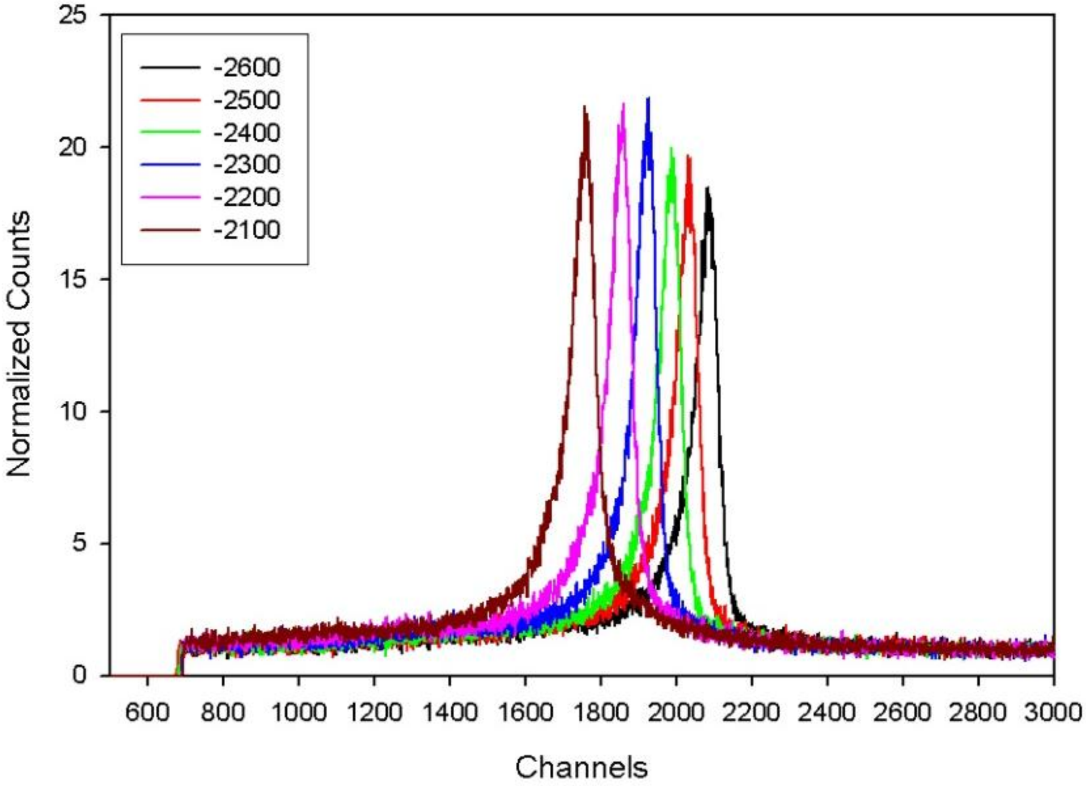

Fig. 5.14. Time spectra collected with varying the potential applied to the bunching electrode.

5.11 PALSFit Analysis of Lifetime Spectra

To extract the spectrometer time resolution from the timing spectra, the nonlinear least squares fitting program known as PALSfit is used. The program fits a measured spectrum to a model which consists of the sum of decaying exponentials convoluted with a resolution function and constant background. As mentioned in the introduction, the resolution function can be attributed to the experimental setup. The program attempts to iteratively minimize the difference between the data and a model which consists of *k* fitting parameters (b_i):

$$\Phi = \Sigma_{i=1}^{n} \omega_i \left(y_i - f_i \left(b_1, \ldots, b_k \right) \right)^2 \qquad 5.9$$

where y_i is the data point and $f_i(b_1 \ldots, b_k)$ is the value produced by a function which consists of *k* parameters of *b*. The value ω_i is a statistical weighting parameter:

$$\omega_i = \frac{1}{\sigma_i^2} \qquad 5.10$$

where σ_i^2 is the estimated variance of y_i, assuming Poisson statistics. The model's fitting parameters, b_i, are estimated and the calculation is iterated to minimize Φ. [78]

The optimum resolution fit occurred when using two Gaussians with intensities of 90% and 10%, which have approximately the same value. The Gaussian with a 90% intensity is taken to be the spectrometer time resolution. Directly in front of the sample is a grid with 90% transmission efficiency. The two Gaussians are attributed to annihilation with the grid and target, where approximately 10% of the annihilations occur in the grid and the remaining reach the target. The time resolution of the 90% component was found to be 277 ps.

As can be seen in fig. 5.14, possess an exponential tail which has a long lifetime component in excess of 1 ns. This should not occur in metals, where lifetimes are on the order of 100's of picoseconds.

5.12 Effect of Chopping the Beam

In an effort to remove the long lifetime component appearing in the lifetime spectra, an attempt was made to chop the incoming beam. To accomplish this, the second channel of the AFG is used to supply a 50 MHz, 10 $V_{p\text{-}p}$ square wave to the moderator. This channel was split to supply the time-varying chopping waveform to the moderator and supply the stop signal for the TAC. The voltage supplied to the extraction grid was slightly more positive relative to the voltage supplied to the moderator, meaning all the slow positrons emitted from the moderator are repelled from entering the spectrometer and attracted back to the moderator surface. With the application of the square waveform to the moderator, the magnitude of the applied voltage is periodically decreased to less than that of the extraction grid (keeping in mind that the potentials are negative), meaning during this time interval, slow positrons emitted from the moderator are able to proceed down the spectrometer. The remaining positrons are attracted to the moderator, chopping the beam.

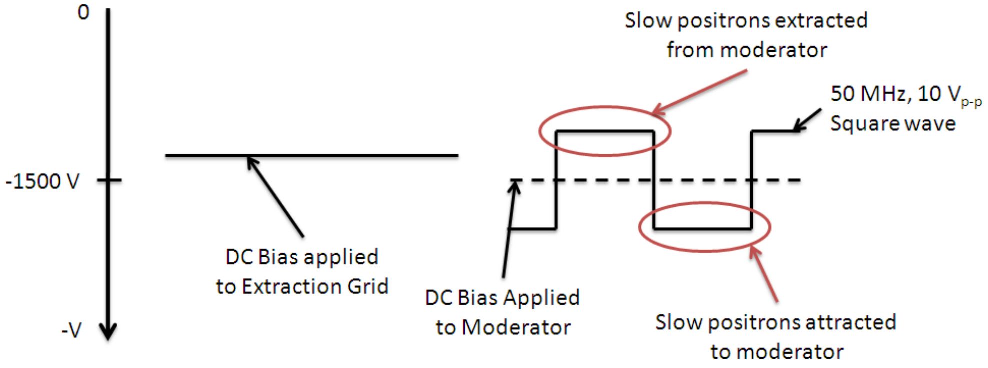

Fig. 5.15. Illustration displaying the potential differences which are used in chopping the DC positron beam.

To be successful, the slow positrons generated by the chopper must arrive at the first acceleration gap of the buncher in phase with the applied sine wave. Because a single AFG supplies waveforms for both the buncher and the chopper, changing the phase of the chopping waveform channel to that of the buncher channel will alter what portion of the DC beam is sent to the spectrometer therefore altering the arrival time of positrons to the buncher. This phase must be optimized by taking multiple short time spectra while varying the phase shift of the chopping waveform. The results of this optimization can be seen in fig.

5.16. The optimum phase shift between the two channels occurs when the peak height of the spectra is at its maximum. This is because the bulk of the positrons produced by the chopper are bunched into the final peak. When not in phase, positrons are scattered into the background. The optimum phase shift for the chopping waveform occurs at -100° relative to the bunching waveform.

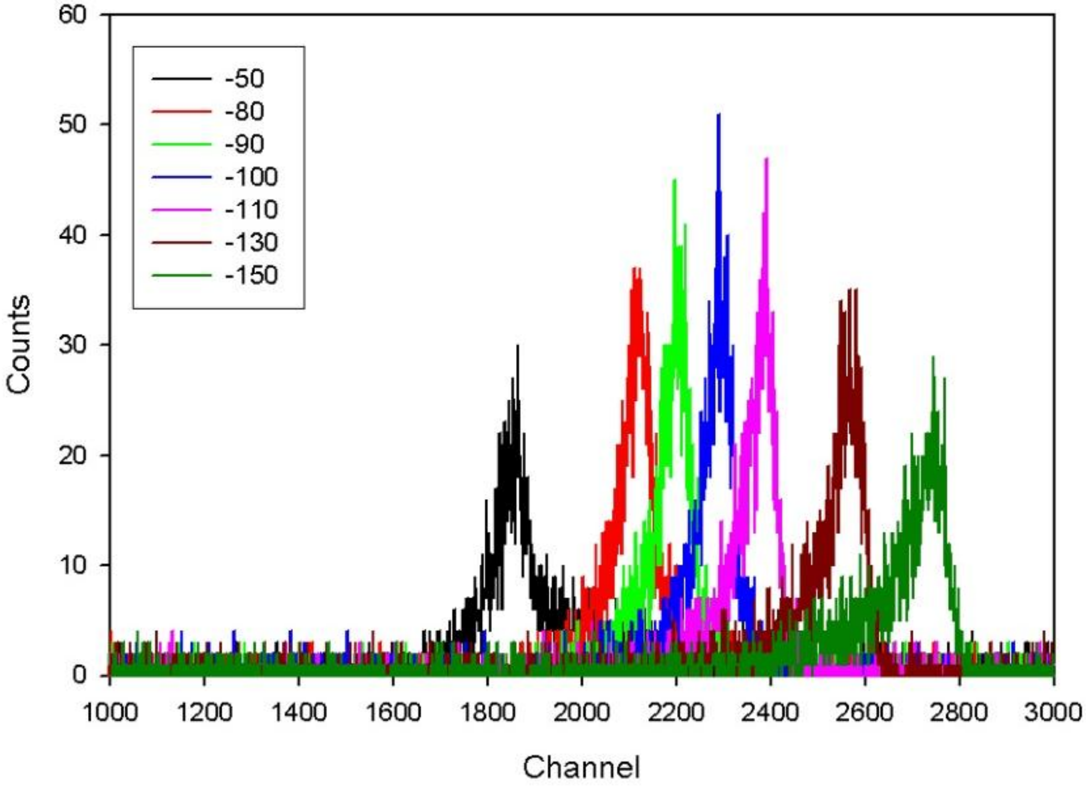

Fig. 5.16. Results of a scan through the phase shift between the bunching and chopping waveform.

With the optimum phase shift determined, a new time spectrum was collected using the optimum settings. This spectrum, along with a spectrum collected with a DC beam, can be seen in fig. 5.17. Each spectrum has been normalized to 1 and plotted on a log-lin plot so comparisons can be made between the two measurements. As can be seen, the long lifetime component does not appear in the chopped beam. Also, the peak-to-background increases from approximately 14:1 for the DC beam to approximately 46:1 for the chopped beam.

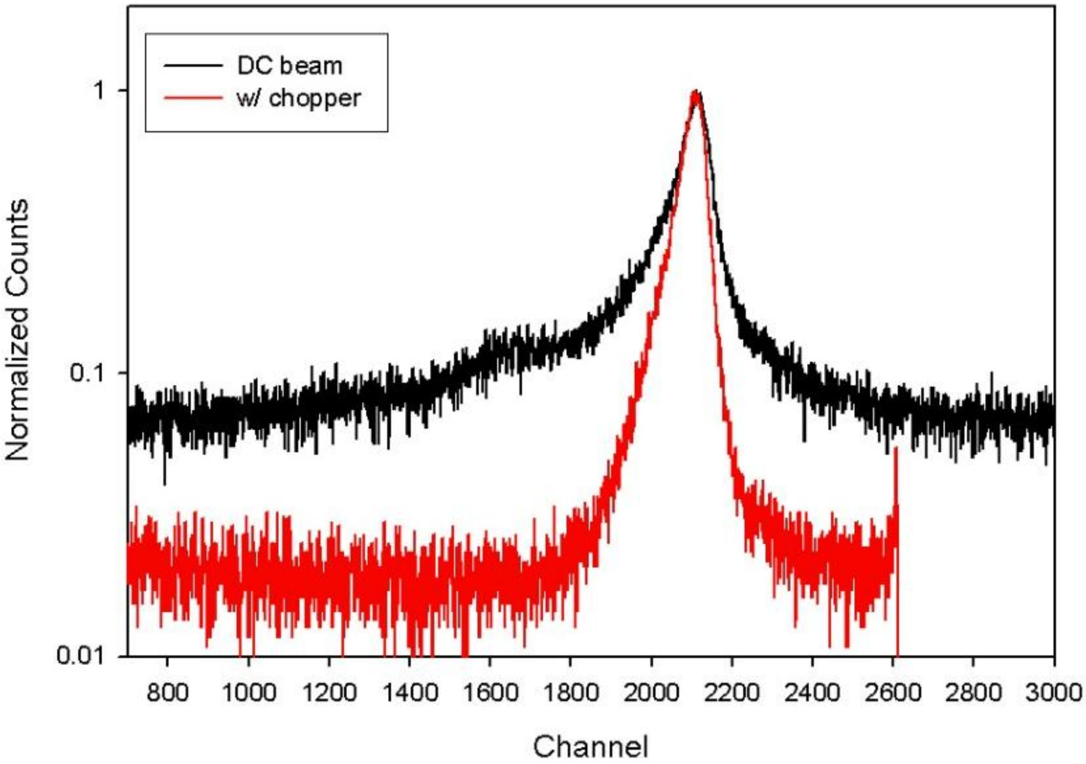

Fig. 5.17. Comparison between the time spectra collected when a DC beam is supplied to the buncher and a chopped beam is supplied to the moderator.

5.13 Final Performance

At the time of testing, the primary moderator banks had approximately 1000 hours of full power operation, leading to a decrease in the intensity, down to approximately 1x10^8 slow positrons per second (with both primary moderators functioning). Also, an intermittent short decreased the primary source intensity approximately in half. Because of these losses, the measured count rate of the pulsed positron beam was 60 counts per second, with both primary moderators functioning. When considering the detection efficiency, this corresponds to an on sample intensity of 1.2x10^5 slow positrons per second within the slow positron pulse. The loss in intensity from the primary beam is attributed to the low moderation efficiency (3.6%), passing the positron beam through a 1 cm aperture (~90% loss) and chopping the primary beam down to a 6 ns pulse from a continuous DC beam.

With regular maintenance, it is expected that a primary beam intensity of $1\text{x}10^9$ s^{-1} is achievable. This will increase the on target intensity to $1.2\text{x}10^6$ s^{-1}. Assuming the moderation efficiency of the transmission remoderator can be increased by a factor of 2, a conservative estimate, by better annealing and increasing the implantation efficiency, the on target intensity would increase to $2.4\text{x}10^6$ slow positrons per second. With consideration of the enhanced detection efficiency of a factor of 4.2 due to repositioning the target, the on sample event rate is expected to approach 5040 s^{-1}, assuming a primary source intensity of $1\text{x}10^9$ s^{-1}. This would allow a $1\text{x}10^6$ event time spectra to be collected in just over 3.25 minutes. In addition to the improvements to the performance of the beam, the NC State University PULSTAR reactor will undergo a power uprate from 1-MW to 2-MW. Because the slow positron intensity scales linearly with reactor power, the doubling in reactor power would increase intensity by a factor of 2. This would lead to an on sample intensity of $4.8\text{x}10^6$ s^{-1}, with an expected count rate of 10080 s^{-1}. A $1\text{x}10^6$ event time spectra could then be collected in 100 seconds.

Multiple positron groups have developed pulsed slow positron beams for lifetime measurements. The Electrotechnical Laboratory in Japan constructed a pulsed slow positron beam using a three grid chopper, a subharmonic prebuncher and a 150 MHz main buncher. This buncher produces a time resolution of ~100 ps and the pulse period can range from 25 ns to 10 ms because of the three grid chopper design. Because positrons are produced using a LINAC, reflected positrons can be stored in a storage ring, rather than being lost. [54]

The Munich group developed a pulsed slow positron beam with a time resolution of 150 ps (FWHM), with an overall time resolution of 240 ps. The pulsing system operates at a frequency of 50 MHz and consists of two rf bunching stages and a chopping stage. The first bunching stage uses a periodic ramp potential to increase the utilization of the primary beam by the main buncher, with an efficiency approaching 65%. [55-57]

Table 5-1. Performance comparison between pulsed positron beams at intense sources.

	FRM-II	**AIST**	**NCSU (Final Performance)**
Event Rate	**$1.5x10^{4}$**	**$>4x10^{3}$**	**$2.5x10^{3}$ [d] ($5.0x10^{3}$)[e] ($1.0x10^{4}$)[f]**
Time Resolution	**240 ps**	**~ 223 ps**	**277 ps**
Time Window	**20 ns**	**25ns – 1µs**	**20 ns**
Spot Size	**2 mm**	**30-100 µm**	**10 mm**
Beam Energy	**22 keV**	**30 keV**	**27 keV**

The Munich group's slow positron beam is located at the 20 MW FRM-II reactor. Slow positrons are produced by pair-production using gamma rays generated by thermal neutron capture reactions in a Cadmium shroud. [71] The calculated thermal neutron flux at the location of the positron converter is $2x10^{14}$ $cm^{-2}s^{-1}$, with a capture rate in the cadmium shroud of $1.2x10^{13}$ $cm^{-2}s^{-1}$. [74] The 9.041 MeV neutron binding energy of the Cd-113 isotope is released on average by 2.3 photons per neutron [7], meaning the photon flux in excess of the pair production threshold passing through the converter is estimated to be in approximately of $2.76x10^{13}$ $cm^{-2}s^{-1}$. For the PULSTAR Reactor, the photon flux in excess of

---

[d] Assuming a primary slow e^{+} beam intensity of $5x10^{8}$ s^{-1}.
[e] Assuming a primary slow e^{+} beam intensity of $1x10^{9}$ s^{-1}.
[f] Assuming an uprate in the PULSTAR power level to 2 MW (primary beam intensity of $2x10^{9}$ s^{-1}).

the pair production threshold passing through the moderator bank closes to the reactor core is calculated to be 3.07x10^{12} cm^{-2}s^{-1}, an order of magnitude less. Additionally, the material chosen to act as the moderator/convertor material for the FRM-II slow positron beam is Platinum, rather than Tungsten. Because Platinum has a higher atomic number, the pair production cross section is larger by approximately 11%. [74] With the upgrade in the PULSTAR's power level to 2 MW, occurring in the near future, and fresh moderators, it is possible for the detected event rate to be comparable to that produced by the pulsed positron beam located at FRM-II, although the power level would be 10 times smaller than that produced at FRM-II. Also, with the use of the grid chopper design to initially chop the beam, with the proper tuning, it is possible to easily increase the measurement time window, allowing the measurement of longer lifetime materials.

The pulsed positron beam located at AIST is used to generate a microprobe, so it has an on sample spot size ranging from 100-30 μm and the slow positrons are generated by a LINAC. A 70 MeV electron beam is injected onto a tantalum converter, generating fast positrons which are moderated with Tungsten thin films. The slow positron intensity is 2-3x10^{7} s^{-1}, but the spot size of the primary beam is approximately 10 mm. The high spatial resolution is produced with the utilization of two magnetic lenses, in addition to aiding in producing a beam with a higher time resolution. The high time resolution is produced by a 165 MHz resonant cavity. Because of the high frequency used, multiple stages of prebunching are required to time focus positron pulses to a suitable width to generate the high time resolution pulse by the 165 MHz cavity. [75] Initial raw positron pulses must be chopped and time focused by a prebuncher and buncher prior to reaching the final acceleration gap, which leads to complexity to the bunching system. Because the pulsed positron beam implemented at NC State operates on a 50 MHz double gap harmonic buncher, a suitable pulse width can be achieved using simpler electronics. Because it is a double gap harmonic buncher, the positrons experience two sections of velocity modulation, therefore the required power needed to generate the pulse is less than the resonant cavity used to generate the high resolution pulses at AIST. In addition, because both use a grid to provide a longitudinal field for chopping the beam, the repetition rate of the beam can be modified to allow for the measurement of longer lifetime components, to extend the use to the measurement of long lifetime defects.

Chapter 6 Conclusions and Future Work

6.1 Conclusions

The goal of this work was the development of a high intensity slow positron beam which can be used to provide positrons to two lifetime spectrometers and the development of a variable energy pulsed slow positron annihilation lifetime spectrometer (e^+-PALS) able to characterize defects in metals and semiconductors. The development of the high intensity slow positron beam proved to be a success, producing a beam which reached an intensity in excess of 10^9 s^{-1}. The beam stabilized at a nominal intensity of $5x10^8$ s^{-1}, due to contaminants in the vacuum altering the condition of the surface, with a beam diameter of approximately 30 mm. In addition, the beam switchyard design was successful in efficiently guiding positrons to either of the slow positron spectrometers as needed.

Implementation of the variable energy pulsed slow positron beam (e^+-PALS spectrometer) used to study metals and defects has also been successful. The current time resolution has been shown to be 277 ps, which is the quadrature sum of the detector resolution and pulse width. With fresh primary remoderators, the on sample intensity is expected to reach $1.2x10^6$ event rate.

6.2 Future Work

6.2.1 The Prebuncher

Prebunching of the positron beam could be accomplished by the use of a periodic ramp function applied to the transmission remoderator. Directly behind the moderator is a grid, which would produce a small region containing a time-varying electric field. Assuming a

50MHz ramp function with a peak to peak voltage of 7 V is used, the kinetic energy of the positrons can be calculated to obtain a specified focal length. The ideal periodic ramp function waveform is given by [33]:

$$V(t) = \frac{V_o t}{\left(\frac{1}{2 f_o} \right)} \quad \left(-\frac{1}{2 f_o} < t \le \frac{1}{2 f_o} \right) \tag{6.1}$$

where f_o is the frequency of the waveform and V_o is the peak-to-peak voltage. The derivative with respect to time would therefore be constant in this case:

$$\frac{dV(t)}{dt} = \frac{V_o}{\left(\frac{1}{2 f_o} \right)} \tag{6.2}$$

By inserting this into Eq.4.13, a relationship between the kinetic energy of the beam and the focal point can be determined:

$$L = \frac{E_o v_o}{e V_o f_o} \tag{6.3}$$

or

$$E^{3/2} = \frac{e V_o f_o L}{\sqrt{2/m}} \tag{6.4}$$

Because the kinetic energy of the positrons is simply equal to the product of the charge and applied potential, the voltage required for a given focal length is:

$$V_{\text{mod}}^{3/2} = \frac{V_o f_o L}{\sqrt{2e/m}} \tag{6.5}$$

Assuming a focal length of 1.2 m, the required voltage applied to the moderator would be approximately 50V. Because the positrons are emitted with an energy of approximately 2.8V, the required potential would therefore be 47.2V.

To test the effectiveness of the prebuncher, a user program was created for the ion optics simulation package SIMION. [39] The model consists of vertical grids within a grounded tube. The simulation consisted of 4100 particles emitted from a grid with an energy sampled from a Gaussian distribution with a FWHM of 0.4 eV [55] and a mean energy of 2.8 eV. The time of birth of the particle, which ranged from 0 to 20ns, determines the potential supplied to the grid. At a focal length of 1.2m, the time of flight and the kinetic energy of the positrons were recorded. A histogram of the time of flight data is presented in the fig. 6.1 below, with time bins of 100 ps.

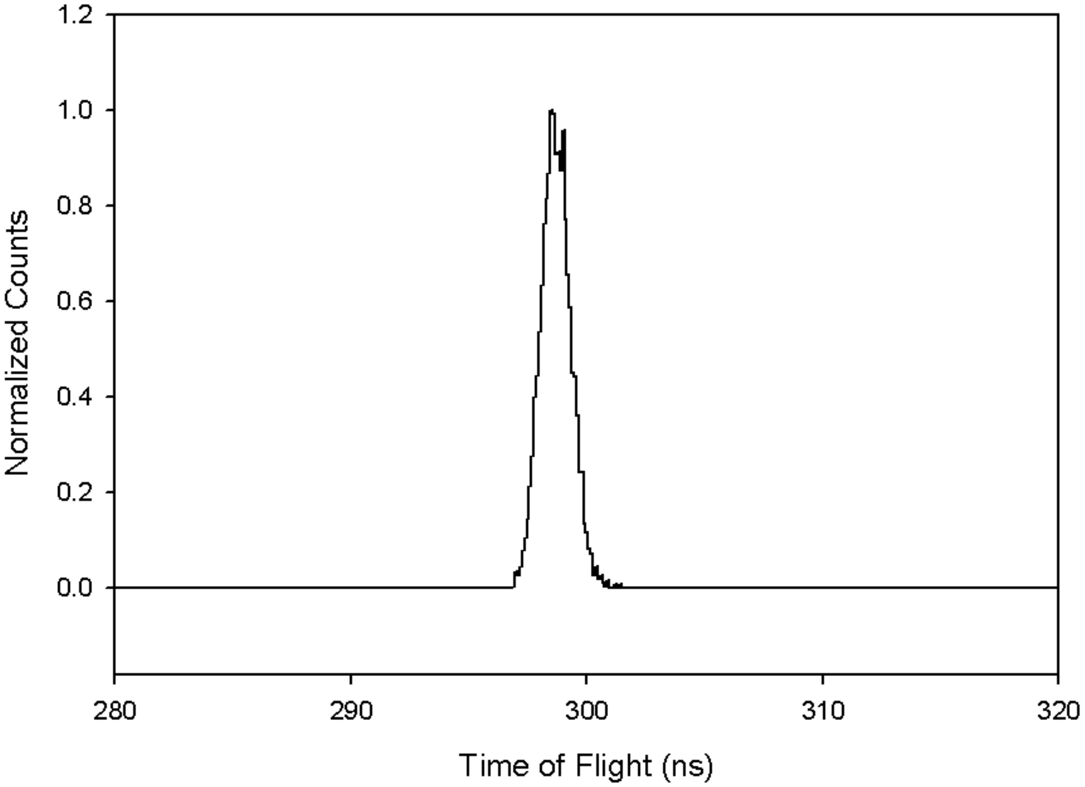

Fig. 6.1. Calculated time spectrum at the entrance of the buncher produced by a 7 V_{pp} ramp potential applied to the moderator.

This simulated time spread was found to be 1.4 ns (FWHM) with a corresponding energy spread of approximately 8 eV. If the prebuncher was able to compress 50 percent of the incident DC beam into the acceptance window of the buncher, the detected count rate should effectively double, to 10080 events per second, assuming a primary positron beam intensity of $1x10^9$ s^{-1}.

6.2.1.1 *The Buffer Amplifier*

The capacitance to ground of the prebuncher, including the coaxial lines supplying the signal, was found to be 167 pf. This capacitance yields an impedance of 19 Ω at 50 MHz. Because the output impedance of the arbitrary function generator used to supply the time-varying-potential is 50 Ω, there is an impedance mismatch between the source and load resulting in a degradation of the applied signal.

A unity gain buffer amplifier with lower output impedance than the waveform generator may be used to transfer the waveform with greater efficiency to the load. The amplifier used is an operational amplifier set up in a voltage follower circuit. Because of its large input impedance, very little current is drawn from the waveform generator, meaning there is little distortion to the source signal. Also, because of the small output impedance, the amplifier can supply current to the load with less degradation to the input signal. [62]

An Intersil high slew rate operational amplifier is used for the buffer amplifier. This amplifier had a slew rate of 7000 V/μs [63], which is sufficient to supply the desired bunching signal. This amplifier is attached to a copper clad circuit board, which acts as a common ground for all the components. A 1 amp, 24 V AC-DC power supply is used to supply voltage to the op-amp. A voltage divider is placed on the positive and negative supply leads to supply a +/- 10.9V to the positive and negative inputs of the amplifier. The slew rate of the amplifier increases with higher supply voltages. A 100 μf capacitor is placed in parallel with both the positive and negative supply voltage to act as a low pass filter, which keeps ripples in the supply voltage from reaching the amplifier. A 10 nf capacitor is also placed in parallel with the supply voltages to act as a higher frequency low pass filter, which prevents high frequency voltages from the amplifier from reaching the supply circuit.

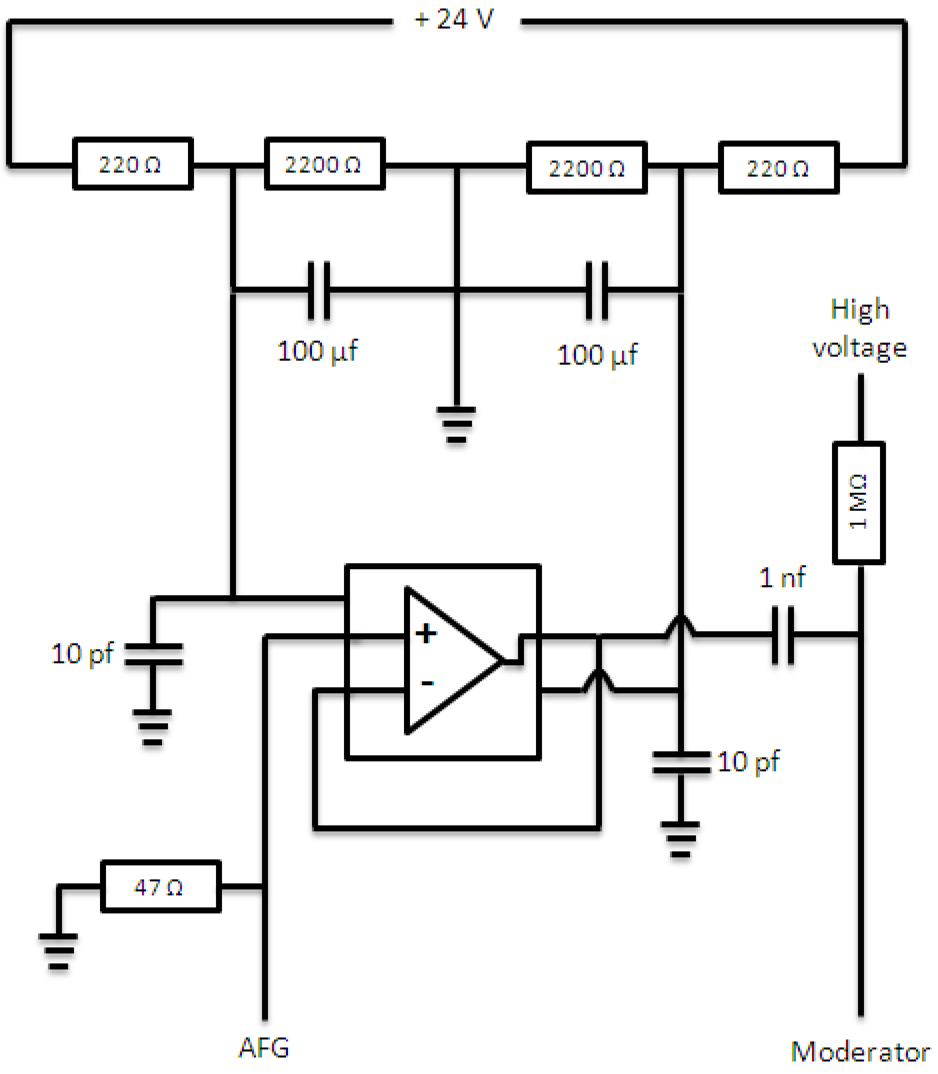

Fig. 6.2. Wire diagram for the buffer amplifier.

The signal from the AFG is fed to the amplifier through a bnc bulkhead connector. This bulkhead connects to the non-inverting input of the op-amp and is terminated with a 47Ω resistor in parallel to ground. The output of the amplifier is attached to the inverting input of the amplifier, to produce the unity gain voltage follower circuit, and capacitively coupled to the high voltage supply using a 1nf, 3 kV capacitor. This is then sent to an SHV bulkhead connector, where it can be fed to the moderator electrode. An image of the assembled buffer amplifier can be seen in fig. 6.3.

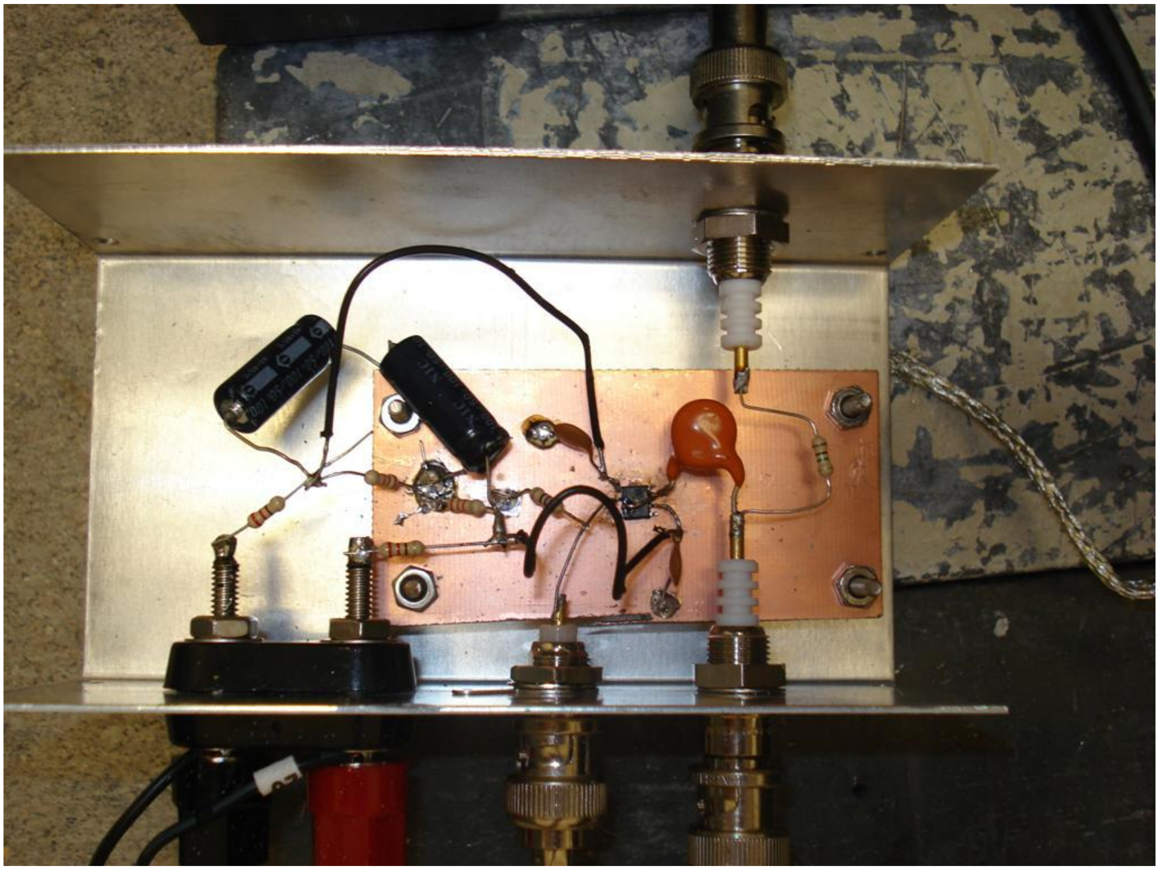

Fig. 6.3. Image of the assembled buffer amplifier. The copper circuit board acts as a common ground.

Further tests would need to be performed to determine the effectiveness of the buffer amplifier.

6.2.2 Magnetic Focusing

To focus more of the primary positron beam onto the transmission moderator, simulations have been performed to see if a magnetic lens can be utilized to focus the primary positron beam. In a design similar to that presented by Oshima *et. al*. [76], the proposed magnetic lens consists of a 12” in diameter coil surrounded by a 1cm thick soft iron yoke. The yoke would be constructed from multiple overlapping plates to provide a 12” in diameter, 1 cm thick, plate with a 4” aperture. This would be attached to the front of the magnetic coil, with the remainder of the coil enclosed 1 cm thick soft iron. The yoke would contain a 2 mm gap, resulting in an intense magnetic field over a short distance. This lens design was modeled in TriComp to test its effectiveness. Positrons were emitted within a solenoid with the initial simulated trajectories produced by the extraction optics simulation for the primary lenses of the positron beam.

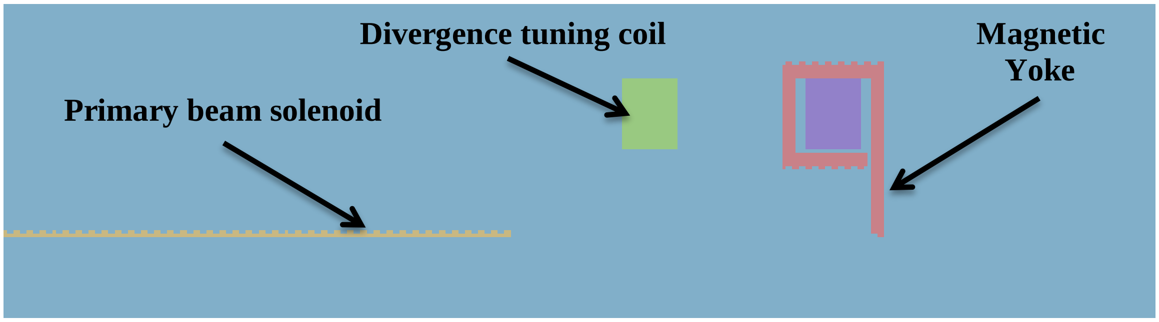

Fig. 6.4. A Tricomp model of a 4” ID solenoid followed by a magnetic lens.

An additional coil was placed between the end of the solenoid and magnetic lens so the divergence of the beam exiting the solenoid could be modified. Electrostatic lenses were also simulated so the simulated positrons could be accelerated.

Figure 6.5 presents the simulated magnitude of the magnetic field strength on the axis of the beam for both a 4 inch in diameter solenoid and a 4 inch solenoid with a magnetic lens placed approximately 9.75” away from the outlet of the solenoid. It should be emphasized that the graph presents the magnitude of the magnetic field. The current passing through the coil acting as the lens is in the opposite direction of the current flowing through the solenoid of the primary beam. Therefore, according to the simulation, if the current through the solenoid is 80G, the field produced by the lens is approximately -80G.

To test the effectiveness of the proposed focusing design, the position of positrons were recorded at various locations as they traversed the beamline. Positrons were emitted with starting positions, trajectories and kinetic energies determined by the electrostatic simulations of the extraction and focusing of positrons from the moderator banks. This was to ensure positrons used in the beam focusing simulation mimicked the behavior of the primary positron beam.

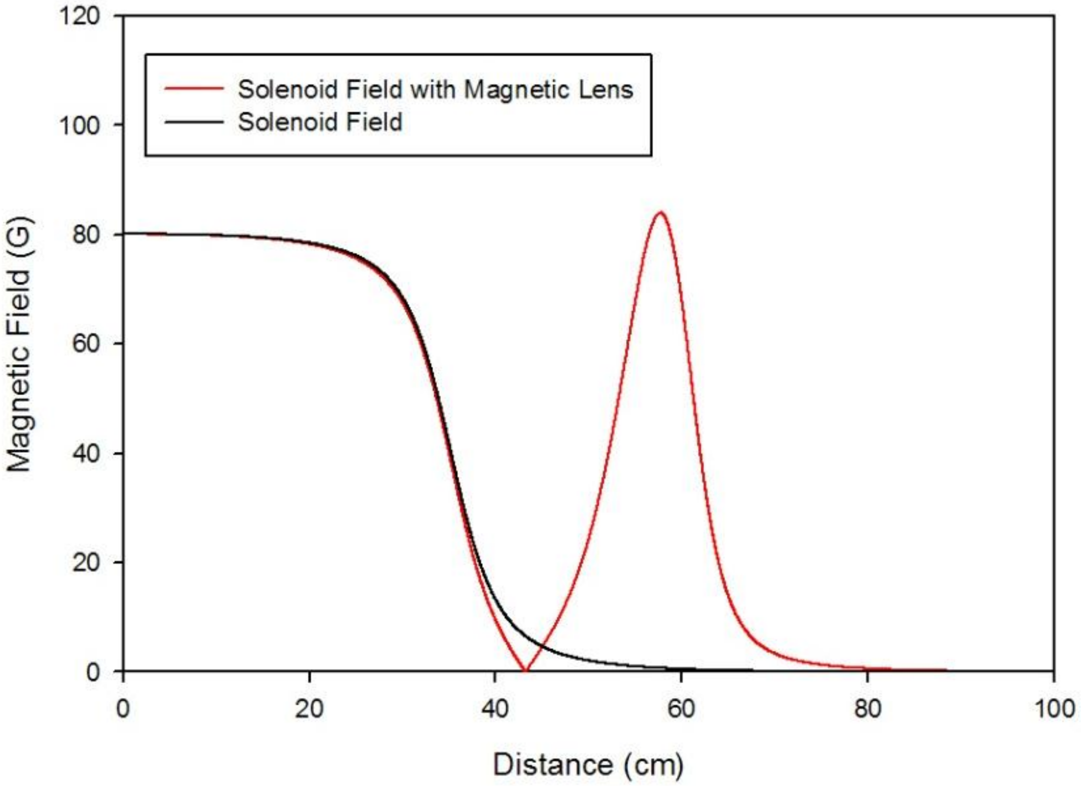

Fig. 6.5. Calculated magnitude of the axial magnetic field strength for the outlet of a solenoid (black) and solenoid followed by magnetic lens.

Figure 6.6 displays a contour plot of the primary positron beam within the primary beam's solenoid.

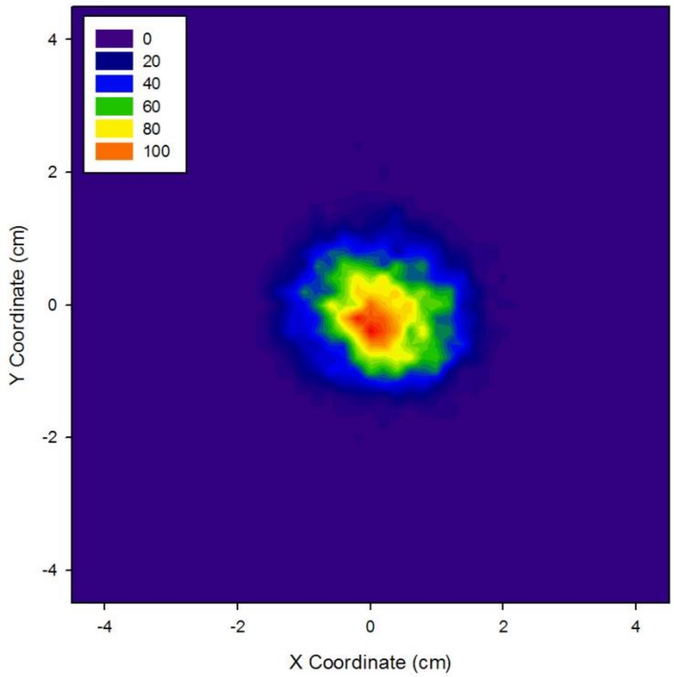

Fig. 6.6. Simulated beam profile for the primary positron beam.

The following is a contour plot of the positron beam approximately 7 cm away from the yoke of the magnetic lens.

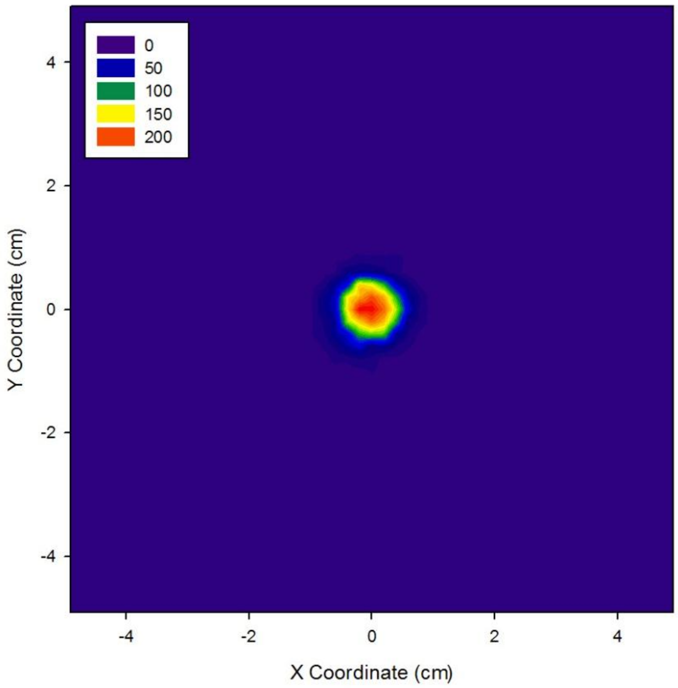

Fig. 6.7. Simulated beam profile of the primary positron beam 7 cm after a magnetic lens.

With some optimization of the current applied to the magnetic lens and extraction coil, and the kinetic energy of the positron beam, approximately 53% of the primary positron beam can be focused into a 1 cm aperture.

Because the magnetic lens focuses the positrons into a region of low axial magnetic field, further focusing can be performed to reduce the spotsize of positrons emitted from the remoderator foil into the spectrometer. To accomplish this, the magnetic coils of the spectrometer can be arranged so that they act as a magnetic funnel, meaning the positrons emitted from the remoderator foil follow the converging magnetic field of the magnetic gradient of the spectrometer's magnetic coils. The proposed design would consist of an extraction grid directly in front of the remoderator foil followed by two lenses. The first lens has a positive potential, relative to the extraction grid and second lens to ensure positrons do not collide with the walls of the focusing lenses.

TriComp was once again used to test the effectiveness of this proposed design. Positrons were emitted with an energy sampled from a 0.4 eV Gaussian distribution and a 10° Gaussian distribution for the initial trajectory.

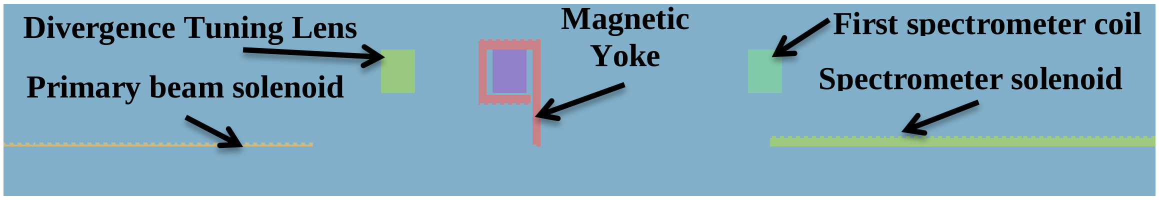

Fig. 6.8. A Tricomp simulation of the magnetic lens and additional coils off the spectrometer acting as a magnetic funnel.

The starting points for the emitted positrons were taken as the recorded positions from the focusing simulation at the focal point. A -100 V, relative to the remoderator foil (or emission plane for the simulation) was placed on the extraction grid and the second focusing lens, with -50 V on the first lens. This simulation indicated 93% of the positrons emitted from the remoderator foil could be further focused into a spotsize with a FWHM of approximately 3.2 mm.

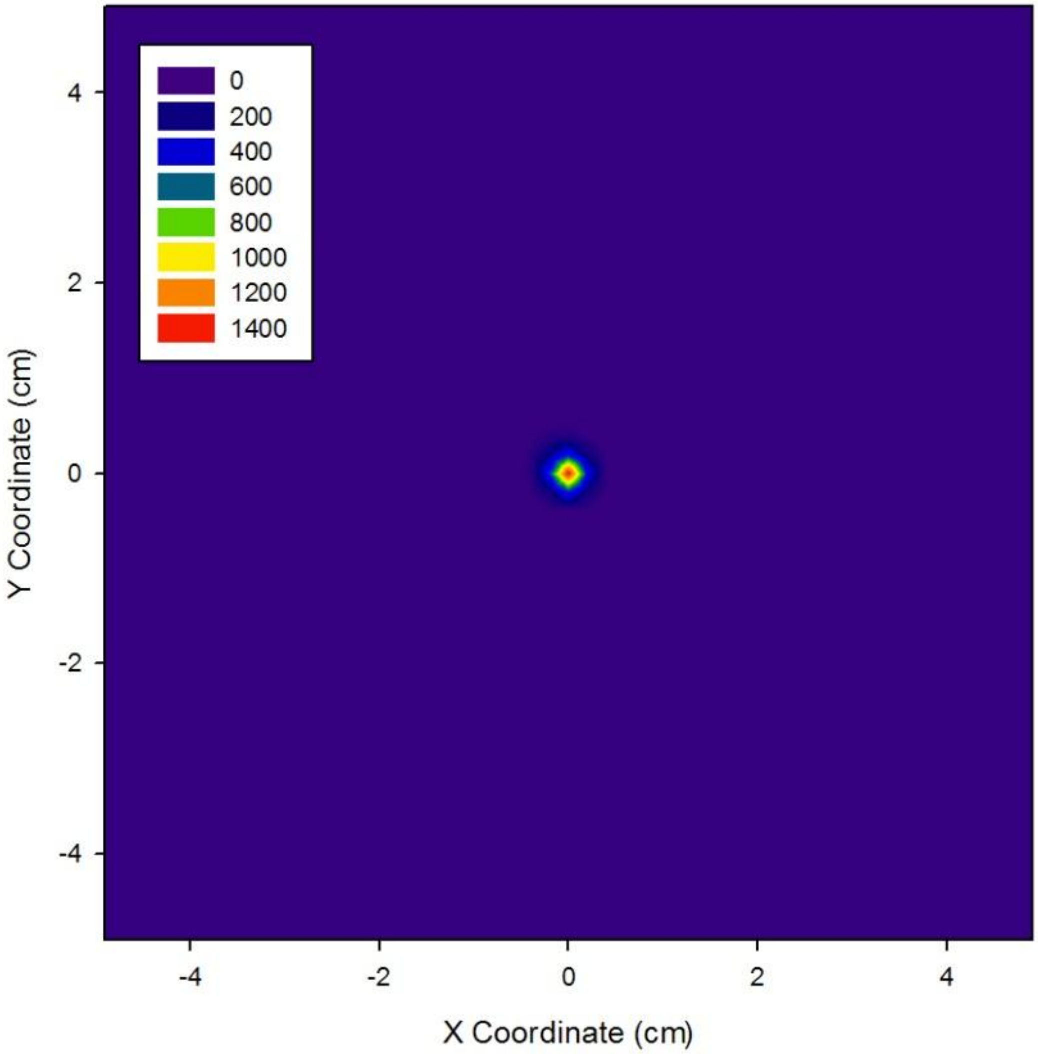

Fig. 6.9. Simulated beam profile of slow positrons emitted from a remoderator foil into a magnetic funnel. The FWHM of the profile is 3.2 mm.

Further simulations were conducted to ensure that the performance of the magnetic lens did not degrade with the additional coils of the spectrometer inserted into the simulation. The magnetic focusing simulation was again performed and 51% of the primary positrons can traverse a 1 cm aperture 7 cm away from the lens.

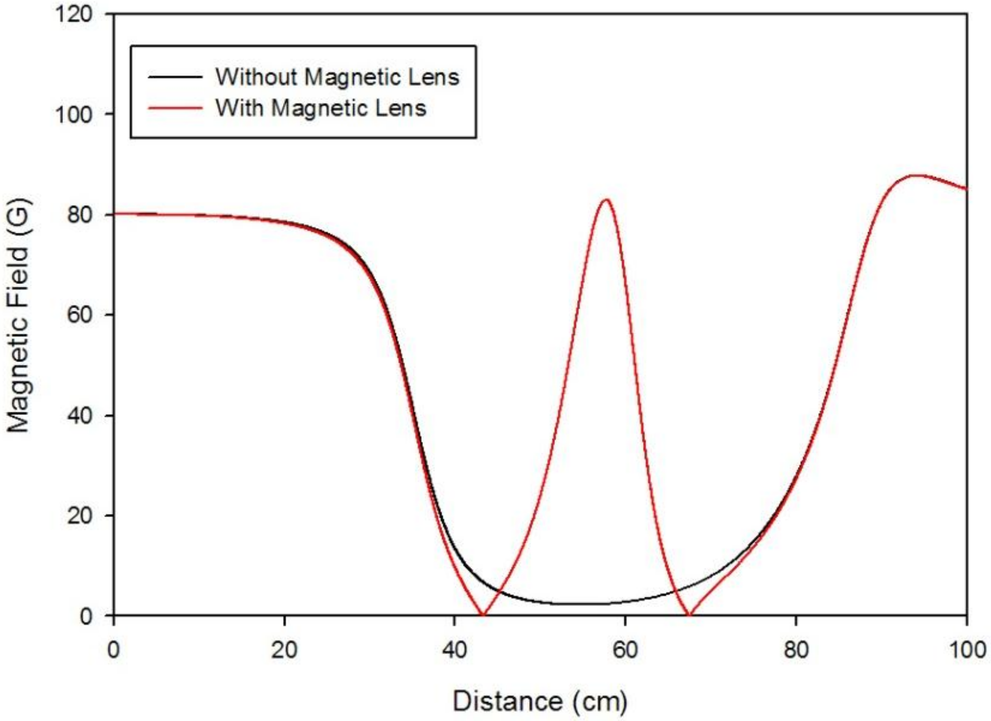

Fig. 6.10. Simulated axial field of the transmission to the spectrometer with and without a magnetic lens.

6.2.3 Load-Lock and Sample Holder

Currently, to replace the sample, the entire spectrometer must be brought to air. The introduction of air also results in atmospheric water vapor entering the spectrometer. This water vapor can then adsorb to the surface of the internal components and outgas during the pumping down of the spectrometer. This increases the time required to reduce to beam pressure to high vacuum conditions. One method to minimize the amount of water vapor introduced into the spectrometer is to backfill the spectrometer with dry nitrogen. The amount of atmospheric water vapor entering the spectrometer is therefore minimized. Because the nitrogen is mostly inert, it is easier to pump from the spectrometer.

An alternative approach to reducing the time taken to change samples is to install a load lock to the target chamber of the spectrometer. A load lock is a small chamber attached to the vacuum system, separated by a gate valve. Because of the small volume of the load-lock, the pressure can be quickly brought to high vacuum conditions. Once a suitable pressure is reached, the gate valve can be opened and the sample can be lowered into position.

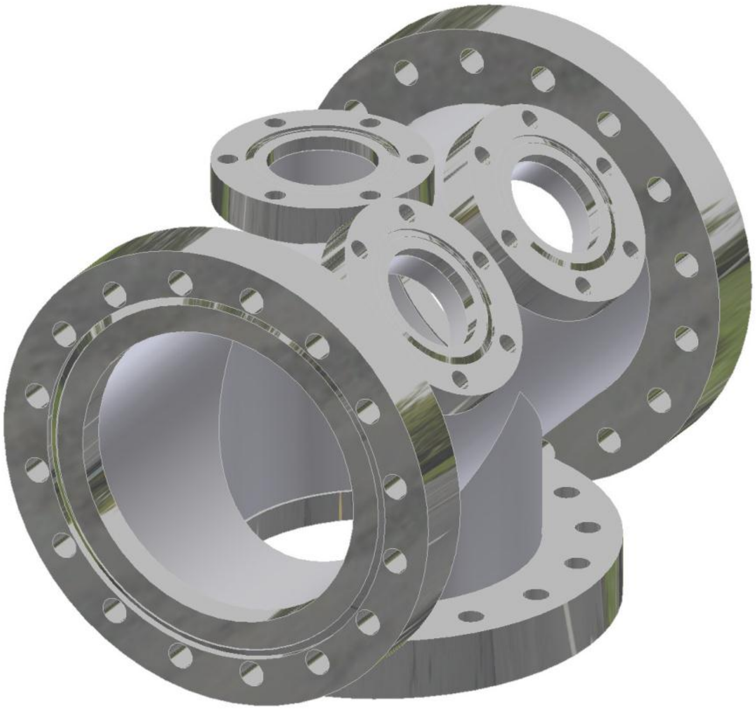

Fig. 6.11. Image of a proposed load-lock vacuum chamber design.

The volume of the proposed load-lock would be made as small as possible to minimize the amount of time required to lower the chambers pressure to a suitable pressure. A 6” conflat flange would be used to mount the chamber to a gate valve, to isolate the load-lock from the spectrometer. A 2.75” flange would be offset from the center of this mounting flange by 0.775” so a simple linear manipulator can be used to side the sample into place at the target position. Additional 2.75” flanges could be utilized as voltage feedthroughs and offer a location for measuring the pressure of the chamber. When necessary to open the load-lock to air, filling this chamber with dry nitrogen will minimize the amount of water vapor entering the load-lock, coupled with the small volume of the chamber; the pump-down time should be greatly improved.

Further improvements to the sample throughput can be made by fabricating a sample stalk which could hold multiple samples in a row. Once the analysis is performed on the first sample of the stalk, the holder could be lowered, introducing a new sample for analysis. The previously analyzed sample then simply lowers into the vacuum chamber support. An alternative stalk could also be utilized to allow resistive heating of the sample for the characterization of defects with respect to temperature.

6.2.4 Optimization of the Moderator Diameter

Currently, the diameter of the primary moderator banks are as large as can be achieved without the risk of shorting of the lenses to the vacuum chamber wall. This maximizes the amount of tungsten in the vicinity of the core in an attempt to generate the greatest slow positron intensity. A smaller moderator would in principle produce fewer slow positrons, but could possibly be focused into a smaller spot size, generating a beam with a better brightness. Because beam tube 6 which houses the positron beam forms a 37° angle to the face of the reactor core, if the primary moderators are made with a smaller diameter, they could be slid closer to the face of the core. The ability to place the moderators closer to the core where the photon flux is higher could make up for positrons lost because of the smaller moderators.

Multiple MCNP runs were performed with moderator banks of different diameters, ranging from 3” to 8.8”. In each simulation, the density supplied to MCNP is equal to that of a moderator composed of 0.25 mm thick tungsten strips forming a moderator 8.8” in diameter, 1” thick and the strips form an array of 1 cm cells, i.e. calculations assume that each moderator bank possesses the same surface area and mass as the 8.8” moderator used for the current positron beam. Therefore the effective volume for positron emission is the same for all cases.

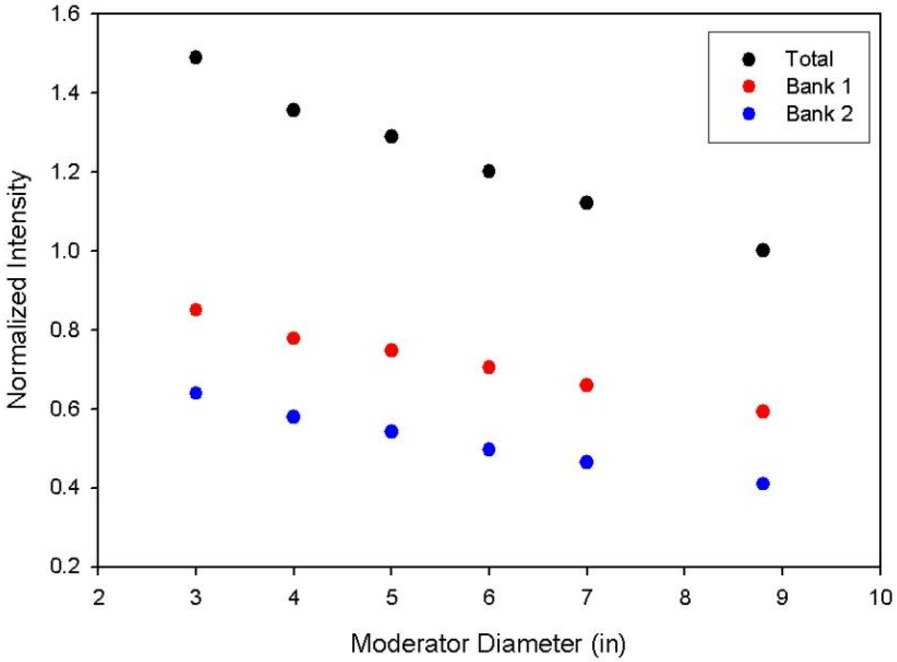

Fig. 6.12. MCNP simulation results for varying the diameter of the moderator banks while maintaining a constant vain thickness and surface area.

This calculation assumes that the volume of each moderator bank under consideration is equal. In addition, because of the thin thickness of the moderator strips which would be used (0.25 mm) the surface area of each moderator bank would be the same. These two conditions imply that the cross section of the cells of the moderator must decrease, which would lead to a reduction of the moderation efficiency. The true optimum in the moderator size would therefore be the point where the increase in positron production would be offset by the loss of positron extraction efficiency due to collisions with the walls of the smaller array cross section. A decrease in spot size could possibly be obtained because of better electrostatic focusing due to the smaller moderators.

References

[1] P.A.M. Dirac, Proc. Roy. Soc. London Ser. A. **126** (1930) 360.

[2] C.D. Anderson, Phys. Rev. **43** (1933) 491.

[3] J. Chadwick, P.M.S. Blackett, G.P.S. Occhialini, Proc. Roy. Soc. London Ser. A. **144** (1934) 235.

[4] Charlton, M. and Humberston, J.W., *Positron Physics*, New York: Cambridge University Press, 2001.

[5] E. Bellotti, M. Corti, E. Fiorini, C. Liguori, A. Pullia, A. Sarracino, P. Sverzellati, L. Zanotti, Phys. Lett. **124** (1983) 435.

[6] P.S. Schultz, K.G. Lynn, Rev. Modern Phys. **60** (1988) 701.

[7] Coleman, P. ed., *Positron Beams: and Their Applications*, New York: World Scientific, 2000.

[8] Krause-Rehberg, R. and H. Leipner, *Positron Annihilation in Semi-conductors: Defect Studies*, Berlin: Springer-Verlag, 1999.

[9] N.D. Lang, W. Kohn, Phys. Rev. B. **3** (1971) 1215.

[10] C.H. Hodges, M.J. Scott, Phys. Rev. B. **7** (1973) 73.

[11] F. Jacobsen, K. Lynn, Phys. Rev. Lett. **76** (1996) 4262.

[12] J.A. Baker, M. Touat, P.G. Coleman, J. Phys. C: Solid State Phys. **21** (1988) 4713.

[13] D. A. Fischer, K.G. Lynn, D.W. Gidley, Phys. Rev. B. **33** (1986) 4479.

[14] Krane, K., *Introductory Nuclear Physics*, New York: John Wiley & Sons, 1998.

[15] Tipler, P. and R. Llewellyn, *Modern Physics*, 4th ed., New York: W.H. Freeman and Company, 2003.

[16] D. Schödlbauer, P. Sperr, G. Kögel, W. Triftshäuser, Nucl. Instr. Meth. B. **34** (1988) 258.

[17] Faw, R.E.,and Shultis, J.K., *Radiological Assessment: Sources and Doses*, La Grange Park, IL, American Nuclear Society, Inc., 1999.

[18] Wollnik, H. *Optics of Charged Particles*, Orlando, Fl., Academic Press, Inc., 1987.

[19] Canter, K.F., "Slow Positron Optics", *Positron Spectroscopy of Solids (Spettroscopia Positronica dei Solidi)*, Burke, VA, IOS Press, Inc., 1995.

[20] Canter, K.F., Mills, A.P., Can. J. Phys. **60** (1982) 551.

[21] Fink, J., Schumacher, B., Nuc. Instr. Meth. **130** (1975) 252.

[22] Colmenares, C., Howell, R.H., Ancheta, D., Cowan, T., Hanafee, J., Sterne, P. (1996) *First Positron Annihilation Lifetime Measurement of Pu* (Lawrence Livermore National Laboratory Report, UCRL-ID-126003). Springfield, Va: National Technical Information Service, U.S. Department of Commerce.

[23] Williams, P., Ann. Rev. Mater. Sci. **15** (1985) 548.

[24] Omote, K., Ito, Y., Kawamura, S., App. Phys. Lett. **82** (2003) 544.

[25] Howell, Richard. Positron Facility, Lawrence Livermore National Lab. *Antimatter Helps to Protect Our Nuclear Stockpile.* https://www.llnl.gov/str/Howell.html.

[26] Glade, S. J. Nucl. Mat. **351** (2006) 197.

[27] Moscou, L., Lub, S., Powder Technology **1981** (1981) 45.

[28] Conner, W. Cevallos-Candau, J., Weist, E., Pajares, J., Mendioroz, S., Cortes. A., Langmuir **2** (1986**)** 151.

[29] Dombrowski, R., Hyduke, D., Lastoskie, C., Langmuir **16** (2000) 5041.

[30] Gidley, D.W., Peng, H., Vallery, R.S., Annu. Rev. Mater. Res. **36** (2006) 49.

[31] Krause-Rehberg, R., Bondarenko, V., Thiele, E., Klemm, R., Schell, N., Nucl. Instr. Meth. B. **240** (2005) 719.

[32] Bisi, A., Faini, G., Gatti, E., Zappa, L., Phys. Rev. Lett. **5** (1960) 59.

[33] Humphries, S., *Charged Particle Beams*, New York: John Wiley & Sons, Inc., 1990.

[34] *Nuclear Reactor Program: Specifications*. (2010) Retrieved November 7, 2010, from http://www.ne.ncsu.edu/nrp/images/history/PULspecs.pdf.

[35] *Nuclear Reactor Program: PULSTAR Reactor*. (2010) Retrieved November 7, 2010, from http://www.ne.ncsu.edu/nrp/pulstar.html.

[36] Hathaway, A. G. (2003) *Design and Testing of a Prototype Slow Positron Beam at the NC State University PULSTAR Reactor*. (Master's Thesis, North Carolina State University).

[37] X-5 Monte Carlo Team, "MCNP5—A General Monte Carlo N-Particle Transport Code, Version 5," Los Alamos National Laboratory, Los Alamos, NM, Tech. Rep. LA-UR-03-1987, 2003.

[38] van Veen, A., Schut, H., de Roode, J., Labohm, F., Falub, C.V., Eijt, S.W.H., Mijnarends, P.E., Mat. Sci. For. **363-365** (2001) 415.

[39] Dahl, D. A., *SIMION 3D Version 7.0 User's Manual*, Idaho Falls, ID, Idaho National Engineering and Environmental Laboratory, 2000.

[40] Weng, H.M., Ling, C.C., Hui, I.P., Beling, C.D., Fung, S., App. Surf. Sci. **194** (2002) 24.

[41] Lamarsh, J.R. and Baratta, A.J., *Introduction to Nuclear Engineering* (3rd ed.), Upper Saddle River, NJ: Prentice Hall, 2001.

[42] Moxom, J., Hathaway, A.G., Hawari, A.I., Out of Core Testing of the North Carolina State University PULSTAR Reactor Positron Beam. *2007 IEEE Nuclear Science Symposium Conference Record* (2343-2348).

[43] Jørgensen, L.V., Labohm, F., Schut, H., van Veen, A., J. Phys.: Condens. Matter **10** (1998) 8743.

[44] Moxom, J., Hathaway, A.G., Bodnaruk, E.W., Hawari, A.I., Xu, Ju., Nucl. Instru. Meth. A. **579** (2007) 534.

[45] *Field Precision*, P.O. Box 13595, Albuquerque, NM 87192, USA.

[46] Chen, F.F., *Introduction to Plasma Physics*, New York: Plenum Press, 1974.

[47] Larson, R., Hostetler, R., *Calculus* (3rd Edition), Lexington, MA: D.C. Heath and Company, 1986.

[48] Guitrau, E.P., *The EDM Handbook*, Cincinnati: Hanser Gardener Publications, 1997.

[49] Varian Turbo-V 301 Navigator Pump. "Varian Turbo-V 301 Navigator Pump Technical Specs". *Agilent Technologies*. http://www.varianinc.com/cgi-bin/nav?products/vacuum/pumps/turbo/t301/specs&cid=LQOLLQOJFL.

[50] Cotronics Corp. "High Temperature Adhesives and Epoxies, Ceramics, Insulation, Epoxies and Epoxy". *Cotronics Corp*. <http://www.cotronics.com>.

[51] Hawari, A.I., Gidley, D.W., Xu, J., Moxom, J., Hathaway, A.G., Brown, B., Vallery, R., The Intense Slow Positron Beam Facility at the NC State University PULSTAR Reactor. *Application of Accelerators in Research and Industry: Twentieth International Conference, AIP Conference Proceedings*. **1099** (2009) 862.

[52] Perkins, A., Carbotte, J.P., Phys. Rev. B **1** (1970) 101.

[53] West, R.N., Adv. Phys. **22** (1973) 263.

[54] R. Suzuki, T. Ohdaira, T. Mikado, Rad. Phys. Chem. **58** (2000) 603.

[55] W. Bauer-Kugelmann, P. Sperr, G. Kogel and W. Triftshauser. Mat. Sci. For. 363-365 (2001) 529.

[56] P. Sperr, W. Egger, G. Kögel, G. Dollinger, C. Hugenschmidt, R. Repper, C. Piochacz, App. Surf. Sci. **255** (2008) 35.

[57] W. Egger, P. Sperr, G. Kögel, G. Dollinger, Phys. Stat. Sol. **4** (2007) 3969.

[58] Humphries, S., *Princles of Charged Particle Acceleration*, New York: John Wiley & Son, 1999.

[59] O'Hanlon, John F., *A User's Guide to Vacuum Technology* (2nd ed.), New York: John Wiley & Sons, 1989.

[60] L. V. Jørgensen, A. van Veen, H. Schut, J. Chevallier. J. Appl. Phys. **81** (1997) 2725.

[61] D. W. Gidley, W. E. Frieze. Phys. Rev. Lett **60** (1988) 1193.

[62] Engelberg, S. *Digital Signal Processing: An Experimental Approach*, London: Springer-Verlag, 2008.

[63] Intersil. *700 MHz Slew-enhanced VFA Datasheet*. May 3, 2007. https://www.intersil.com/data/fn/fn7332.pdf.

[64] Laakso, A. (2005). *Construction of a Pulsing System for Low-energy Positrons*. (Doctoral Dissertation, Helsinki University of Technology).

[65] Knoll, Glen F. *Radiation Detection and Measurement* (3rd ed.), New York: John Wiley & Sons, Inc., 1999.

[66] Carr, J.J., *Secrets of RF Circuit Design*, New York: McGraw-Hill, 2001.

[67] Hagen, J.B., *Radio-Frequency Electronics: Circuits and Applications*, Cambridge, UK:

Cambridge University Press, 1996.

[68] Ortec® Advanced Measurement Technology. *Ortec 583B Data Sheet.* Feb 2007. Updated 2007.

[69] Ortec Advanced Measurement Technology. *Ortec 566 Time-to-Amplitude Converter Data Sheet*. Feb. 2007.

[70] Bodnaruk, E.W. (2008) *Design and Implementation of a Digital Positron Annihilation Lifetime System for Measurements in Graphite.* (Master's Thesis, North Carolina State University).

[71] C. Hugenschmidt, T. Brunner, S. Legl, J. Mayer, C. Piochacz, M. Stadlbauer, K. Schreckenbach. Phys. Stat. Sol. C **4** (2007) 3947.

[72] H. Saito, Y. Nagashima, T. Kurihara, T. Hyodo. Nucl. Instr. Meth. A. **487** (2002) 612.

[73] A.I. Hawari, D.W. Gidley, J. Moxom, A.G. Hathaway, S. Mukherjee. 2011 J. Phys.: Conf. Ser. **262** (2011) 012024.

[74] NEPOMUC: NEutron induced POsitron Source MUniCh. *Institute E21: NEPOMUC.* Updated: April 2010. http://e21.frm2.tum.de/index.php?id=207.

[75] N. Oshima, R. Suzuki, T. Ohdaira, A. Kinomura, T. Narumi, A. Uedono, M. Fujinami. Rad. Phys. and Chem. **78** (2009) 1096.

[76] N. Oshima, R. Suzuki, T. Ohdaira, A. Kinomura, T. Narumi, A. Uedono, M. Fujinami. J. Appl. Phys. **103** (2008) 094916.

[77] *The ARRL Handbook for Radio Communications*. Newington, CT: ARRL, 2002.

[78] J. Olsen, P. Kirkegaard, N. Pedersen, M. Eldrup. *PALSfit: A Computer Program for Analysing Positron Lifetime Spectra*. "Part 1: Mathematical and Physical Foundation". Risø National Laboratory. Roskilde, Denmark. 11-09-2006.

Appendices

Appendix A The Band Reject Filter

The high amplitude rf voltages applied to the bunching electrode were picked up in the anode coaxial cable of the detector. The result was a sinusoidal structure superimposed on the detected pulse. The first attempt to correct this was to house the detector within an aluminum enclosure, which served as a faraday cage and offered rf shielding to the detector. Unfortunately, the sinusoidal structure was not removed from the output, indicating the rf was being picked up by the coaxial cable connecting the detector to its discriminator.

A notch filter is a band reject filter with a high quality factor, *Q*. The quality factor of a filter is the ratio of the central frequency to the bandwidth of the filter. A high *Q* for a notch filter indicates the rejection of a narrow range of frequencies about the central frequency. This means the filter would be capable of attenuating the rf picked up by the detector while allowing the signal pulses to pass through to the discriminator. A series resonant trap can be seen in fig. A.1.

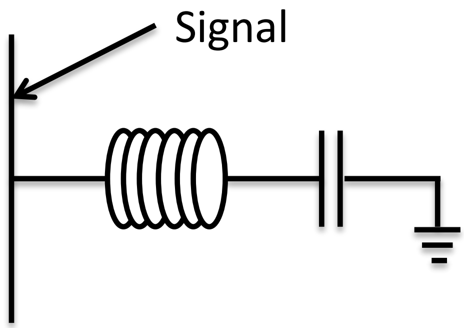

Fig. A.1. Series resonant trap in parallel with the signal path.

This series LC circuit is shunted across the signal path and offers low impedance to incoming signals with frequencies at the resonant frequency of the filter and high impedance at all other frequencies. [66] At resonance, a series LC circuit acts as acts as a short circuit [67], therefore if the incoming signal is at the resonant frequency, it is shunted away from the signal path and straight to ground. For all other frequencies, the pulses bypass the filter and continue along the signal path.

The resonant frequency of a notch filter can be determined using:

$$f = \frac{159}{\sqrt{LC}} \tag{A.1}$$

where f is the frequency in MHz, L is the inductance in μH and C is in pf. The filter was designed to attenuate signals with a frequency of 50MHz using a 2-14 pf capacitor, therefore the desired inductor must be design. Simply rearranging Eq. A.1 allows the calculation of the strength of the inductor required to produce in a resonant LC circuit at a given frequency and capacitance.

$$L = \frac{25280}{f^2 C} \tag{A.2}$$

Assuming a capacitance of 7pf, the required inductor must be 1.44μH.

An air core inductor with an inductance of approximately 1.4μH must be wound to produce a resonant circuit for the notch filter. The inductance of an air wound solenoid can be estimated using Eq.4.27. Assuming a diameter of 0.5” and a length of approximately 1”, a 17 coil solenoid would produce an inductance of 1.47μH. The capacitance can then be varied to 6.88 pf.